CYCLIC VARIATION IN COMBUSTION IN A CONSTANT VOLUME COMBUSTION CHAMBER

by

Ali Ghorbali

A thesis submitted to the School of Graduate Studies in partial fulfillment of the requirement for the degree of

Master of Applied Science

in

Mechanical Engineering

OTTAWA CARLETON INSTITUTE OF MECHANICAL AND AEROSPACE ENGINEERING

OTTAWA, CANADA, 1993

ISBN 0-612-15624-9

UNIVERSITÉ D'OTTAWA
UNIVERSITY OF OTTAWA

Abstract

Cycle to cycle variations in combustion and turbulence characteristics in a swirling flow were measured in a cylindrical vessel. The vessel was charged by rapid tangential injection using a shrouded valve for two valve lifts (7 mm and 12 mm). A premixed lean mixture of propane and air (ϕ = 0.8) was ignited at quarter radius from the center. Pressure rise as a function of time was measured using a pressure transducer. Mean flow, turbulence intensity and Taylor microscale were estimated by statistical analysis of a single hot wire anemometer signal using ensemble averaging and cyclic analysis.

Results obtained indicate that changing the valve lift changes turbulence characteristics at mid-radius. However, turbulence characteristics at quarter radius from center and quarter radius to wall were found to be independent of valve lift.

Mean time, standard deviation of mean time delay and Taylor microscale were estimated using combustion pressure traces.

Results indicate that the mean time and the standard deviation at ignition are weak functions of mean flow and turbulence intensity and strong functions of the Taylor microscale as implied by the Tennekes model. Cyclic variations at ignition were observed to contribute the most to cyclic variations.

Acknowledgements

Special appreciation is expressed to Dr. R. Milane for his support, assistance, guidance and full supervision of this research, as thesis advisor. The author would like also to thank Drs. S. Tavoularis and W. Hallett for their comments and suggestions.

Sincere appreciation is also expressed to the Tunisian Government for providing financial assistance throughout the author's graduate programme.

Contents

List of Tables

List of Figures

Notations

a = Hot wire calibration constant

b = Hot wire calibration constant

C = Thermocouple's time response

M_f = Mole fraction

P_g = Pressure of the flow

P_p = Partial pressure

P_t = Total pressure

R_c = Hot wire cold resistance

R_s = Hot wire operating resistance

R_t = Total resistance

T_g = Flow temperature

T_s = Sensor temperature

U = Arbitrary instantaneous velocity

U_a = Axial velocity

U_b = Binormal velocity

U_e = Effective velocity

U_n = Normal velocity

U_r = Radial velocity

U_t = Tangential velocity

U_w = Velocity normal to the normal and binormal velocities

u = Fluctuation component of velocity

u_a = Axial fluctuation component of velocity

u_b = Binormal fluctuation component of velocity

u_e = Effective fluctuation component of velocity

u_n = Normal fluctuation component of velocity

u_r = Radial fluctuation component of velocity

u_t = Tangential fluctuation component of velocity

u_w = Fluctuation component normal to u_a and u_b

u' = Turbulence intensity

$\overline{u^2}$ = Mean square of fluctuation

$\overline{u_a{}^2}$ = Axial mean square of fluctuation

$\overline{u_b{}^2}$ = Binormal mean square of fluctuation

$\overline{u_e{}^2}$ = Effective mean square of fluctuation

$\overline{u_n{}^2}$ = Normal mean square of fluctuation

$\overline{u_r{}^2}$ = Radial mean square of fluctuation

$\overline{u_t{}^2}$ = Tangential mean square of fluctuation

$\overline{U_b}$ = Binormal mean velocity

$\overline{U_e}$ = Effective mean velocity

$\overline{U_n}$ = Normal mean velocity

$\overline{U_r}$ = Radial mean velocity

$\overline{U_t}$ = Tangential mean velocity

V_0 = Voltage across sensor, prongs, probes, cable and the leg of the Wheatstone bridge

V_s = Voltage across sensor

α = Hot wire calibration constant

α_c = Expansion resistance of the hot wire sensor

β = Hot wire calibration constant

λ = Taylor microscale

σ = Normal stress

Chapter 1

INTRODUCTION

1.1 Preamble

Over the years, engineers have used different ways to improve the performance of their engines. The largest improvement in thermal efficiency has been achieved by raising compression ratios using lean mixtures. However, this results in an unsteadiness of the engine power input, which is unacceptable for a passenger car.

It has been recognized for many years that this power fluctuation is caused by cyclic variations in combustion. The combustion variations are considered a fundamental and widespread combustion problem in spark ignition engines.

These variations manifest themselves as variations in pressure, pressure rate, flame front speed, work of the cycle and the rate of heat transfer.

Early research efforts in the field were devoted to the understanding of the effect of controllable engine operating and design variables on pressure development. Most of these studies showed that these variables have only a marginal effect on the combustion outcome. Recently, the effect of cylinder flows was found to be more significant on combustion, which changed the research trend towards the investigation of the relationship between in-cylinder flows, cyclic combustion, and pressure variations.

1.2 Study Needs

Cyclic variations in combustion limit the optimum use of high compression ratio. The spark must be retarded to avoid detonation, thereby reducing the mean burn rate, which leads to lower engine outputs. Reduction or elimination of combustion variations could lead to:

1. Optimum power output.

2. A smooth running vehicle.

3. An important reduction in exhaust emissions.

4. A reduction of noise (noise due to engine roughness).

Controlling combustion variations such that performance in all cycles is as efficient as in the best cycle can also result in fuel economy.

Combustion variations, which have to be minimized, are expected to be mainly related to the turbulence associated with in-cylinder flows. Therefore, understanding of the turbulence phenomenon within the chamber is essential to explain cycle-to-cycle combustion variations. However, turbulence characteristics are generally not measured directly but rather estimated based on chamber height, engine speed, and assuming an isotropic flow condition. The accuracy in turbulence characteristics can be much improved through direct measurements, and therefore the relationship between turbulence and combustion variation can be better defined.

1.3 Thesis Description

The thesis consists of six chapters. In chapter 1, the subject is introduced, and the study needs are stated. Chapter 2 deals with the major research

contributions of past years. In chapter 3 the experimental apparatus, instrumentation, and experimental procedure are described. Chapter 4 is devoted to the mathematical development for turbulence characteristics, including mean flow, turbulence intensity, and Taylor microscale. Chapter 5 presents and discusses the experimental findings while chapter 6 summarizes conclusions and recommendations for future research.

Chapter 2

LITERATURE REVIEW

2.1 General

Cyclic variations in combustion in spark ignition engines, being an important consideration facing combustion investigators, have been of interest for the past 30 years. Researchers have attempted to investigate the effect of engine operating variables and mixture motion within the combustion chamber on cyclic variations. This problem has been extensively reviewed by Young (1981), therefore there is no necessity to repeat his effort. Instead, a summary of his survey is presented. Also, recent literature (published after 1981) is reviewed.

Young (1981) reported the following:

1. Cyclic variations in combustion are strongly affected by the equivalence ratio, which is an important factor affecting the laminar flame speed and consequently the combustion rate. Minimum cyclic variations occur at a slightly rich equivalence ratio, typically 1.1 to 1.25. At this equivalence ratio, the shortest combustion duration and the highest peak pressure can be reached. The parameters used by the investigators to characterize cyclic variations in combustion are pressure (Soltau 1961), peak pressure (Karim 1967), rate of pressure rise (Patterson 1966) and flame arrival times (Harrow and Orman 1965). By using these different parameters, researchers agreed that minimum cyclic variations occur at a slightly rich equivalence ratio.

2. Dilution of the fresh charge by exhaust gases leads to a decrease in the flame speed. This yields a lower burning rate, which results in an increase in cyclic variations. Karim (1967), Soltau (1961) and Patterson (1966) found that the dilution of the fresh mixture with inert gases has a similar effect on cyclic variations as that of residual gases.

3. Cyclic variations are minimized when fuels having a higher flame speed are used.

4. The type of ignition system, spark duration, spark jitters, spark gap, electrode shape and spark energy do not have any effect on cyclic variations as long as the mixture ignites and the spark gap is greater than the quenching distance. However, the location and number of ignition sources have significant effects on cyclic variations. To minimize these variations , the spark should be located so that the flame speed is maximized, leading to the highest burning rate. Warren and Hinkamp (1956) found that cyclic variations are minimized at MBT (minimum for best torque) spark timing.

5. The combustion chamber shape affects mainly the combustion duration and to a lesser extent cycle to cycle variations. The combustion chamber that leads to higher combustion rates and therefore to the shortest combustion duration produces lower cyclic variations.

6. Compression ratio and engine speed have insignificant effects on cyclic variations. An increase in engine speed usually results in larger cyclic variations and an increase in compression ratio leads to less residual gas and consequently to lower cyclic variations.

7. Cyclic variations in combustion originate during the first stage of combustion.

8. The effect of mixture preparation on cyclic variations is unclear. Different studies have shown higher and lower cyclic pressure variations with homogeneous compared to non-homogeneous mixtures.

Broeze (1950), using different types of valves on a CFR engine, found that the early flame development was more affected than the main combustion period when an organized swirl was present in the combustion chamber. He also found that a shrouded intake valve, providing a swirl, reduces both the delay (from ignition to departure of the cylinder pressure) and the main combustion periods. Vichnievsky and Sale (1958) found that the addition of a shrouded intake valve had an important steadying effect on cylinder pressure development. Witze and Vilchis (1981) unexpectedly found in an engine operating with a lean mixture that cyclic variation increases with an increase in swirl speed. Milane et al (1987) found, for a stoichiometric mixture, that cyclic variation in both ignition and combustion periods decreases as the swirl increases. In another study, Milane (1990) found that the ratio of the mean flow standard deviation to the mean flow and the ratio of turbulence intensity standard deviation to turbulence intensity increase as the swirl decays. The trend followed by these ratios can partially explain the increase of cyclic variation in combustion as swirl decays since changes in mean flow and turbulence

contribute to changes in turbulent kinetic energy and flame front area.

Pischinger and Heywood (1990) showed that the cyclic variations of heat loss to the electrodes can result in significant cycle-to-cycle variations in the initial flame growth. The heat loss varies from cycle to cycle due to substantial variations in the contact area between the flame and the electrodes. They also suggested that the contact area between the flame and the electrodes is controlled by the local flow field which varies from one cycle to another. A large flow velocity convects the flame away from the electrodes, thereby reducing the contact area, which leads to a lower heat loss to the electrodes. Pischinger and Heywood (1990) concluded that the use of thinner electrodes leads to smaller contact area, which reduces the heat loss to the electrodes. They also concluded that a good choice of the electrodes geometries reduces the contact area with the flame.

Anderson (1987) showed, by using a high power C.D.I. system, that the burn time, defined between 10 and 90% of mass burned, is reduced, which results in reduced cyclic variation. Kalghatgi (1987) found that the interaction between the flow field and the flame kernel during the early combustion phase is the major cause of cyclic variation. The motion of the center of the flame kernel was found to be a cause of cyclic variation (Gatowski et al 1984).

Recently, Witze et al (1990) unexpectedly found that the flame kernel convection is not a major source of cyclic variation as first postulated by Gatowski et al (1984). Using several spark plugs, Beshai et al (1988) found the effects of spark pluglocation to be negligible, suggesting that cyclic variation is generated by large scale flow velocity. The distance between spark plugs and its relation to turbulence length scale were not specified. Witze et al (1984) found substantial cyclic variations in the unburned turbulence intensity ahead of the flame front, suggesting that the whole flow pattern is responsible for cyclic variation.

Soltau (1961) performed an experiment in which high speed movies of combustion in an engine were made. He noted that the initial period of combustion (period from ignition to the establishment of a fully developed flame) varies the most from cycle to cycle. However, the fully developed flame travel phase is the most repeatable stage. Arrigoni et al (1973) noted that the initial period of combustion is the most important combustion stage affecting cyclic variations. Kalghatgi(1985) states that "*the early phase of combustion is very crucial since cyclic variations in combustion and hence pressure development originate during this phase*". He also found that cyclic variation in combustion decreases when the laminar flame speed increases. Hill and Kapil (1989) found

that spark gap and combustion chamber geometry do not affect this relation between flame speed and cyclic variations. Hill (19SS) states that" *variations in combustion duration have been reported to be considerably smaller than the variations in the time required for combustion initiation*".

Tennekes (1967) developed a simple model for the structure of turbulence. This model consists of dissipative vortex tubes of thickness η (η is the Kolmogoroff microscale), which are stretched by eddies of size λ (λ is the Taylor microscale). This model is illustrated in Fig. 2.1. In these vortex tubes, the processes of molecular mixing, dissipation of kinetic energy and equalization of temperature and concentration occur at high intensity. In turbulent combustion, Tabaczynski et al (19S1) postulated that, within each λ size region, the flame propagates with a laminar speed s_l, whereas the vortex tubes act as ignition sites, where the flame propagates with faster velocity compared to the laminar speed. Recently, Daneshyar and Hill (1988) postulated, using the vortex bursting concept (Chomiak, 1977), that the burning rate in the η region is proportional to the square root of the density ratio across the flame (unburned to burned gas density ratio) times the turbulent fluctuations. Using a spark shadowgraph, Chomiak (1970) found that the turbulent burning zone consists of distinct vortex tubes of mean diameter approximately equal

to the Kolmogoroff microscale (see Fig. 2.2). Also, by measuring the chemiluminescence in combustion regions, Chomiak (1972) found that the smallest highly luminous objects inside the combustion region have a size of about 1.5 mm, which corresponds approximately to the Kolmogoroff microscale in the region. These observations seems to confirm that viscous dissipation is not uniformly distributed in the flow but is concentrated in small isolated regions. Witze (1981) took flame pictures from four different cycles under identical engine operating conditions (see Fig. 2.3). From this figure, it is clear that in the farthest left picture, the spark ignition occurs in the fast burning zone (η region) so that turbulent spreading began immediately, whereas in the farthest right picture, it seems that the spark ignited at or close to the center of the eddy of size λ, where the laminar flame speed had to precede turbulent spreading. This observed process seems to be in agreement with the hypothesis that the initial cyclic variations are due to the fine turbulence structure.

Keck et al (1987) postulated that the most important parameters affecting the initial flame growth are the size of the first eddy λ burned and the laminar flame speed s_l at ignition. They also suggested that the characteristic eddy size controls the transition from the initial to the fast-burning stage. They found that a substantial displacement of the flame center from the spark plug

occurred during the first stage due to convection by mean flow. Hill (1988) postulated that the characteristic time for cyclic variations at ignition is related to the time to burn an island of size equal to the Taylor microscale. This characteristic time depends on the location of ignition with respect to the fast burning region (vortex tubes). This time varies between 0 (when the spark ignites the vortex tube) and the time $\frac{\lambda}{2s_l}$ (when the spark ignites at the center of the λ size region). Since ignition has the same probability to occur anywhere within an unburned island of size λ, a mean value of $\frac{\lambda}{4s_l}$ was taken by Hill (1988) to be an average delay time.

Hill (1988) measured cyclic variations in combustion in an internal combustion engine with no swirl using combustion pressure traces. He then used the relation for isotropic turbulence between Taylor microscale λ, integral scale L and turbulence intensity u'.

$$\frac{\lambda}{L} = 15^{0.5} Re_l^{-0.5} \tag{2.1}$$

where $Re_l = \frac{u'L}{\nu}$ is the Reynolds number based on the integral scale. To calculate the Taylor microscale λ assuming the integral scale L equal to the instantaneous chamber height, the turbulence intensity was estimated assuming that it is proportional to engine speed.

2.2 Study Objectives

The fuel motion in the cylinder is among the principal factors which affect cycle to cycle variations in combustion. To be more specific, cyclic variations in combustion strongly depend on the parameters characterizing the turbulence in the combustion chamber.

In this study, the work of Hill (19SS) is extended to a swirling flow generated in a constant volume vessel, where turbulence characteristics are directly measured and not estimated. The objectives of this study are:

1. to measure mean flow, turbulence intensity and Taylor microscale using a single hot wire for three locations and two valve lifts;
2. to measure combustion pressure traces for a lean mixture and to deduce cyclic variations in combustion from these traces;
3. to investigate the relationship between the Tennekes model for turbulence structure and cyclic variation in combustion pressure traces.

In order to study the effects of gas motion on cyclic variation in combustion, a constant volume vessel of disc shape with a shrouded intake valve and variable

lift (to generate different turbulent flow fields within the combustion chamber) was designed and constructed to simulate the top dead center of an internal combustion engine chamber.

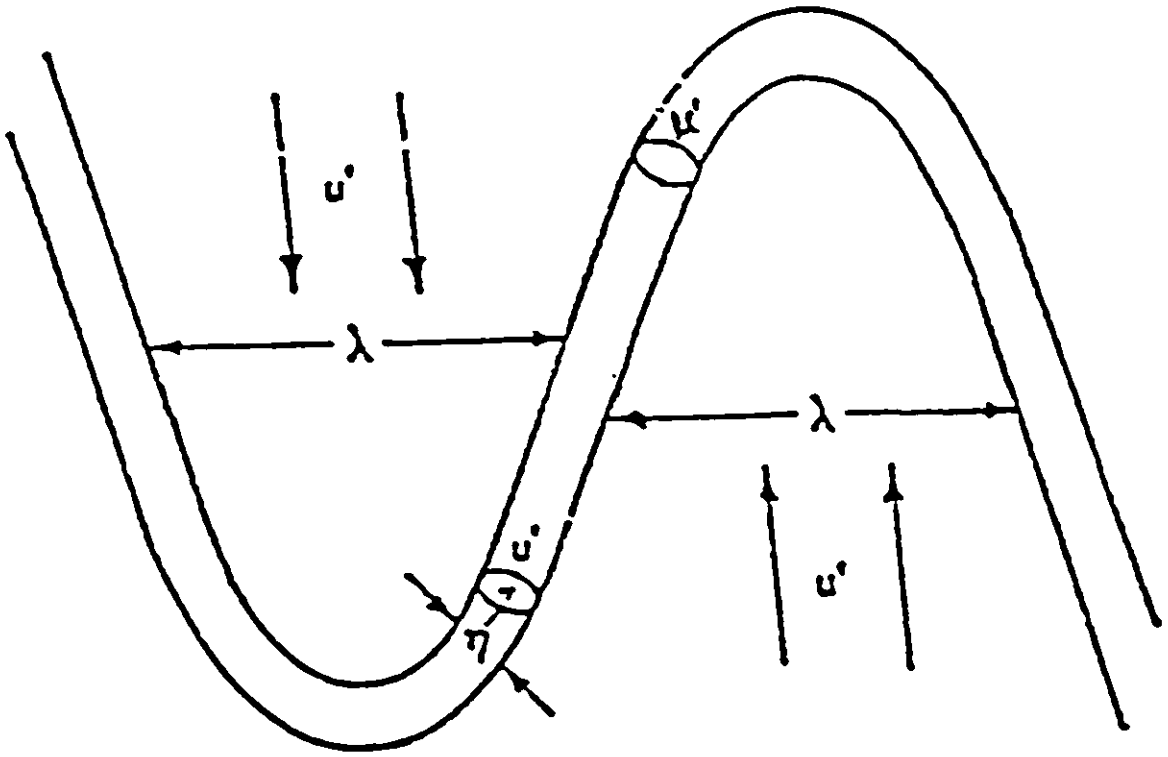

Figure 2.1: Model of Small Scale Structure of Turbulence, (Tennekes 1968).

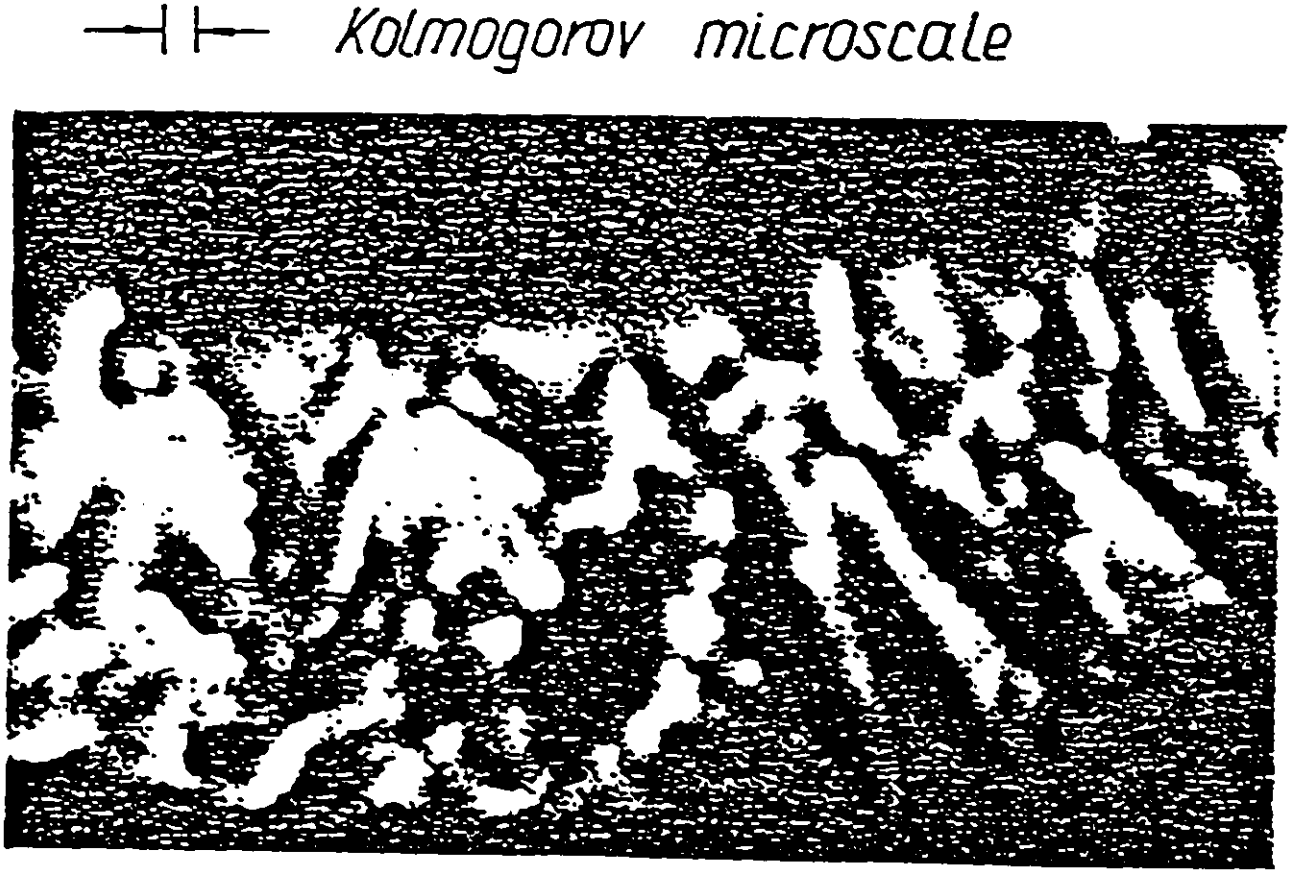

Figure 2.2: Spark Shadowgraph Picture of the Turbulent Burning Zone. (Chomiak 1970).

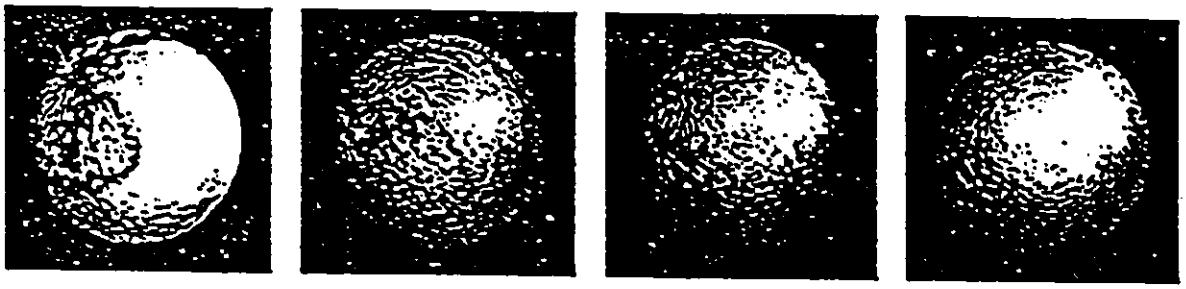

Figure 2.3: Flame Picture from Four Different Cycles under the Same Engine Operating Conditions, (Witze 1981).

Chapter 3

EXPERIMENTAL PROGRAM

3.1 Experimental Apparatus

The experimental program was conducted in the Mechanical Engineering Laboratory at the University of Ottawa. A schematic of the experimental apparatus is shown in Fig. 3.1. A constant volume vessel of disc shape with a shrouded intake valve with variable lift is designed to closely simulate the essential features of the combustion process occurring near top dead center (T.D.C.) in a conventional spark ignition engine. The complete device consists of a cylindrical chamber, an intake system, an air cylinder, a control solenoid valve, an electronic unit, a capacitor discharge (C.D.I) ignition sys-

tem, a high pressure air tank supplying air to activate the air cylinder, a mixture of propane and air, an injection mixture tank and a vacuum pump.

3.1.1 Cylindrical vessel

The cylindrical vessel was designed by Lei (1986). This vessel is made of 316 stainless steel. In order to accommodate the intake system while saving material, the combustion chamber location is off-center. This cylindrical vessel is fitted with one inch thick aluminium discs at each end (Drawing 1, Appendix A). These two aluminium discs are held to the cylindrical vessel by two clamps of one inch thickness each. Each clamp uses six half inch diameter bolts. The intake system, pressure transducer and exhaust valve are fitted flush along the wall of the cylinder.

3.1.2 Intake system

In this study, the intake system, illustrated in drawing 2, Appendix A, was designed so that the valve lift could be varied, thereby inducing different flow fields and different small scale turbulence structures. A half cut shroud is maintained on the valve using two screws (refer to Fig. 3.2). This valve

shroud is used to produce a swirling flow. An "O" ring sits in the groove in the intake to prevent leaking when the valve is closed and to reduce the impact load when the valve hits the intake port during closure. The upper port is a continuation of the intake port. An external threaded ring is used to ?old the upper port and the intake port to the body of the bomb. The injection tank is connected to the combustion chamber through an inlet tube welded to the side of the upper port at a 45^0 angle. The fuel mixture flows into the bomb through the inlet tube, the upper port and the intake port. The intake valve has a rod running through the whole intake system (design of the intake valve is discussed in Appendix B). Two U-cup seals are used between the rod, the upper port and the shroud orientation angle selector to prevent leakage while the system is pressurized or evacuated. The shroud orientation angle selector is fixed to the upper port using a threaded cup. At the end of the rod, a flange is screwed on the rod with a flange lock nut to prevent the flange from rotating. The valve lift is controlled by the position of the flange with respect to the rod. The flange is connected to the air cylinder that controls the opening and the closure of the intake valve.

3.1.3 Spark plug electrodes

In order to ignite the mixture, the spark gap should be greater than the quenching distance. The spark plug cathode is designed to be adjustable in length. Many investigators found that cyclic variations in combustion are not affected by the shape of electrodes. However, a large size electrode might disturb the flow. For this reason the electrodes are pointed near the ignition point. A 2 mm spark gap is used and the spark energy is calculated using the following relationship:

$$Spark - Energy = \frac{CV^2}{2} \tag{3.1}$$

where C is the equivalent capacitance ($C = 23.5\mu f$) and V is the voltage across the anode leg (V=163 volts). The spark energy is found to be 312 mJ.

3.1.4 Electronic control unit

The electronic control unit was designed by a former graduate student, George Faris, from the Department of Electrical Engineering at the University of Ottawa. This unit controls the injection duration of the mixture and the ignition timing. The first signal sent activates the solenoid so that the intake is opened. The ideal opening time of the valve is determined by the duration of

this signal. At the end of this signal, the solenoid is deactivated and the intake closes.. The valve opening time is adjustable from 55 to 200 ms. A second signal triggers the capacitor discharge ignition system. The time delay separating the closure of the valve and the ignition of the mixture is controllable.

3.2 Mixture Preparation

Since the lean mixture is commonly used in the spark ignition engines, an equivalence ratio of 0.8 is selected in the present study. The partial pressure method is used to prepare a mixture of predetermined propane and air ratio. The volume concentration of a component of a gas mixture is proportional to its partial pressure. For an ideal gas, the following equation gives the partial pressure of a component:

$$P_p = M_f P_t \tag{3.2}$$

where P_p is the partial pressure, P_t is the total pressure of the mixture and M_f is the mole fraction of the component.

The chemical reaction describing the combustion of propane and air at an equivalence ratio of 0.8 is

$$0.8C_3H_8 + 5O_2 + 18.8N_2 \longrightarrow 2.4CO_2 + 3.2H_2O + 18.8N_2 + O_2 \tag{3.3}$$

Each mole of propane reacts with 29.75 moles of air. Therefore the mole fraction of propane is 0.0325 and the mole fraction of air is 0.9675. For non-ideal gases such as gases at high pressure and low temperature, equation 3.2 does not hold. In such case, a compressibility factor Z should be included in the equation. The compressibility factor of propane and air is found in a generalized compressibility chart. Since the critical temperature of propane is 370 K at room temperature, the reduced temperature is 0.8. For a total pressure of 1034.2 kPa (150 psi), the partial pressure of propane is 33.6 kPa (4.875 psi) while its critical pressure is 4266 kPa (618.7 psi). Therefore the reduced pressure is very low. At such a low pressure, the compressibility factor is equal to 1, and consequently propane gas is very close to an ideal gas. The critical temperature of air is 143.41 K, and at room temperature the reduced temperature is then 2.25 . The critical pressure of air is 3774.5 kPa (547.4 psi). If the pressure in the mixture tank is 1034.2 kPa (150 psi), the partial pressure of air will be 1000.6 kPa (145.125 psi). Then, the reduced pressure is 0.27. From the compressibility chart, the factor Z of air is found to be 0.98, which is close to unity. Hence, the mixture can be reasonably treated as an ideal gas and equation 3.2 can be applied.

After calculating the proper partial pressure of propane and air, the pres-

sure regulators of the propane and the air tanks can be adjusted accordingly. When filling up the mixture tank, it is suggested that after evacuation propane should be injected first, followed by filling up the tank with air. This procedure is taken so that the high-pressure air in the tank will not rush into the lower pressure propane tank.

Since the pressure in the injection tank is significant for combustion tests, it is recommended to fill up the injection tank slowly to prevent changes in the mixture temperature, and allow it to reach ambient temperature before any re-adjustment of pressure.

3.3 Instrumentation

In order to investigate the turbulence characteristics of air swirl within the combustion chamber, a single hot wire anemometer was used. To compensate for the effect of air pressure and temperature on the output of the hot wire anemometer, a pressure transducer and two different thermocouples (Omega and Namac) were used to measure pressure and temperature respectively. The hot wire probe was inserted parallel to the axis of the combustion chamber so that the axis of the sensor was perpendicular to the combustion chamber axis

and the pressure transducer was fitted flush with the wall of the combustion chamber (Fig. 3.3).

3.3.1 Single Hot Wire

In the last few years the hot wire anemometer has been used as a diagnostic technique for the measurement of fluid motion in internal combustion engines. For simplicity, a single hot wire was used in this study. This technique is limited because it does not resolve flow direction. In order to overcome this limitation, measurements were made in a simplified combustion chamber configuration that produces strong swirl, such that the mean velocity direction is well defined.

The single hot wire anemometer was calibrated at room temperature and atmospheric pressure , then an analytical model (Milane et al, 1988) was used to correct the response signal for its dependence on gas temperature and pressure measured in the combustion chamber. For a cylindrical hot wire sensor operating at a temperature T_s in a flow stream with velocity U, temperature T_g and pressure P_g, the output voltage across the sensor is given by the following formula:

$$V_s^2 = T_g^{.8}(T_s - T_g)(\beta + \alpha \frac{P_g^{\,n}}{T_g^{\,1.76n}} U^n) \qquad (3.4)$$

where α, β and n are calibration constants depending on wire dimensions.

3.3.2 Hot Wire Calibration.

A hot wire anemometer is a thermal device which relates the heat transfer from a heated wire to the flow velocity passing over it. Therefore, it is not an absolute measuring system and it requires calibration.

Consider a standard wire placed in a flow with its axis perpendicular to the direction of the flow (Fig. 3.4). The wire is normal to the flow and its entire length is exposed to the cooling effect. If the probe is yawed about an axis normal to the wire, a progressively shorter wire length will be exposed to the flow, resulting in lower sensitivity. However, if the probe is rotated about the same axis the whole length of the wire will still be exposed to the flow, but the sensitivity increases due to the disturbance of the prongs and the elasticity of the wire.

The anemometer voltage was calibrated against the flow velocity measured by a Pitot tube. The experimental set-up is located in the fluids laboratory (D006 CBY). The flow velocity was determined using a model 34FB2 Meriam manometer. The sensitivity of the manometer is of order of 0.001

inches of H_2O. The calibration experiment was conducted in a low turbulence calibration unit. This set-up consists mainly of a yaw-pitch turnable frame and a low turbulence jet. The velocity of the jet was regulated by a diaphragm actuating as a control valve and maintained constant to an accuracy of $\pm$ 0.1 %. A TSI A 260 A-t1-5 hot wire having a 5 μm diameter and about 1.3 mm length was used in all experiments. In order to obtain accurate information about the directional sensitivity of a normal hot wire probe a velocity and yaw calibration was carried out. Fig. 3.5 illustrates the general orientation of a single cylindrical sensor mounted perpendicular to the probe axis with respect to an arbitrary velocity U. This velocity U can be decomposed into a normal component U_n, a binormal component U_b and a component U_w normal to U_b and U_n. It is obvious that U_n and U_b should have a major contribution in the cooling of the wire, while the contribution of U_w should be of secondary importance.

A common expression used for the effective cooling velocity U_e is:

$$U_e^2 = U_n^2 + a^2 U_b^2 + b^2 U_w^2 \tag{3.5}$$

where a^2 and b^2 are calibration constants which account for the hot wire length to diameter ratio, the mounting type, the size of the prongs and the shape and the proximity of the probe shape. To determine the constant a^2, the hot

wire is placed binormal to the flow (refer to Fig. 3.4). The actual velocity is measured using a Pitot tube and a Meriam manometer, whereas the effective velocity U_{e1} is measured using the hot wire anemometer. The constant a^2 is equal to the ratio of the square of the mean effective velocity and the square of the mean actual velocity. The constant b^2 is determined in the same manner as a^2 by placing the wire parallel to the flow. In the present study, a^2 and b^2 were found to be 1.2 and 0.016 respectively (refer to Table 3.1).

The anemometer signals were sampled at a rate of 50 kHz using a digital oscilloscope (Nicolet model 3091), and the data were time averaged. Initially the resistance of the unheated wire R_c was determined and the operating resistance R_s of the wire was selected in such a way that the wire operating temperature T_s was equal to 250 deg C. The operating resistance is given by the following formula:

$$R_s = R_c(1 + \alpha_c(T_s - T_c)) \tag{3.6}$$

where α_c is the resistance coefficient of the wire and T_c is the ambient temperature. The voltage recorded V_o is equal to the sum of the voltages across the sensor, the prongs, the probe, the cable and the leg of the Wheatstone bridge.

The voltage across the sensor is expressed as follow:

$$V_s = \frac{V_o R_s}{R_t} \tag{3.7}$$

where $R_t = 40 + R_{probe} + R_{prongs} + R_s$. The velocity measured by the Meriam manometer is obtained using the calibrated equation:

$$U = 20.4(\delta H)^{.5} \tag{3.8}$$

where δH is the dynamic pressure head in inches. The above equation is valid at a temperature of 21.5 deg C and a pressure of 101 kPa. The air flow velocity U was varied, δH and V_o were recorded, then the velocity U and the voltage across the sensor were calculated.

The constants α, β and n are determined in such a way that the maximum error in the calculated value of V_s^2 is minimum, using a least-square-fit for a polynomial of order 1.

These values were α =2.245 E-06, β =9.1194 E-06 and n=.44. In Fig. 3.6 the experimental curve for V_s^2 versus $U^{.44}$ is compared to the calculated one using equation 3.4.

3.3.3 Temperature measurement

Three different techniques were considered to measure the flow temperature. These three techniques are:

1. Cold wire (single hot wire operating at constant current).
2. Parallel hot wire (two parallel wires at two different constant temperatures).
3. Thermocouples, type E (From Namac and Omega).

According to the first law of thermodynamics, the absolute temperature in the bomb, immediately after injection, would reach a value approximately equal to γ (the specific heat ratio of the flow mixture) times the initial temperature. After this, the absolute temperature decreases with time because of heat exchange at the wall.

Cold wire

Two types of single sensor cold wire operating at constant current were used. The first was a TSI tungsten wire plated with platinum, $5\mu m$ in diameter and about 1 mm long. The second was a Disa platinum wire Model No. 55P31, $1\mu m$ in diameter and 0.4 mm long. These two cold wires were operated at two different currents of 0.5 and $1.0m.A$. The resulting temperature traces, however, showed a lot of scatter, which prevented reasonably accurate measurements. This technique was therefore rejected.

Parallel sensors

A dual sensor probe model 1244 (5 μm tungsten wire plated with platinum) with both sensors mounted parallel and closely spaced (1mm) were used. The two wires are located sufficiently close to each other to detect the same fluid properties and they are operated at two different temperatures T_s. Applying equation 3.4 for both sensors, one can obtain the instantaneous fluid temperature.

$$T_g = T_{s1} - \frac{{V_{s1}}^2}{{V_{s1}}^2 - {V_{s2}}^2}(T_{s1} - T_{s2}) \tag{3.9}$$

Using this method, as was the case for cold wire, too much scatter was found in the temperature data. Therefore, this instrument was also rejected.

Thermocouples

Thermocouples from different manufacturers (Omega and Namac) were used to measure temperature. The two thermocouples are of type E (chromel and constantan). The Omega and Namac thermocouples have 0.0254 mm (0.001 in) and 0.0508 mm (0.002 in) junction thickness respectively. These two thermocouples indicated the same temperature trace; however the Omega thermocouple was adopted for later use. No instrument responds instantly to a change in its environment, therefore these thermocouples cannot indicate the true temperature. It is common practice to characterize the response of a temperature sensor (thermocouple) by a first order differential equation defined as:

$$T(t) + C\frac{\partial T(t)}{\partial t} = T_e(t) \tag{3.10}$$

where T(t), $T_e(t)$ are the indicated and the environmental temperature respectively and C is the thermal time constant. For both thermocouples the response time C is given by the manufacturer to be between 2 and 5 ms. The indicated temperature has a maximum slope of .5 K/ ms and an average value

of 325 K (see Fig. 3.7). Therefore the maximum of the term $C\frac{\partial T(t)}{\partial t}$ is 2.5 deg K which can be assumed negligible compared to T(t).

From equation 3.10, we can conclude that the indicated temperature is approximately equal to the environmental temperature within 0.8% error.

3.3.4 Pressure Measurement

In combustion, electrical pressure transducers are the most commonly used. The accurate measurement of pressure is extremely important in the present study. However, pressure measurements obtained during the occurrence of exothermic processes may suffer from error due to thermal loading of unprotected transducers. To minimize these errors, investigators have suggested the application of an insulating rubber coating (e.g RTV) over the transducer diaphragm. This insulating rubber has an insignificant effect on time response. In the present experiment, the pressure was measured using a Kistler Model 609-B quartz pressure transducer. The transducer diaphragm was coated with a high temperature silicone rubber compound (GERTV12) after having been primed and solvent cleaned. This procedure was undertaken to reduce errors due to thermal loading. The transducer is coupled to a Kistler charge amplifier

Model No. 5004 which is recorded on a digital oscilloscope Model 3091. Using the most common serial interface protocol RS-232, the data were transferred to a personal computer, then stored on a floppy disk. A sample line printer pressure history is shown in Fig. 3.8.

Because of the inertia of the valve, a delay period between the triggering of the signal and the actual valve opening occurs. This delay is determined directly from the pressure trace since the pressure starts building up when the valve opens. The event starts at a time $t = 0$, the intake valve opens at $t = 41\ ms$ and the pressure starts building up with a constant rate till the valve starts closing, then the pressure rate decreases suddenly. When the valve closes ($t = 116\ ms$) the pressure decreases because of the heat transfer to the chamber walls and the environment. The actual valve opening time is determined experimentally from the pressure trace. The transducer sensitivity is adjusted according to calibration data supplied by the manufacturer. Since the expected peak combustion pressure is around 25 atm (362 psi), the calibration factor 1.09 pc/bar was selected.

3.4 Experimental Procedure

To study the effect of flow field on combustion cyclic variation, it is essential to identify flow parameters and characteristics for given conditions. Therefore, cold flow experiments were undertaken before dealing with combustion.

3.4.1 Cold flow

Measurements of velocity, pressure, and temperature were taken for two valve lifts (7 and 12 mm), at mid-plane at three different locations (one quarter radius from the wall, mid-radius, and one quarterradius from the center), shown in Fig. 3.2. This resulted in a total of six experimental conditions.

For a given valve lift and location of measurement, 40 cycles of pressure and velocity were taken simultaneously. Later, the hot wire probe was replaced by a thermocouple and 40 cycles of temperature were traced. Pressure, velocity, and temperature measurements could not be taken simultaneously because the oscilloscope used had only two channels, which allows a maximum of two signals to be taken at a time.

For each event, the combustion chamber was first evacuated, then air

was injected through the intake valve to the cylinder. Air was used in the cold flow experiments instead of a mixture of air and fuel for safety as well as economical reasons. Signals from hot wire anemometer, pressure transducer, and thermocouple were digitized and stored in a Nicolet model 3019 digital oscilloscope. The digitizing rate was 50 kHz, which enabled measurements, taken 15 ms after valve closure, to be obtained over a time period of 80 ms. Digitized data were transferred and stored in a floppy disk of a micro computer for further analysis.

3.4.2 Combustion

In this part of the experimental program, hot wires and thermocouples were removed and only pressure transducers were kept in place to take pressure measurements. Ignition was produced at two different times from valve closure (24 and 78 ms) at quarter radius from the centre for two different valve lifts (7 and 12 mm), thereby reproducing the same flow conditions of the cold flow experiments. Pressure measurements, which started at ignition time, were taken for 40 cycles over a period of 20 ms. For a particular condition (valve lift = 7 mm, ignition time = 74 ms), 70 cycles instead of 40 cycles of pressure trace were taken to determine the effect of the chosen number

of cycles (40 cycles) on the results. Pressure traces over 40 and 70 cycles were comparable, implying that 40 cycles are sufficient for the results to be statistically meaningful.

Table 3.1: Calibration constants a^2 and b^2

Mean actual velocity $\overline{U}(m/s)$	Mean effective velocity $\overline{U_{e1}}(m/s)$	Mean effective velocity $\overline{U_{e2}}(m/s)$	$a^2 = \frac{\overline{U_{e1}}^2}{\overline{U}^2}$	$b^2 = \frac{\overline{U_{e2}}^2}{\overline{U}^2}$
9.02	9.84	1.16	1.19	0.0165
14.49	16.00	1.86	1.22	0.0164
21.42	23.46	2.72	1.20	0.0161
27.94	30.35	3.56	1.18	0.0162
36.55	39.53	4.69	1.17	0.0165
42.79	47.26	5.36	1.22	0.0157
47.18	51.90	5.87	1.21	0.0155

Notes

- The mean actual velocity $\overline{U}$ is measured by Pitot-tube during hot wire calibration.
- The mean effective velocity $\overline{U_{e1}}$ is a time average effective velocity measured by the hot wire anemometer when the sensor is binormal to the flow.
- The mean effective velocity $\overline{U_{e2}}$ is a time average effective velocity measured by the hot wire anemometer when the sensor is tangential to the flow.

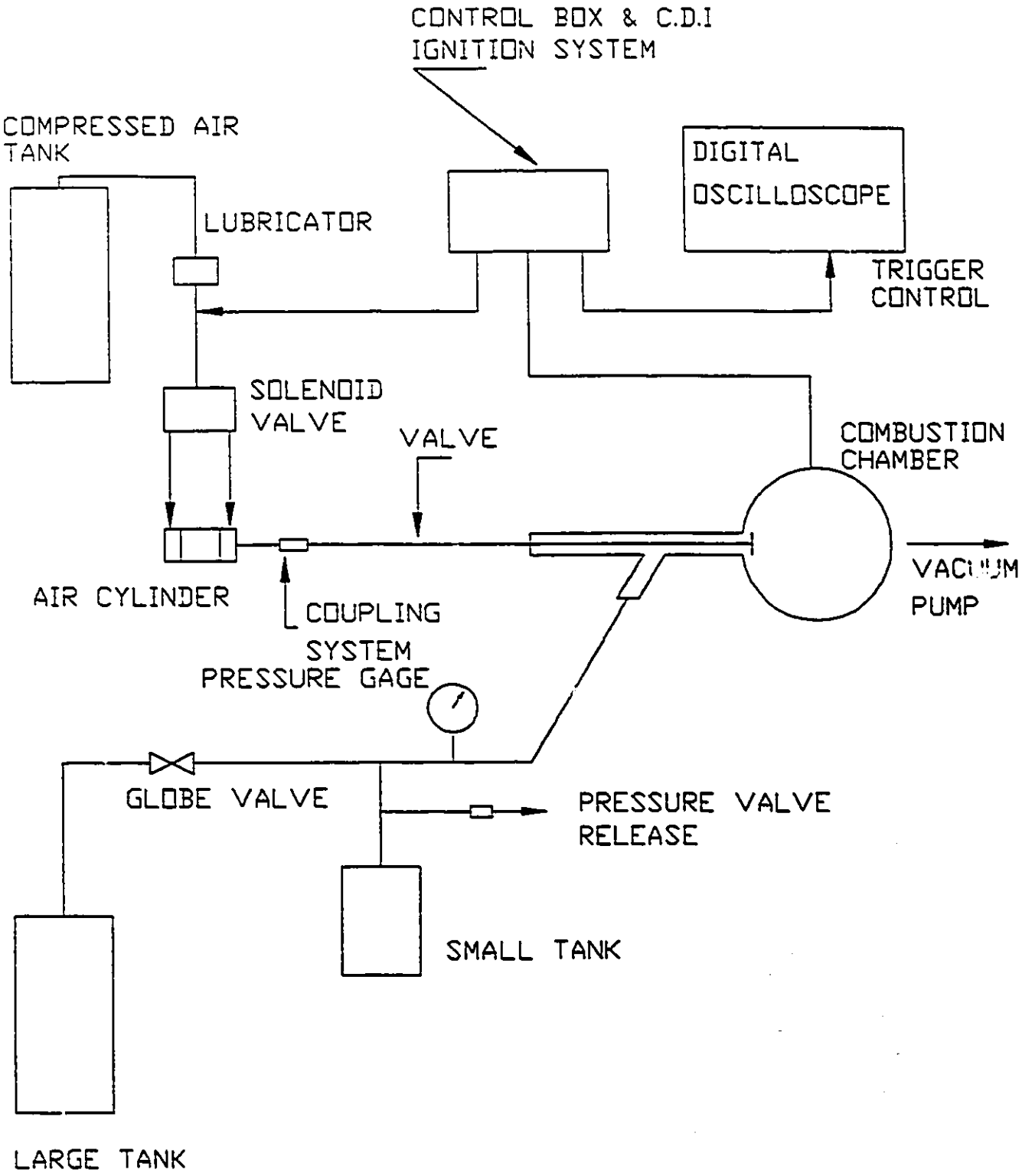

Figure 3.1: Schematic of the Experimental Apparatus.

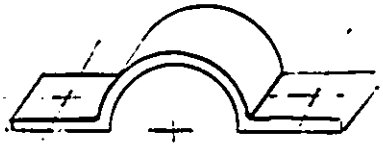

Mounting Ring

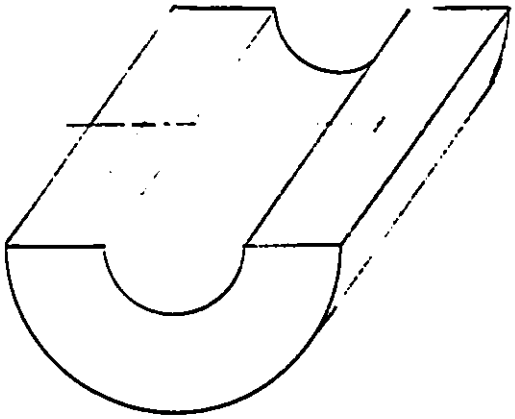

Shroud Valve

Figure 3.2: Valve Shroud.

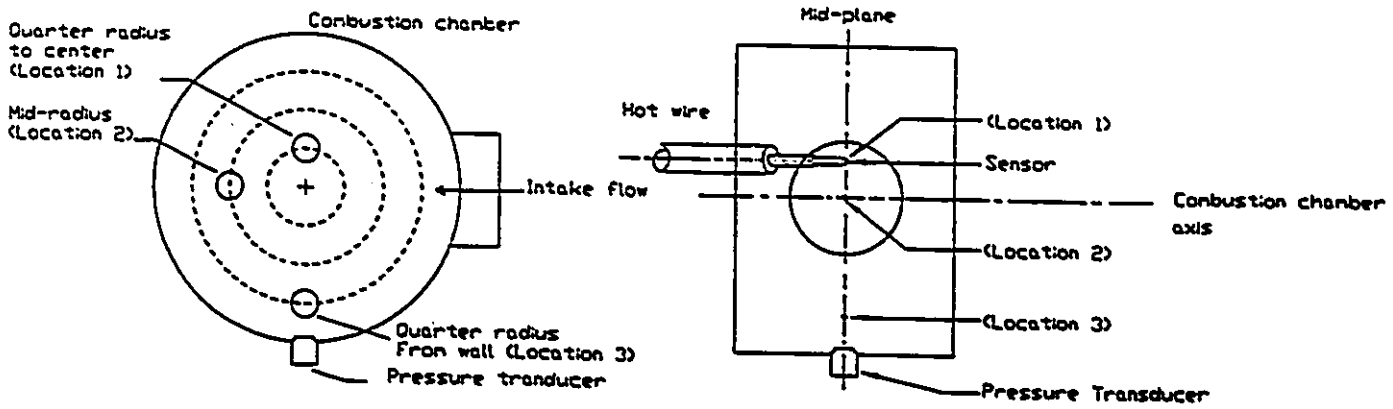

Figure 3.3: Location of the Hot Wire and Pressure Transducer.

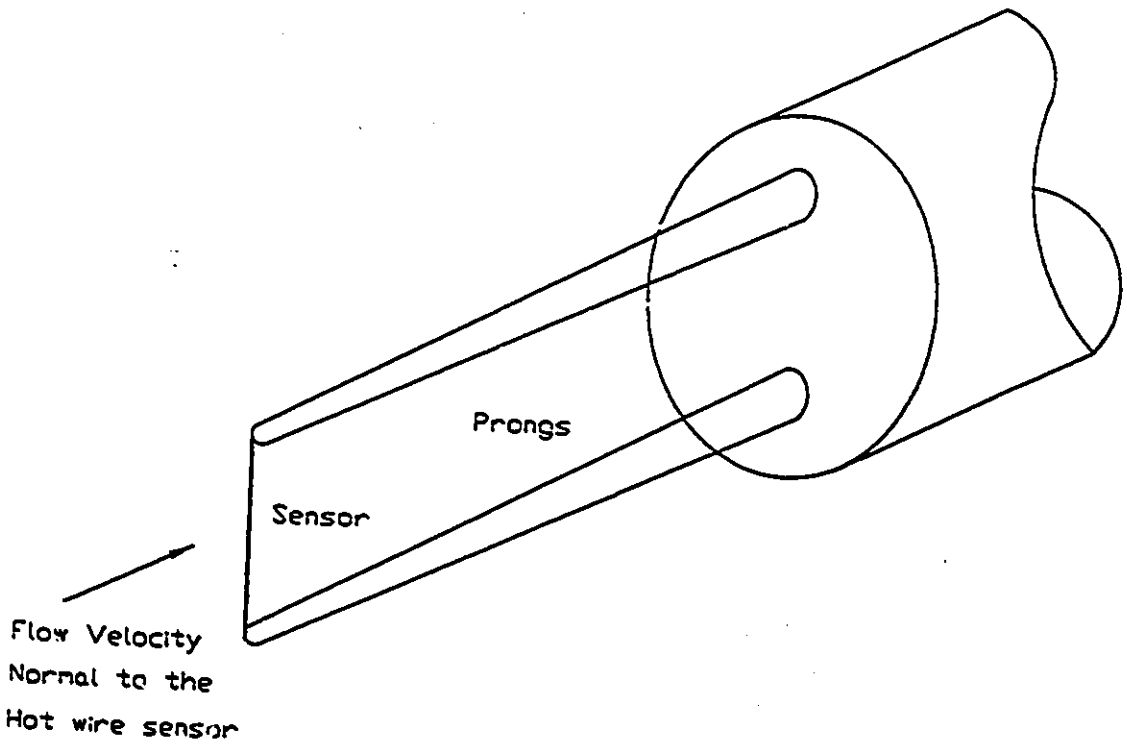

Figure 3.4: Single Hot Wire.

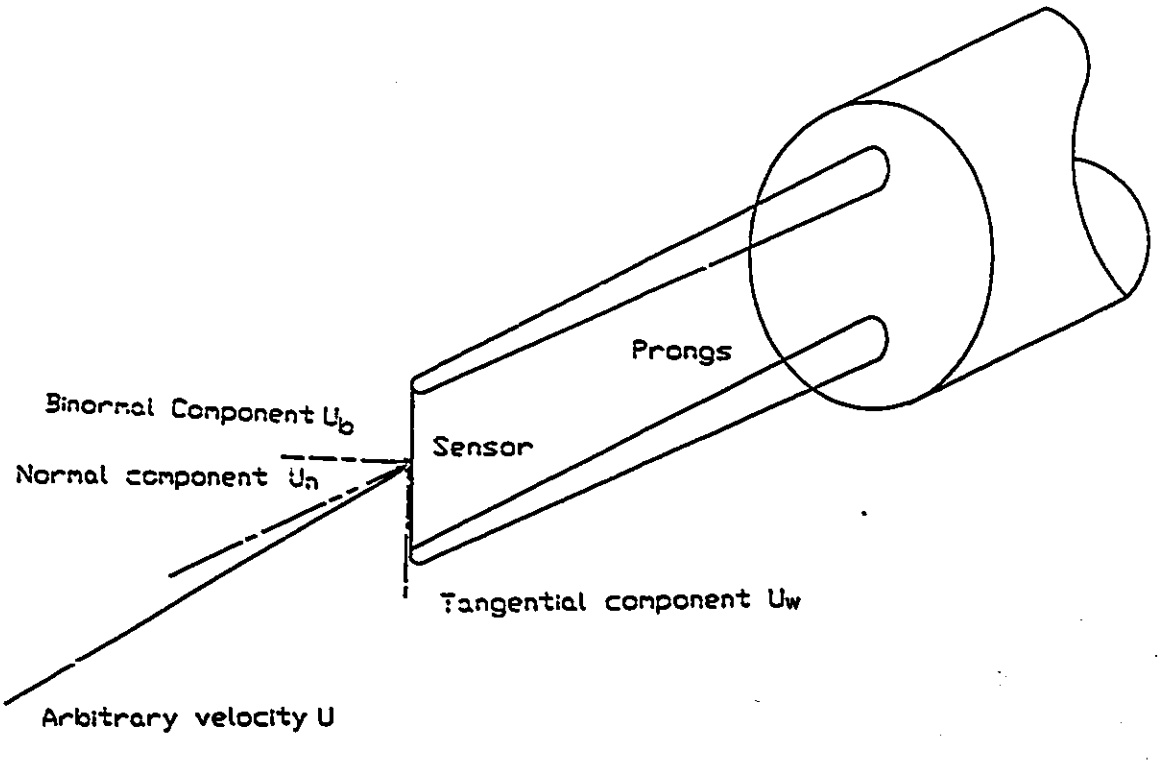

Figure 3.5: General Orientation of a Single Cylindrical Sensor.

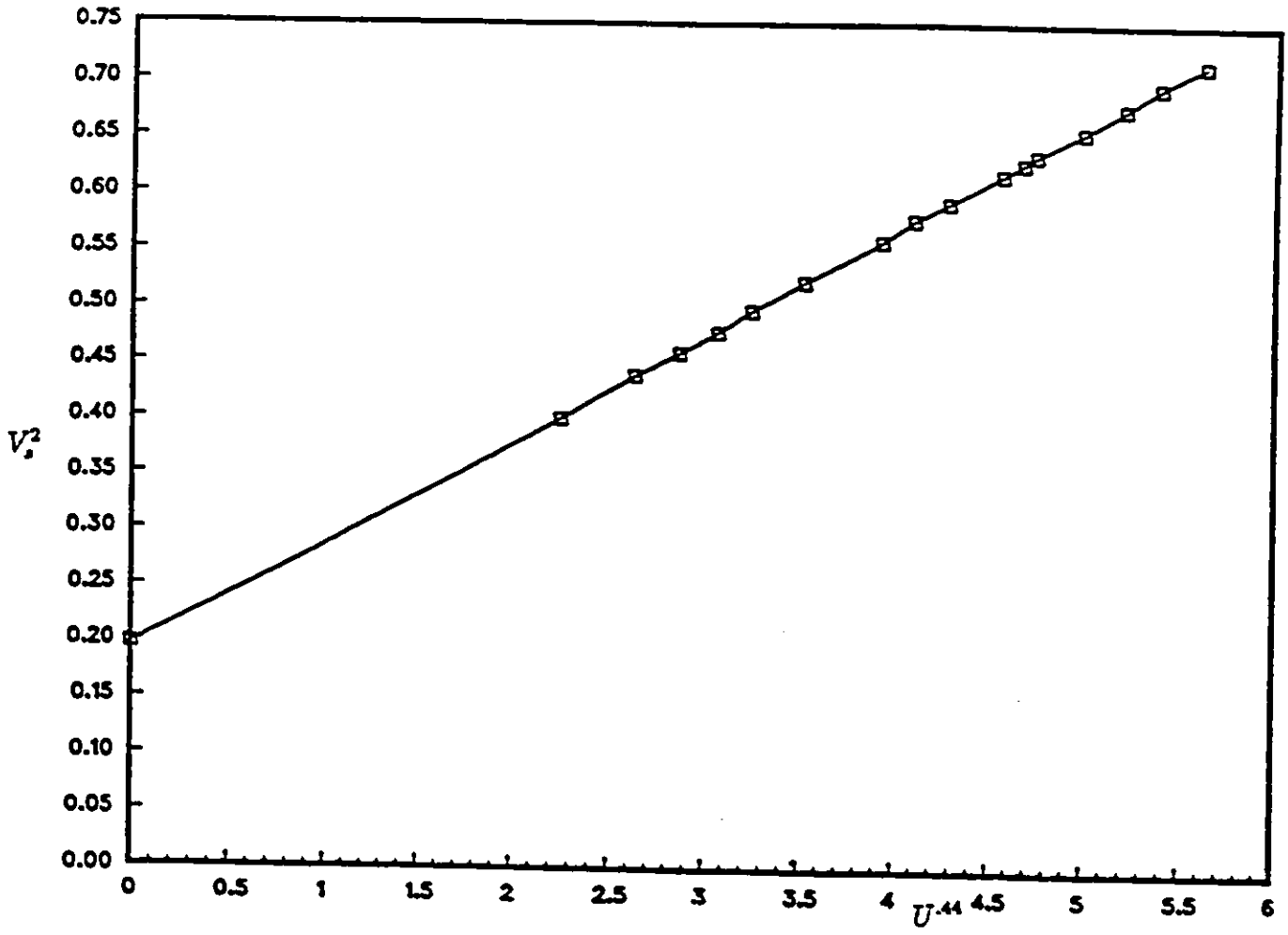

Figure 3.6: Calibration Curve for the Hot wire Sensor.

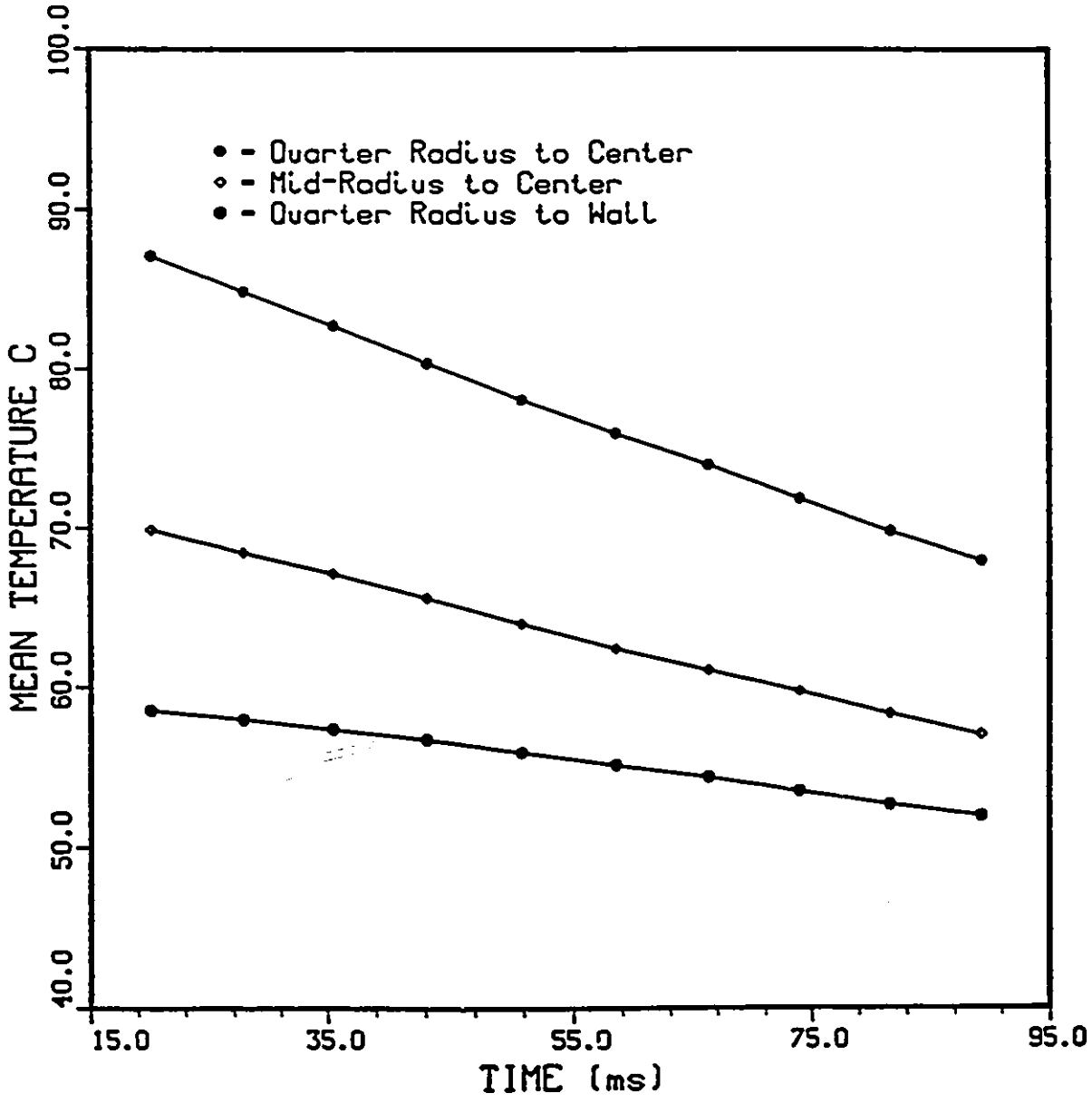

Figure 3.7: Mean Temperature Variation with Time at three Different Locations within the Combustion Chamber.

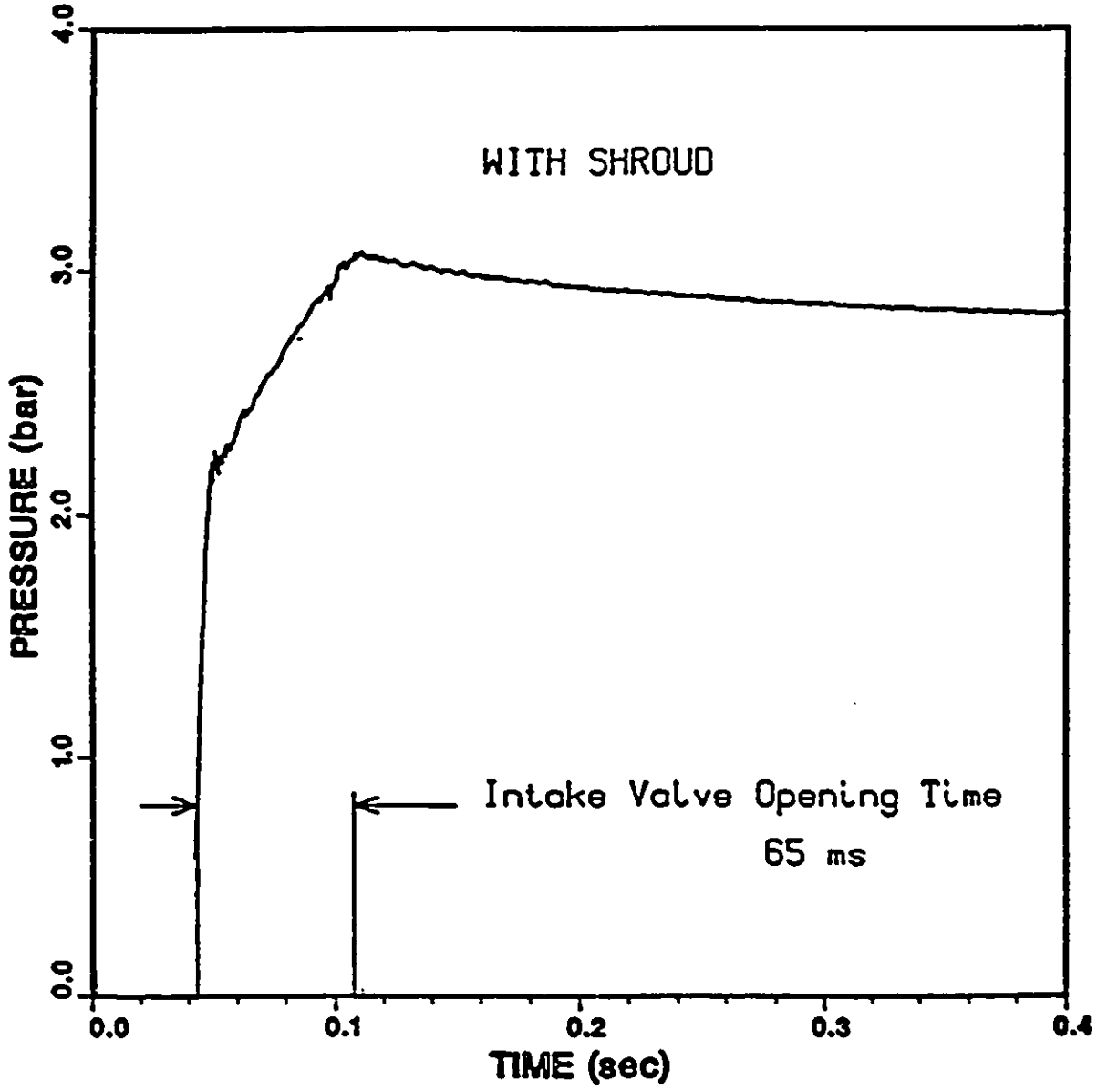

Figure 3.8: Sample Pressure History.

Chapter 4

MATHEMATICAL DEVELOPMENT

In this chapter, relationships for mean flow, turbulence intensity, and Taylor microscale are presented.

4.1 Instantaneous Mean Flow and Turbulence Intensity

The single hot wire probe, which can rotate about its axis, is inserted with the wire parallel to the axis of the combustion chamber (see Fig. 3.2). The sensor is exposed to an unknown flow velocity U. This velocity can be decomposed

into an axial component U_a, a tangential component U_t and a radial component U_r (refer to Fig. 4.1). The velocity U is related to these three components as:

$$U^2 = U_a^2 + U_t^2 + U_r^2$$

On the other hand, the effective velocity measured by the hot wire sensor can be written as:

$$U_e^2 = U_a^2 + a^2(cos^2(\theta)U_t^2 + sin^2(\theta)U_r^2) + b^2(cos^2(\theta)U_r^2 + sin^2(\theta)U_t^2) \quad (4.1)$$

where θ is the angle between the sensor and the radial axes. The instantaneous velocities U_a, U_t and U_r can be decomposed into mean ($\overline{U_a}$, $\overline{U_t}$ and $\overline{U_r}$) and fluctuating components (u_a, u_t and u_r). Substituting these expressions into equation 4.1 for $\theta = 0$, expanding the squares and averaging, one gets:

$$\overline{U_e^2}(\theta = 0) = \overline{U_a}^2 + a^2\overline{U_t}^2 + b^2\overline{U_r}^2 + \overline{u_a^2} + a^2\overline{u_t^2} + b^2\overline{u_r^2} \quad (4.2)$$

The above equation is complicated and it is impossible to solve for the actual velocity U from the effective cooling velocity. Therefore, the hot wire probe was rotated and measurements at different orientations ($\theta = 0$, $\theta = 45$ and $\theta = 90$) were performed. Results (see next chapter) show that the flow is mostly tangential and the mean flows in the radial and axial directions are assumed to be negligible. Then equation 4.2 is reduced to:

$$\overline{U_e^2}(\theta = 0) = a^2(\overline{U_t}^2 + \overline{u_t^2}) + \overline{u_a^2} + b^2\overline{u_r^2}$$

b^2 was found to be negligible compared to 1 and a^2, therefore it is possible to neglect the third term in the right hand side of the above equation

$$\overline{U_e}^2(\theta = 0) = a^2(\overline{U_t}^2 + \overline{u_t^2}) + \overline{u_a^2} \qquad (4.3)$$

On the other hand the square of the effective velocity can be deduced from equation 4.1

$$U_e^2(\theta = 0) = a^2 U_t^2 + u_a^2 \qquad (4.4)$$

which can be rewritten as:

$$U_e^2(\theta = 0) = a^2(\overline{U_t} + u_t)^2 + u_a^2$$

rearranging,

$$U_e^2(\theta = 0) = a^2\overline{U_t}^2(1 + \frac{u_t}{\overline{U_t}})^2 + u_a^2$$

expanding, one gets

$$U_e^2(\theta = 0) = a^2\overline{U_t}^2(1 + \frac{u_t^2}{\overline{U_t}^2} + 2\frac{u_t}{\overline{U_t}} + \frac{u_a^2}{a^2\overline{U_t}^2})$$

Solving for U_e $(\theta = 0)$

$$U_e(\theta = 0) = a\overline{U_t}(1 + \frac{u_t^2}{\overline{U_t}^2} + 2\frac{u_t}{\overline{U_t}} + \frac{u_a^2}{a^2\overline{U_t}^2})^{0.5}$$

Averaging, one gets:

$$\overline{U_e}(\theta = 0) = a\overline{U_t}(1 + \frac{{u_t}^2}{\overline{U_t}^2} + 2\frac{u_t}{\overline{U_t}} + \frac{{u_a}^2}{a^2\overline{U_t}^2})^{0.5} \tag{4.5}$$

Let

$$x = \frac{{u_t}^2}{\overline{U_t}^2} + 2\frac{u_t}{\overline{U_t}} + \frac{{u_a}^2}{a^2\overline{U_t}^2} \tag{4.6}$$

Consider a function $f(x) = (1+x)^{\frac{1}{2}}$. This function can be written in a form of power series (Maclaurin series) as follows:

$$f(x) = \sum_{m=0}^{\infty} \frac{f^m(0)}{m!} x^m$$

where f^m is the mth derivative of f. Expanding the above equation, one gets

$$f(x) = 1 + \frac{1}{2}x - \frac{1}{8}x^2 + \theta(x^3) + ... \tag{4.7}$$

Substituting equation 4.6 and 4.7 into equation 4.5, dropping the terms with high power (third and higher power terms) and squaring, we get:

$$\overline{U_e}^2(\theta = 0) = a^2\overline{U_t}^2 + \overline{{u_a}^2} \tag{4.8}$$

This results in 2 equations (4.3 and 4.8) and 3 unknowns ($\overline{U_t}^2$, $\overline{{u_t}^2}$, and $\overline{{u_a}^2}$). Another equation is required to solve for the three unknowns. Writing equation 4.1 for $\theta = 90\,\text{deg}$, decomposing the instantaneous velocities into

means and fluctuating components, expanding the squares, then averaging and neglecting the radial and axial mean flows and also the third term in the right hand side of the original equation (4.1) one gets:

$$\overline{U_e}^2(\theta = 90) = a^2\overline{u_r}^2 + \overline{u_a}^2 \tag{4.9}$$

On the other hand, the square of the effective velocity can be deduced directly from equation 4.1.

$$U_e^2(\theta = 90) = a^2U_r^2 + u_a^2 \tag{4.10}$$

Equation 4.10 was rearranged in the same way as equation 4.4 ($\theta = 0$) and the mean radial flow was neglected to yield:

$$\overline{U_e}^2(\theta = 90) = \overline{u_a^2} \tag{4.11}$$

Finally, four equations (4.3, 4.8, 4.9 and 4.11) were derived to solve for the unknowns ($\overline{U_t}^2$, $\overline{u_t^2}$, $\overline{u_a^2}$, and $\overline{u_r^2}$). Combining equations 4.11 and 4.9, we obtain:

$$\overline{u_r}^2 = \frac{\overline{U_e}^2(\theta = 90) - \overline{U_e}^2(\theta = 90)}{a^2} \tag{4.12}$$

Similarly, combining equations 4.3 and 4.8 results in:

$$\overline{u_t}^2 = \frac{\overline{U_e}^2(\theta = 0) - \overline{U_e}^2(\theta = 0)}{a^2} \tag{4.13}$$

The mean square fluctuations ($\overline{u_t^2}$, $\overline{u_a^2}$, and $\overline{u_r^2}$) were calculated using equations 4.11, 4.12, and 4.13 respectively (based on an ensemble averaging method described later). It was found that these terms are approximately equal (Tables

4.1 to 4.3), implying isotropic flow condition ($\overline{u_t^2} = \overline{u_a^2} = \overline{u_r^2} = \overline{u^2}$). Measurements were then taken at only one sensor direction ($\theta = 0$). Subsequently, $U_e(\theta = 0)$ is referred to as simply U_e. The mean tangential velocity is obtained from equation 4.3:

$$\overline{U_t} = \left(\frac{\overline{U_e^2} - (1 + a^2)\overline{u^2}}{a^2}\right)^{0.5} \tag{4.14}$$

Substituting equation 4.13 into equation 4.14 one gets:

$$\overline{U_t} = \frac{1}{a^2}((1 + a^2)\overline{U_e}^2 - \overline{U_e^2})^{\frac{1}{2}} \tag{4.15}$$

In conclusion, for the present swirling flow, the flow field can be resolved by placing the hot wire sensor in such a way that it is fully exposed to the tangential flow and using equation 4.13 and 4.15 to calculate the tangential mean flow and the turbulence intensity.

4.2 Average Turbulence Characteristics

Measurements were taken 15 ms after the closing of the intake valve over a period of 80 ms. In this study, turbulence characteristics are calculated using two different methods, ensemble average analysis and cycle-by-cycle-analysis (Liou and Santavicca, 1988). The ensemble average analysis can not give an accurate indication of the mean flow at a point in a given cycle if there

are significant variations from cycle to cycle. The root-mean-square of the turbulent velocity can be overestimated. To overcome this problem a cycle by cycle analysis needs to be carried out. The instantaneous velocity at a given point in a cycle is expressed as a "mean" (which may vary with time) plus a turbulent velocity deviation from this mean. In other words, the flow consists of a basic flow pattern on which the turbulent fluctuations are superimposed. At this point, it is necessary to determine what part of the instantaneous velocity constitutes the mean and what part constitutes the turbulence.

The fast Fourier transform (FFT) of the instantaneous velocity of each cycle is calculated, then a cut-off frequency W_c is defined . The FFT Program, supplied by R. Milane (1986), was modified to meet the needs of the present study. The component of the FFT below W_c represents the mean flow and the components above W_c represent the turbulence. The cut-off frequency W_c was calculated by examining the non-zero components of the FFT of the ensemble averaging. The cut-off frequency was selected as the frequency where the amplitude from the FFT is equal to 2 % of the amplitude at zero frequency. The sensitivity of the results to the selection of W_c will be examined in the results section.

Noise in the signals was treated by eliminating the components of the

FFT above a cut-off noise frequency. The instantaneous velocity of each cycle is written in the form of the Fourier series as follow:

$$U(t) = a_0 + \sum_{n=1}^{W-1} a_n cos(nwt) + b_n sin(nwt) \tag{4.16}$$

where W is the number of points in the time window.

The mean flow velocity $\overline{U(t)}$ is determined from the above equation by equating the coefficients a_n and b_n to zero for n greater than the value corresponding to the cut-off frequency W_c. The fluctuation $u(t)$ is determined by equating the coefficients a_0, $a_n$and b_n to zero for n less than the value corresponding to the cut-off frequency W_c and n greater than the value corresponding to the cut-off noise frequency. The cut-off noise frequency was determined following an analysis similar to that of Sreenivassen et al (1983). The Taylor microscale was calculated assuming various values of cut-off frequency, starting from the highest frequency in the signal (25 kHz). The Taylor microscale was calculated using 40 cycles, and over a period of 10.24 ms, corresponding to 512 points. Fig. 4.2 shows the Taylor microscale plotted versus the cut-off noise frequency. Initially, the Taylor microscale decreases as the cut-off noise frequency increases. A plateau is reached above 10 kHz. The Taylor microscale is insensitive to a value of the cut-off noise frequency above 10 kHz. In this study, the cut-off frequency was assumed to be 10 kHz.

4.2.1 A Mean velocity

The radial and axial mean velocities were assumed to be negligible ($\overline{U_a} = \overline{U_r} = 0$).

Ensemble Averaging Method

The ensemble average mean tangential velocity $\overline{U_t(t)}$ at a given time in the cycle is defined as (refer to equation 4.15):

$$\overline{U_t(t)} = \frac{1}{a^2}\left[(1+a^2)\left(\frac{\sum_{i=1}^{N} U_{e,i}(t)}{N}\right)^2 - \frac{\sum_{i=1}^{N} U_{e,i}^2(t)}{N}\right]^{\frac{1}{2}} \qquad (4.17)$$

where $U_{e,i}(t)$ is the instantaneous effective velocity at time t of the i^{th} cycle and N is the number of cycles sampled.

A time-averaged mean velocity was calculated over a period of 10.22 ms (corresponding to 512 points). This mean flow is calculated as follows:

$$\overline{U_t} = \frac{1}{W}\sum_{j=1}^{W}\overline{U_t(t)} \qquad (4.18)$$

where W is the number of the points in the time window.

Cyclic Analysis Method

The cyclic analysis mean tangential velocity $\overline{U_{t,i}(t)}$ at time t of the i^{th} cycle is given by the following formula (refer to equation 4.15):

$$\overline{U_{t,i}(t)} = \frac{1}{a^2}\left[(1+a^2)\overline{U_{e,i}(t)}^2 - \overline{U_{e,i}(t)^2}\right]^{\frac{1}{2}} \tag{4.19}$$

where $\overline{U_{e,i}(t)}$ is the instantaneous effective mean flow calculated based on cyclic analysis.

A time and ensemble average tangential mean velocity is given by:

$$\overline{U_t} = \frac{1}{W}\frac{1}{N}\sum_{j=1}^{W}\sum_{i=1}^{N}\overline{U_{t,i}(t)} \tag{4.20}$$

where N is the number of cycles.

4.2.2 Turbulence intensity

The axial, radial and tangential turbulence intensities are equal to $u'=(\overline{u^2})^{\frac{1}{2}}$.

Ensemble Averaging Method

The expression of the turbulence intensity u' is given by (refer to equation 4.13):

$$u'(t) = \frac{1}{a}\left(\frac{\sum_{i=1}^{N} U_{e,i}^2(t)}{N} - \left(\frac{\sum_{i=1}^{N} U_{e,i}(t)}{N}\right)^2\right)^{\frac{1}{2}} \tag{4.21}$$

The time averaged turbulence intensity is calculated as follows:

$$u' = \left[\frac{1}{W}\sum_{j=1}^{W} u'^2(t)\right]^{\frac{1}{2}} \tag{4.22}$$

Cyclic Analysis Method

The turbulence intensity u' at time t in the i^{th} cycle is defined as:

$$u_i'(t) = \frac{1}{a}\left[\overline{U_{e,i}(t)^2} - \overline{U_{e,i}(t)}^2\right]^{\frac{1}{2}} \tag{4.23}$$

The time and ensemble average turbulence intensity is calculated as follows:

$$u' = \left[\frac{1}{W}\frac{1}{N}\sum_{j=1}^{W}\sum_{i=1}^{N} u_i'^2(t)\right]^{\frac{1}{2}} \tag{4.24}$$

4.2.3 Taylor microscale

The turbulence intensity is generally low (less than 10% of the mean flow, see chapter 5), therefore the structure of turbulent eddies is considered nearly frozen during their convection past the measuring probe (Taylor approximation).

Ensemble Averaging Method

The ensemble averaged Taylor microscale λ can be approximated by:

$$\lambda(t) = \frac{u'(t)\overline{U_i(t)}}{\left[\overline{\left(\frac{\partial u(t)}{\partial t}\right)^2}\right]^{\frac{1}{2}}} \tag{4.25}$$

where $\frac{\partial u(t)}{\partial t}$ is the derivative of the instantaneous fluctuation with respect to time. The time averaged Taylor microscale is calculated as follows,

$$\lambda = \left[\frac{1}{W}\sum_{j=1}^{W}\lambda^2(t)\right]^{\frac{1}{2}} \tag{4.26}$$

Cyclic Analysis Method

The Taylor microscale at a given time t of the i^{th} cycle is approximated by:

$$\lambda_i(t) = \frac{u_i'(t)\overline{U_{t,i}(t)}}{\left[\left(\frac{\partial u_i(t)}{\partial t}\right)^2\right]^{\frac{1}{2}}} \tag{4.27}$$

The time and ensemble average Taylor microscale (cyclic analysis method) is given as follows:

$$\lambda = \left[\frac{1}{W}\frac{1}{N}\sum_{j=1}^{W}\sum_{i=1}^{N}\lambda_i^2(t)\right]^{\frac{1}{2}} \tag{4.28}$$

Table 4.1: Axial, radial and tangential ensemble average turbulence intensity (location: quarter radius from center and valve lift=7mm).

Time	$\sqrt{(\overline{u_t^2})}$	$\sqrt{(\overline{u_a^2})}$	$\sqrt{(\overline{u_r^2})}$
20.11	3.18	2.93	3.06
27.79	2.77	2.68	2.64
35.47	2.48	2.57	2.46
43.15	2.53	2.47	2.41
50.83	2.21	2.32	2.45
58.51	1.78	1.85	1.82
66.19	1.73	1.81	1.71
73.87	1.83	1.74	1.68
81.55	1.61	1.65	1.55
89.23	1.44	1.51	1.46

Table 4.2: Axial, radial and tangential ensemble average turbulence intensity (location: quarter radius to wall and valve lift=7mm).

Time	$\sqrt{(\overline{u_t^2})}$	$\sqrt{(\overline{u_a^2})}$	$\sqrt{(\overline{u_r^2})}$
20.11	2.28	2.37	2.21
27.79	2.11	2.14	2.10
35.47	1.74	1.76	2.01
43.15	2.06	2.09	2.03
50.83	1.60	1.68	1.85
58.51	1.70	1.64	1.73
66.19	1.44	1.61	1.58
73.87	1.60	1.48	1.67
81.55	1.65	1.63	1.55
89.23	1.23	1.31	1.38

Table 4.3: Axial, radial and tangential ensemble average turbulence intensity (location: mid-radius and valve lift=7mm).

Time	$\sqrt{(\overline{u_t^2})}$	$\sqrt{(\overline{u_a^2})}$	$\sqrt{(\overline{u_r^2})}$
20.11	3.06	3.21	3.17
27.79	2.49	2.57	2.61
35.47	2.42	2.45	2.49
43.15	2.06	2.14	2.16
50.83	2.29	2.18	2.11
58.51	1.94	1.95	1.91
66.19	1.80	1.87	1.88
73.87	1.92	1.86	1.93
81.55	1.57	1.56	1.59
89.23	1.45	1.44	1.41

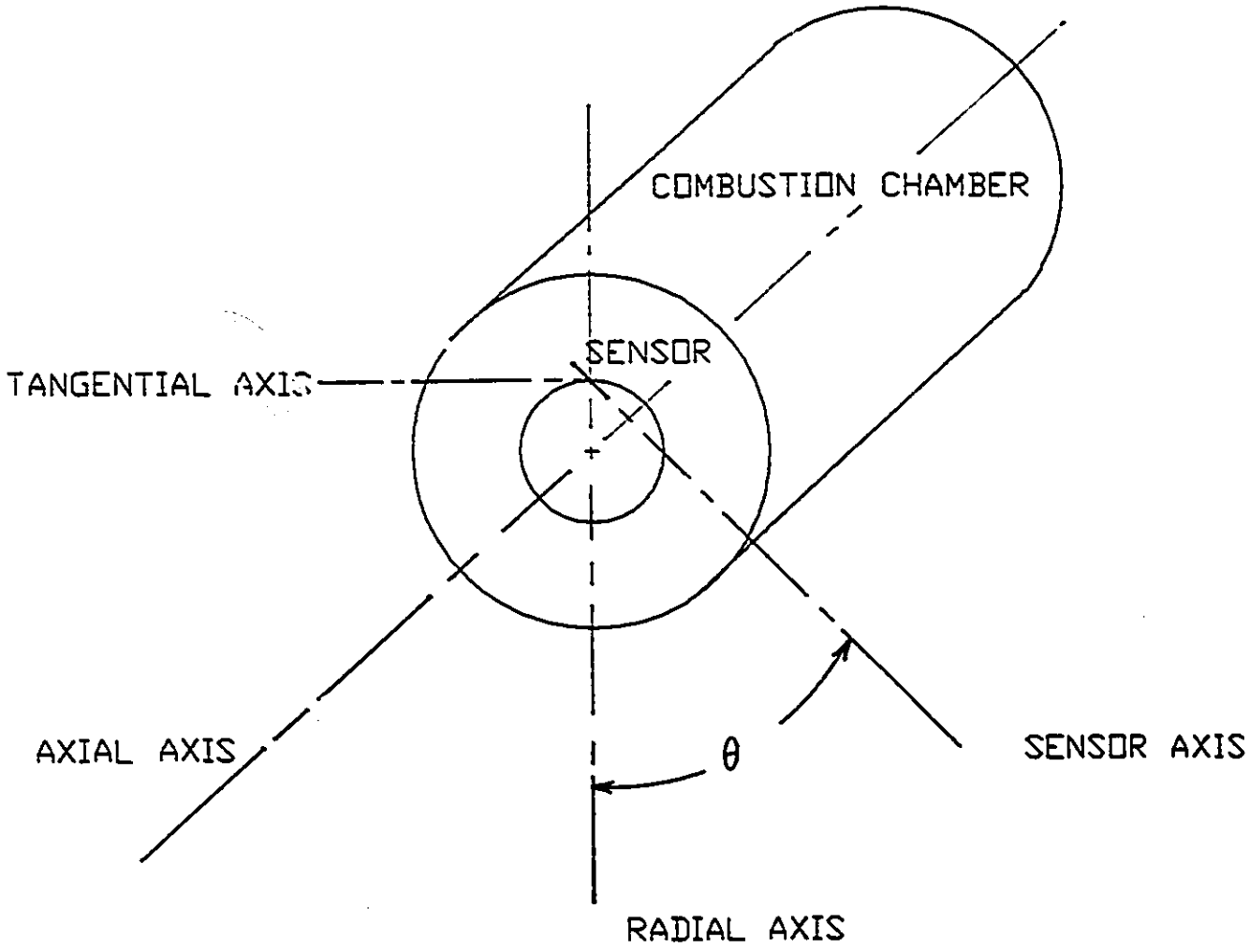

Figure 4.1: Orientation of the Hot Wire Sensor with Respect to the Vessel.

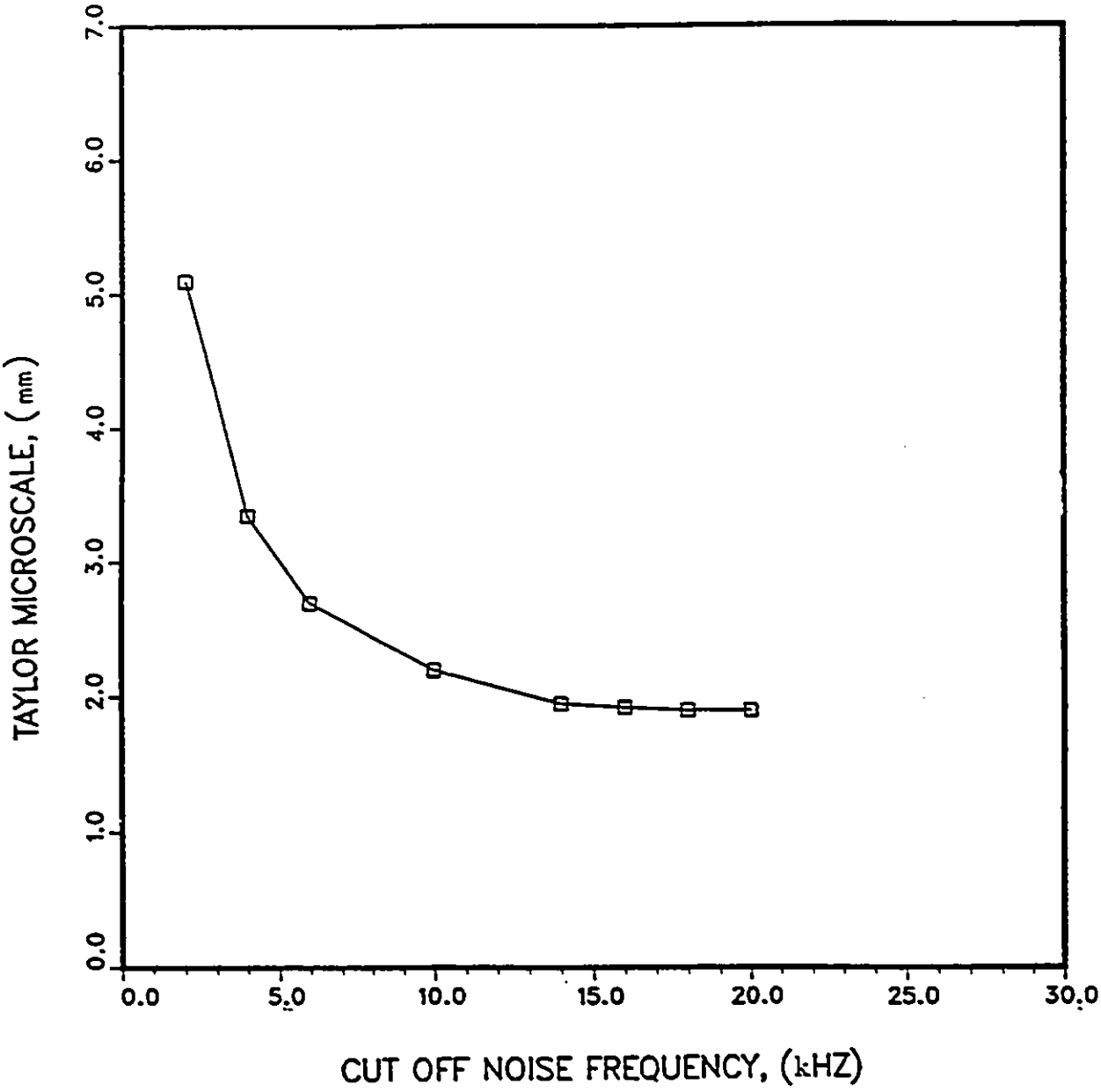

Figure 4.2: Taylor Microscale versus the Cut-off Noise Frequency, (Location: Quarter Radius from Center, Valve Lift = 7 mm).

Chapter 5

RESULTS AND DISCUSSIONS

5.1 Cold Flow

Turbulence characteristics of air swirl in a constant-volume cylindrical chamber with a shrouded intake valve were investigated using a single hot wire anemometer. To determine the direction of flow, the hot wire probe was rotated in intervals of 45 deg (see Fig. 4.1). At $\theta = 0$ deg, the sensor axis coincides with the vessel radius. Figs. 5.1 to 5.3 show the variation of the ensemble averaged root-mean square of the effective velocity with time for angles θ of 0, 45 and 90 deg for three locations and valve lift equal to 7 mm.

Comparing the three curves it can be seen that this value is highest for $\theta = 0$ and lowest for $\theta = 90$ deg.

Referring again to Figs. 5.1 to 5.3 and to equation 4.1, the axial and radial mean velocities are considered negligible compared to the tangential component. It is notable that the flow is fully tangential even though locations of measurement are not aligned, (see Fig 3.2). This is an indication of a swirling flow. In order to investigate whether turbulence in the combustion chamber is isotropic, the hot wire was rotated. The two angles of rotation used were $\theta = 0$ deg and $\theta = 90$ deg. Expressions for axial, radial, and tangential root mean square fluctuations were developed in chapter 4. These fluctuations were found to be nearly equal (Tables 4.1 to 4.3), implying a nearly isotropic turbulence structure.

5.1.1 Temperature

Temperature versus time was plotted for different locations (quarter radius from center, mid-radius and quarter radius from wall). The decay in temperature shown in Fig. 3.6, results directly from the wall heat transfer effect. Fig. 3.6 also indicates that there are significant temperature gradients within the vessel resulting from a combination of charging procedure (compression

effect) and wall heat transfer. Temperature is the lowest for the locations of measurement closest to the wall.

5.1.2 Mean Flow

Results (Tables 5.2 to 5.4) show that the mean flow is insensitive to the cut-off frequency when the latter is varied from 0.2 to 0.8 kHz. Also, the mean flow calculated using ensemble averaging is identical to the mean flow calculated using cyclic analysis. For the three locations, Figs. 5.4 to 5.6 show that the mean flow varies with a change in the valve lift. Fig. 5.7 shows that at V.L. = 7 mm the mean flow is highest at mid radius. It drops at quarter radius to center and it is also low at quarter radius from the wall due to the wall effect. At V.L. = 12 mm, Fig. 5.8 indicates that the mean flow velocity is highest at quarter radius to center, then lower at mid-radius and quarter radius from wall. From Figs. 5.7 and 5.8 it can be concluded that as the valve lift decreases, the flow approaches a solid body rotation. The ratio of standard deviation of the mean value to mean flow calculated using cyclic analysis is shown in Fig. 5.9. Results for the mean flow indicate that the ratio increases as the flow decays. The trend of this ratio is the same for both valve lifts at all locations.

5.1.3 Turbulence Intensity

Tables 5.5 to 5.7 show the values of the turbulence intensity used in this analysis. The turbulence intensity is shown in Figs. 5.10 to 5.20. At the 3 locations and for both valve lifts, the ensemble averaging calculation indicated a higher turbulence intensity than cyclic analysis. This is due to the cycle-to-cycle fluctuation of the mean. In the ensemble averaging a fraction of the mean is included in the calculation of the turbulence intensity. These figures also indicate that the turbulence intensity is sensitive to the cut-off frequency. At quarter radius to center (Fig. 5.16), the valve lift does not influence the turbulence intensity. However, at mid-radius and quarter radius from wall the data indicate higher turbulence intensity at lower valve lift (see Figs. 5.17 and 5.18). For both valve lifts the turbulence intensity is the highest at quarter radius from the center. However, it is about the same at the two other locations (see Figs. 5.19 and 5.20). Fig. 5.21 indicates that the ratio of standard deviation of the turbulence intensity to the turbulence intensity value increases as the flow decays and it is independent of valve lift.

5.1.4 Taylor Microscale

Tables 5.8 to 5.10 show the values of Taylor microscale obtained. The Taylor microscale trend is shown in Figs. 5.22 to 5.32. At the three locations and for both valve lifts, the ensemble averaging calculation indicates a higher Taylor microscale than cyclic analysis. Also, these figures indicate that Taylor microscale is sensitive to the cut-off frequency. At mid-radius, Fig. 5.29 shows a higher Taylor microscale at lower valve lift. At the two other locations, the Taylor microscale was about the same for both valve lifts (see Figs. 5.28 and 5.30). Fig. 5.31 shows that at V.L. =7 mm, the Taylor microscale is independent of location. However, at V.L. =12 mm (Fig. 5.32), it is higher at quarter radius to center. The ratio of standard deviation of Taylor microscale to Taylor microscale value is shown in Fig. 5.33. At mid-radius the different valve lifts result in a substantial difference early in the flow. Then, as the flow decays the difference becomes smaller. At quarter radius to center and from wall, this ratio is the same for both valve lifts. This ratio decays as the flow decays.

5.1.5 Ratio of Turbulence Intensity to Mean Flow

The ratio of turbulence to mean flow are shown in Figs. 5.34 to 5.36. This ratio decays with time for both valve lifts and the three locations. For V.L. = 7 mm at quarter radius from center and mid-radius, this ratio decays at a faster rate initially, then 35 ms from the intake valve closure it decays at a low rate. This indicates that initially the jet is dominant, while later the wall effect is more important (see Figs. 5.34 to 5.36). At quarter radius from wall, the wall is dominant all the time (refer to Fig. 5.36). For V.L. = 12 mm the wall effect is dominant (refer to Figs. 5.34 to 5.36).

For the condition tested, changing the valve lift has changed the spatial variation of turbulence characteristics. The turbulence intensity is higher at lower valve lift at quarter radius from wall and mid-radius. However, it is independent of valve lift at a quarter radius from center. At mid-radius and quarter radius to wall, the mean flow is higher at lower valve lift and it is independent of valve lift at quarter radius to wall and mid-radius. The Taylor microscale at mid-radius is higher at lower valve lift and it is a weak function of the valve lift at the two other locations.

5.2 Combustion

The location of ignition relative to the small scale structure varies from cycle to cycle. In the Tennekes model, the initial flame propagates rapidly if ignition occurs in the vortex tubes of size η (Kolmogorov scale). In the regions between the vortex tubes characterized by the Taylor microscale, the flame speed (laminar flame speed) is lower. These cyclic variations in initial flame speed result in cyclic variation in combustion performance, which are only due to the randomness of ignition location and do not take into account heat transfer to electrodes.

For a mixture of propane and air at equivalence ratio of 0.8, the laminar flame speed is to be 0.3 m/s (Metghalchi et al (1982)). Under the present conditions, the laminar flame speed is slightly sensitive to the pressure at ignition.

5.3 Combustion pressure

The mean delay time is defined as the average time a flame takes to reach the vortex tube. This mean delay time and its corresponding standard deviation were calculated for each operating condition using 40 cycles of combustion pressure traces. Operating conditions and combustion characteristics are

shown in Table 5.11. Case 2 (valve lift = 7mm and ignition time = 28ms) was tested with 70 cycles, which compared to 40 cycles show no statistical difference . As ignition occurs later in the cycle, the mean combustion duration is longer because the flow has decayed . The standard deviation in the delay time was estimated using combustion pressure traces. The time of occurrence of a given pressure was recorded (see Fig. 5.37) and the standard deviation of these times was calculated. These values are plotted in Fig. 5.38. This figure shows that the standard deviation for a given operating condition increases as pressure increases. The extrapolated value of standard deviation of delay time at ignition (pressure = 3.26 bar) is between 0.5 and 0.6 ms and the value at peak pressure is between 0.75 and 0.90 ms. It is obvious that about 70 % of the value of the standard deviation at the peak pressure occurs at ignition. This indicates that cyclic variations at ignition contribute the most to cyclic variations. It is also notable that even though turbulence intensity and mean flow decay by almost 50% while the Taylor microscale remains constant as ignition time is delayed (see table 5.11), the standard deviation at ignition changes by only 20 %. This suggests that the standard deviation at ignition is a weak function of mean flow and turbulence intensity and a strong function of Taylor microscale as implied by the Tennekes model.

5.4 Validity of Tennekes model

If ignition occurs at a distance r from the vortex tube, the time required for the flame to reach the dissipative region is $\frac{r}{S_L}$, where S_L is the laminar flame speed. For each condition, two cycles corresponding to an ignition close to the vortex tube and two cycles corresponding to an ignition farthest from the dissipative region and a mean pressure trace over the 40 cycles were plotted (see Figs. 5.39 and 5.40). The maximum, minimum and mean time corresponding to a pressure of 4 bars were recorded. The maximum delay time t_{max} is defined as the difference between the maximum and minimum time. According to Tennekes model, this maximum delay time corresponds to a distance $\frac{\lambda}{2}$ travelled by the flame. In other words, the travelled distance $\frac{\lambda}{2}$ is equal to the laminar flame speed S_l times the maximum delay time t_{max}. The maximum delay time was found to vary between 2.20 ms and 2.68 ms (see table 5.12). Therefore, the values of λ are between 1.61 mm and 1.32 mm. These values are about 20 % less than the value found using the hot wire anemometer (cyclic analysis method) (see table 5.13). The mean delay time t_{mean} is defined as the difference between the mean and minimum time (ignition occurs at vortex tube). This mean delay time was found to vary between 1.33 ms and 0.97 ms.

The mean delay time t_{mean} and the standard deviation σ were respectively compared to the terms $\frac{\lambda}{5S_L}$ and $\frac{\lambda}{10S_L}$ (refer to Tables 5.14 and 5.15). It can be concluded that the mean delay time and the standard deviation correlate with the term $\frac{\lambda}{S_L}$. It is found that the standard deviation is approximately equal (within a maximum error of 15%) to $\sigma = \frac{\lambda}{10S_L}$, and the mean delay time can be approximated by (within a maximum error of 25%) to $t_{mean} = \frac{\lambda}{5S_L}$.

Table 5.1: Initial Condition for the Cold Flow

Valve Opening Time (ms)	Charging Pressure (bar)	Inlet Temperature deg C
75	3.26	21.5

Table 5.2: Tangential Mean Flow at Quarter Radius from Center

Time (ms)	Tangential Mean Flow $\bar{U}(m/s)$				
	$V.L. = 7mm$			$V.L. = 12mm$	
	E.A.	C.A. C.F. = 0.2 KHz	C.A. C.F. = 0.8 KHz	E.A.	C.A. C.F. = 0.2 KHz
20.11	20.79	20.79	20.79	23.82	23.82
27.79	19.99	19.99	19.99	22.78	22.78
35.47	20.02	20.02	20.02	20.88	20.88
43.15	17.62	17.62	17.62	18.70	18.70
50.83	15.10	15.10	15.10	17.11	17.11
58.51	14.33	14.33	14.33	16.07	16.07
66.19	14.09	14.09	14.08	14.87	14.87
73.87	12.80	12.80	12.80	14.03	14.03
81.55	11.33	11.33	11.33	13.08	13.08
89.23	10.18	10.18	10.18	11.87	11.87

Table 5.3: Tangential Mean Flow at Quarter Radius from Center

Time (ms)	Tangential Mean Flow $U(m/s)$				
	$V.L. = 7mm$			$V.L. = 12mm$	
	E.A.	C.A. C.F. = 0.2 KHz	C.A. C.F. = 0.8 KHz	E.A.	C.A. C.F. = 0.2 KHz
20.11	26.67	26.67	26.67	19.42	19.42
27.79	24.09	24.09	24.09	18.52	18.52
35.47	23.20	23.20	23.20	17.35	17.35
43.15	20.44	20.44	20.44	16.06	16.06
50.83	19.60	19.60	19.60	14.94	14.94
58.51	17.27	17.27	17.27	14.37	14.37
66.19	17.02	17.02	17.02	13.64	13.64
73.87	16.47	16.47	16.47	12.33	12.33
81.55	14.78	14.78	14.78	11.66	11.66
89.23	14.28	14.28	14.28	11.32	11.32

Table 5.4: Tangential Mean Flow U at Quarter Radius to Wall

Time (ms)	Tangential Mean Flow, $U(m/s)$			
	$V.L. = 7mm$		$V.L. = 12mm$	
	E.A.	C.A. C.F. = 0.2 KHz	E.A.	C.A. C.F. = 0.2 KHz
20.11	24.58	24.58	16.98	16.98
27.79	20.51	20.51	15.94	15.94
35.47	18.62	18.62	14.81	14.81
43.15	20.48	20.48	14.10	14.10
50.83	20.39	20.39	14.11	14.11
58.51	17.42	17.42	14.11	14.11
66.19	15.12	15.12	13.49	13.49
73.87	15.05	15.02	12.62	12.62
81.55	16.02	16.02	11.85	11.85
89.23	15.71	15.71	11.21	11.21

Table 5.5: Turbulence Intensity u at Quarter Radius from Center

Time (ms)	Turbulence Intensity, $u(m/s)$				
	$V.L. = 7mm$			$V.L. = 12mm$	
	E.A.	C.A. C.F. = 0.2 KHz	C.A. C.F. = 0.8 KHz	E.A.	C.A. C.F. = 0.2 KHz
20.11	3.18	2.06	1.25	3.38	1.81
27.79	2.77	1.69	1.03	3.02	1.65
35.47	2.48	1.56	0.95	2.72	1.47
43.15	2.53	1.50	0.86	2.36	1.33
50.83	2.21	1.29	0.72	2.44	1.17
58.51	1.78	1.03	0.56	2.33	1.09
66.19	1.73	0.97	0.54	2.31	1.00
73.87	1.83	0.95	0.52	1.99	0.98
81.55	1.61	0.84	0.46	1.90	0.86
89.23	1.44	0.71	0.35	1.66	0.76

Table 5.6: Turbulence Intensity u at mid-Radius

Time (ms)	Turbulence Intensity, $u(m/s)$				
	$V.L. = 7mm$			$V.L. = 12mm$	
	E.A.	C.A. C.F. = 0.2 KHz	C.A. C.F. = 0.8 KHz	E.A.	C.A. C.F. = 0.2 KHz
20.11	3.06	1.89	1.16	1.81	0.88
27.79	2.49	1.43	0.87	1.72	0.93
35.47	2.42	1.11	0.71	1.26	0.92
43.15	2.06	1.13	0.70	1.30	0.70
50.83	2.29	1.08	0.66	1.20	0.63
58.51	1.94	0.98	0.61	1.32	0.63
66.19	1.80	0.74	0.44	1.21	0.61
73.87	1.92	0.74	0.42	1.36	0.58
81.55	1.57	0.77	0.45	1.19	0.50
89.23	1.45	0.69	0.43	1.13	0.42

Table 5.7: Turbulence Intensity u at Quarter Radius to Wall

Time (ms)	Turbulence Intensity, $u(m/s)$			
	$V.L. = 7mm$		$V.L. = 12mm$	
	E.A.	C.A. C.F. = 0.2 KHz	E.A.	C.A. C.F. = 0.2 KHz
20.11	2.28	1.34	1.70	0.93
27.79	2.11	1.22	1.63	0.88
35.47	1.74	1.11	1.34	0.82
43.15	2.06	1.05	1.25	0.71
50.83	1.60	0.93	1.37	0.69
58.51	1.70	1.00	1.32	0.74
66.19	1.44	0.78	1.15	0.69
73.87	1.60	0.80	1.07	0.65
81.55	1.65	0.76	1.05	0.63
89.23	1.23	0.64	1.01	0.64

Table 5.8: Taylor Microscale λ at Quarter Radius from Center

Time (ms)	Taylor Microscale, $\lambda(mm)$				
	$V.L. = 7mm$			$V.L. = 12mm$	
	E.A.	C.A. C.F. = 0.2 KHz	C.A. C.F. = 0.8 KHz	E.A.	C.A. C.F. = 0.2 KHz
20.11	2.88	1.85	1.15	3.55	1.87
27.79	3.09	1.85	1.16	3.47	1.87
35.47	3.07	1.92	1.19	3.48	1.86
43.15	3.27	1.91	1.12	3.25	1.81
50.83	3.13	1.79	1.04	3.61	1.71
58.51	2.87	1.64	0.92	3.80	1.74
66.19	2.93	1.62	0.92	4.01	1.70
73.87	3.13	1.60	0.90	3.66	1.76
81.55	2.89	1.47	0.84	3.60	1.60
89.23	2.83	1.37	0.71	3.30	1.48

Table 5.9: Taylor Microscale λ at Mid-Radius

Time (ms)	Taylor Microscale, $\lambda(mm)$				
	$V.L. = 7mm$			$V.L. = 12mm$	
	E.A.	C.A. C.F. = 0.2 KHz	C.A. C.F. = 0.8 KHz	E.A.	C.A. C.F. = 0.2 KHz
20.11	3.46	2.11	1.31	2.59	1.17
27.79	3.47	1.96	1.21	1.80	0.92
35.47	4.19	1.90	1.22	1.22	0.85
43.15	3.40	1.84	1.15	1.97	1.00
50.83	3.84	1.79	1.10	2.40	1.16
58.51	3.66	1.81	1.13	1.92	1.28
66.19	3.93	1.58	0.95	2.97	1.37
73.87	4.75	1.80	1.01	3.46	1.34
81.55	3.49	1.67	0.98	2.94	1.12
89.23	3.06	1.43	0.90	2.97	1.02

Table 5.10: Taylor Microscale λ at Quarter Radius to Wall

Time (ms)	Taylor Microscale, $\lambda(mm)$			
	$V.L. = 7mm$		$V.L. = 12mm$	
	E.A.	C.A. C.F. = 0.2 KHz	E.A.	C.A. C.F. = 0.2 KHz
20.11	3.11	1.78	2.52	1.35
27.79	3.07	1.74	2.73	1.45
35.47	2.40	1.51	2.32	1.38
43.15	3.05	1.53	2.24	1.24
50.83	2.84	1.61	2.53	1.26
58.51	2.98	1.71	2.43	1.33
66.19	2.56	1.36	2.25	1.31
73.87	2.75	1.34	2.20	1.30
81.55	3.12	1.39	2.09	1.24
89.23	2.64	1.32	2.09	1.30

Table 5.11: Operating Conditions and Turbulence Parameters at Ignition (turbulence parameters are averaged using cyclic analysis method)

Operating Conditions	Mean Initial Pressure (bar)	Mean Peak Pressure (bar)	Mean Combustion Duration (ms)	Pressure Ratio P_p/P_i	Mean Flow (m/s)	Turbulence Intensity (m/s)	Taylor Microscale (mm)
V.L. = 7 mm I.T. = 28 ms	3.26	22.83	15.98	7.00	19.99	1.69	1.85
V.L. = 7 mm I.T. = 74 ms	3.14	21.47	21.88	6.74	12.80	0.95	1.60
V.L. = 12 mm I.T. = 28 ms	3.26	22.91	15.92	7.02	22.78	1.65	1.87
V.L. = 12 mm I.T. = 74 ms	3.16	21.12	23.22	6.71	14.03	0.98	1.76

Table 5.12: Maximum and Minimum Delay Time

Operating Conditions	Maximum Delay Time (ms)	Minimum Delay Time (ms)	Standard Deviation (ms)
V.L. = 7 mm I.T. = 28 ms	2.22	1.22	0.549
V.L. = 7 mm I.T. = 74 ms	2.68	1.30	0.645
V.L. = 12 mm I.T. = 74 ms	2.20	0.97	0.550
V.L. = 28 mm I.T. = 74 ms	2.55	1.33	0.706

Table 5.13: Comparison Between the Measured Taylor Microscale and the Estimated Taylor Microscale from Combustion Pressure Traces.

Operating Conditions	Taylor Microscale Deduced from Cold Flow (mm)	Taylor Microscale Estimated from Combustion (mm)
V.L. = 7 mm I.T. = 28 ms	1.85	1.33
V.L. = 7 mm I.T. = 74 ms	1.60	1.61
V.L. = 12 mm I.T. = 74 ms	1.87	1.32
V.L. = 28 mm I.T. = 74 ms	1.76	1.53

Table 5.14: Comaprison between mean time delay and the term $\frac{\lambda}{5S_t}$

Mean time delay $T_{mean}(ms)$	Taylor microscale (mm)	$\frac{\lambda}{5S_t}$ (mm)
1.22	1.85	1.23
1.30	1.60	1.06
0.97	1.87	1.24
1.33	1.76	1.17

Table 5.15: Comaprison between the standard deviation and the term $\frac{\lambda}{10S_l}$

Standard Deviation σ(ms)	Taylor microscale (mm)	$\frac{\lambda}{10S_l}$ (mm)
0.549	1.85	0.616
0.645	1.60	0.533
0.550	1.87	0.623
0.706	1.76	0.58

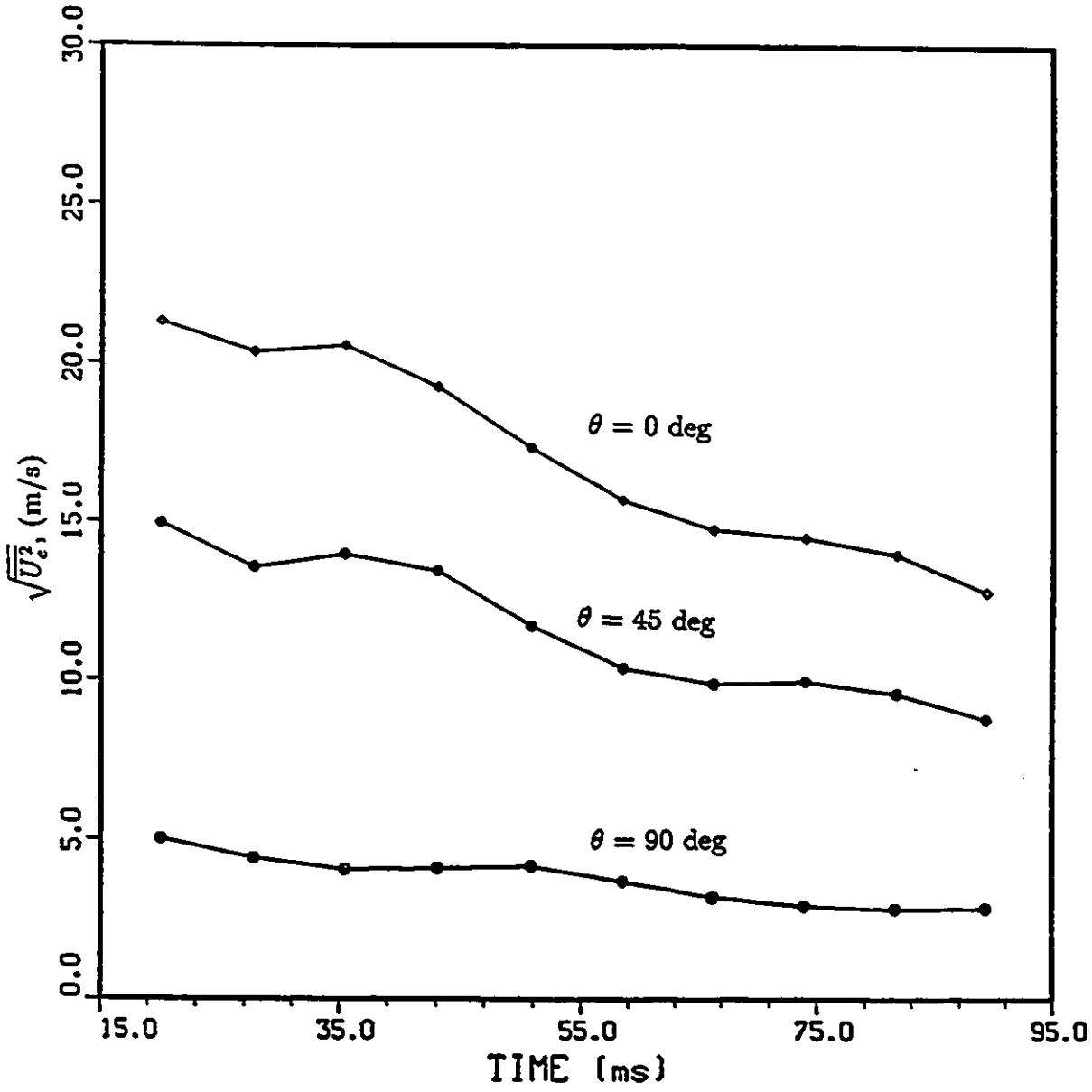

Figure 5.1: Ensemble averaged root mean square of the effective velocity versus time (location: quarter radius from center and valve lift=7mm)

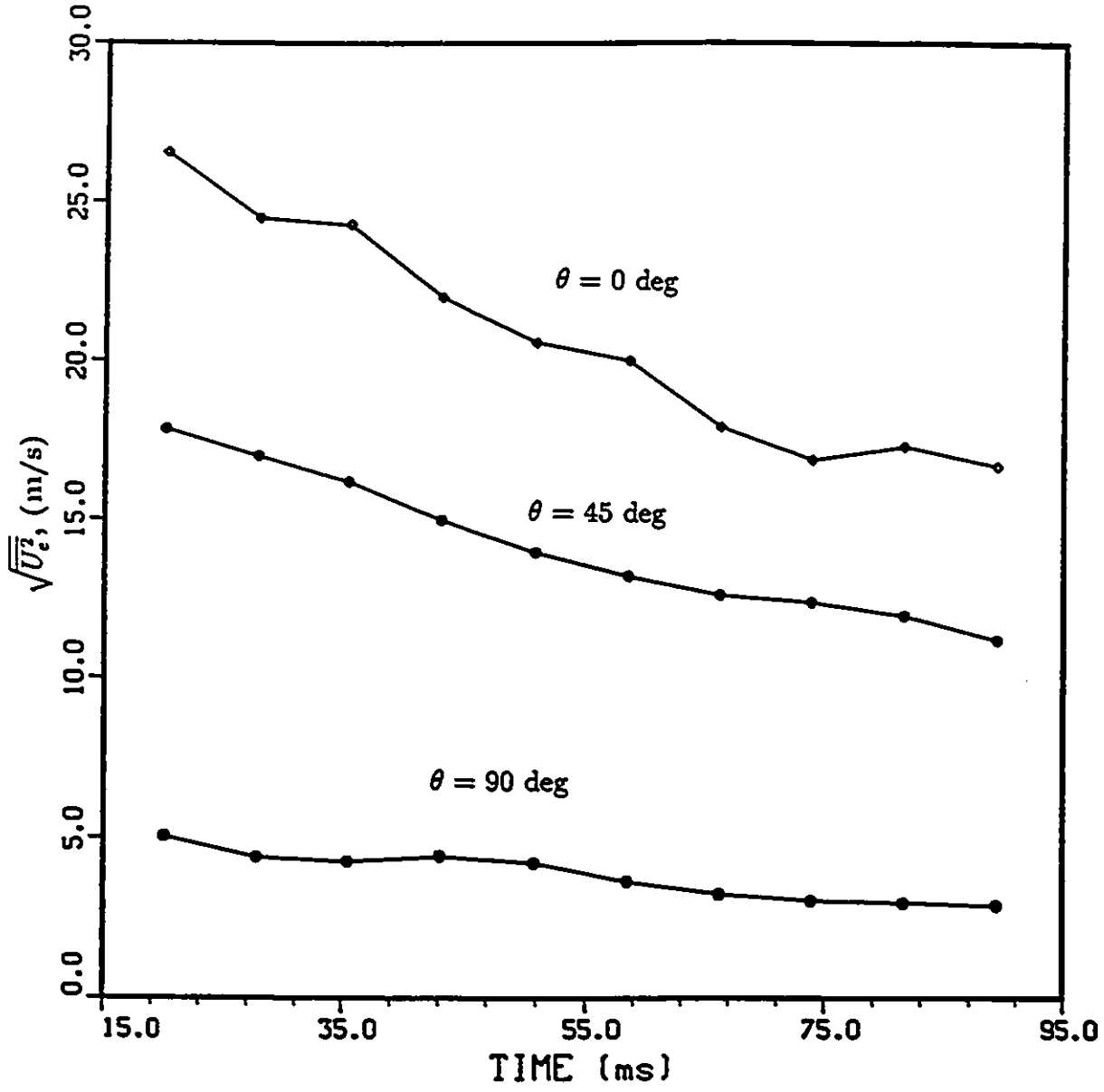

Figure 5.2: Ensemble averaged root mean square of the effective velocity versus time (location: mid-radius and valve lift=7mm)

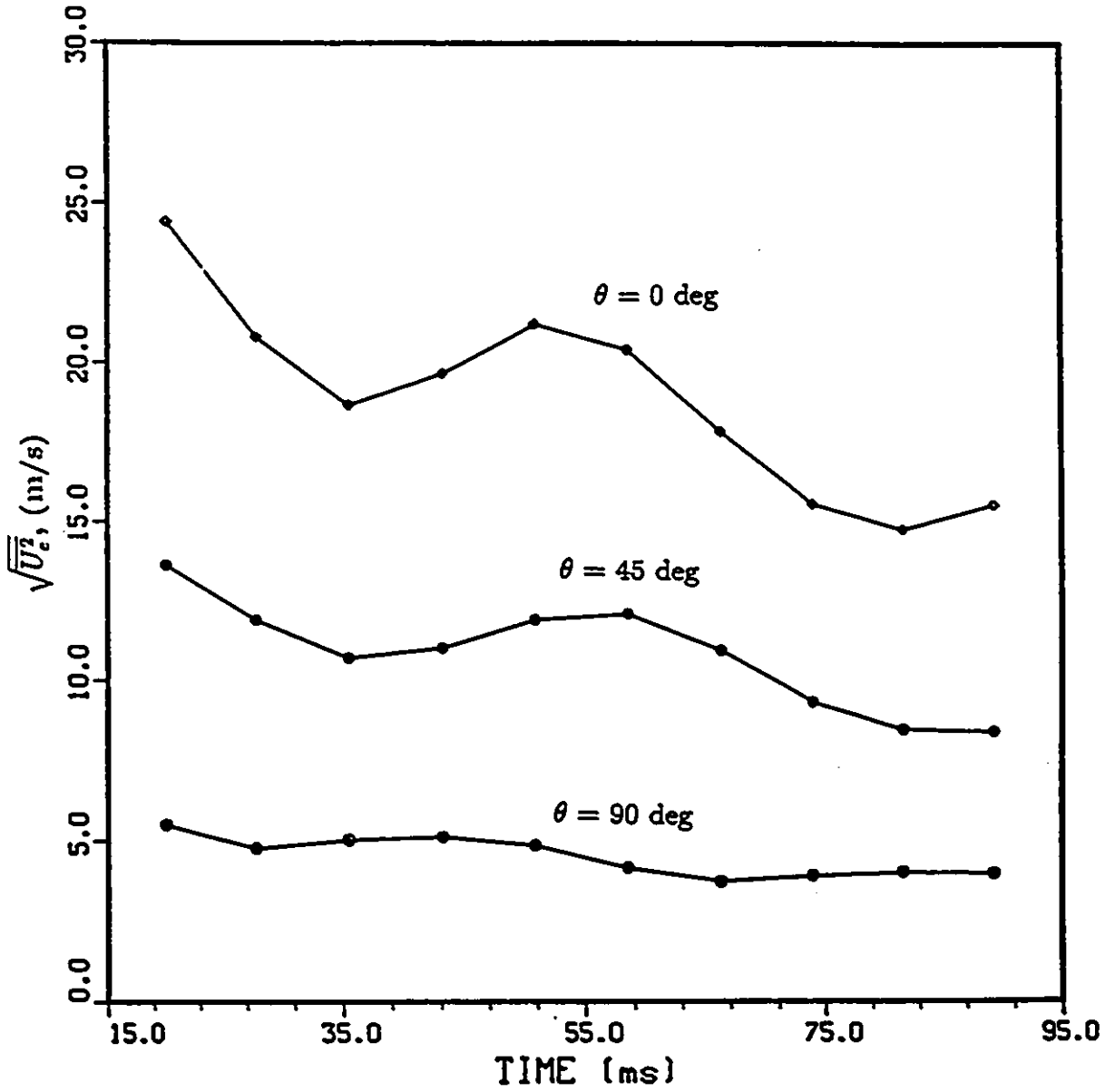

Figure 5.3: Ensemble averaged root mean square of the effective velocity versus time (location: quarter radius to wall and valve lift=7mm)

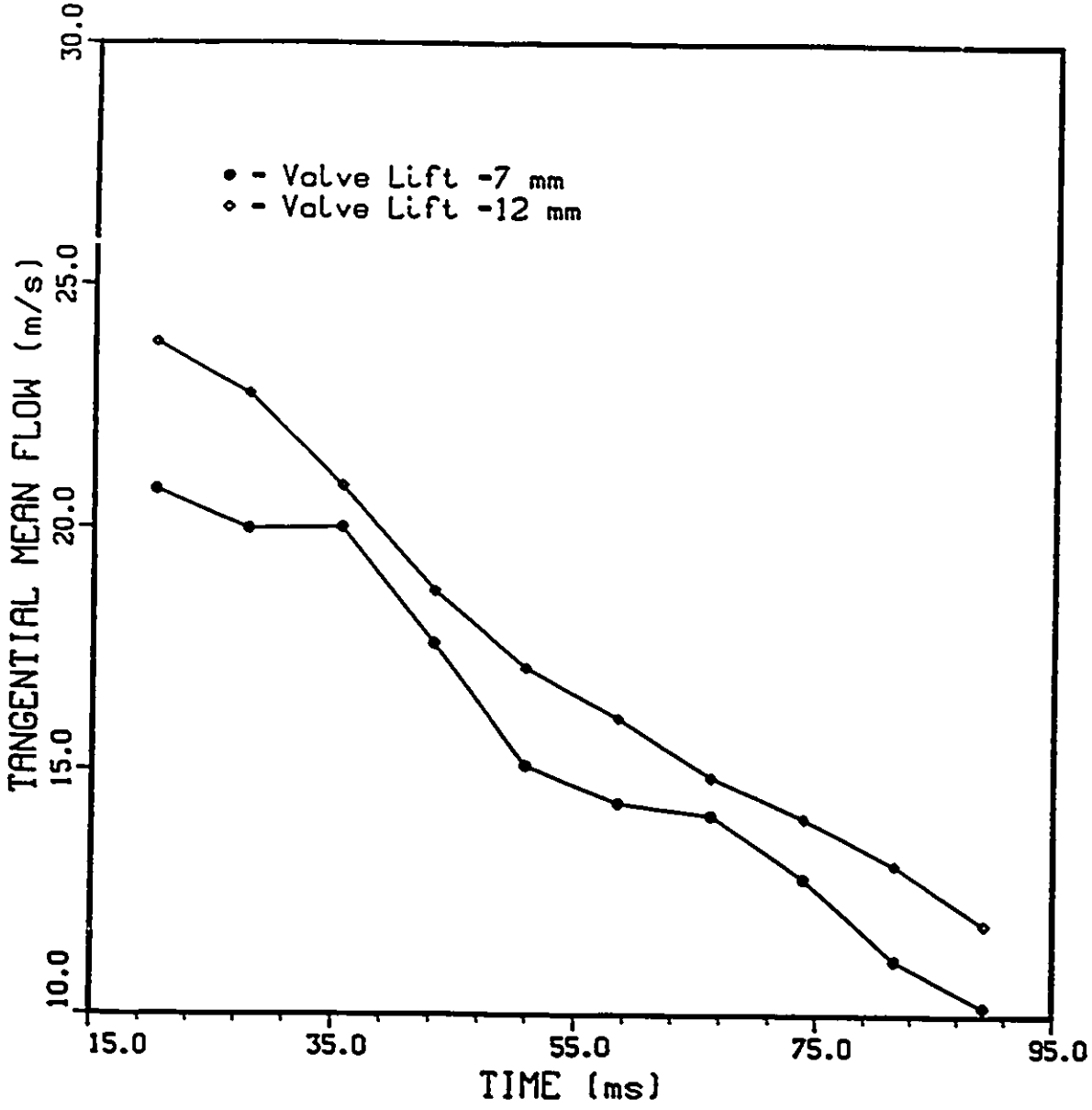

Figure 5.4: Effect of valve lift on tangential mean flow as a function of time (location: quarter radius from center)

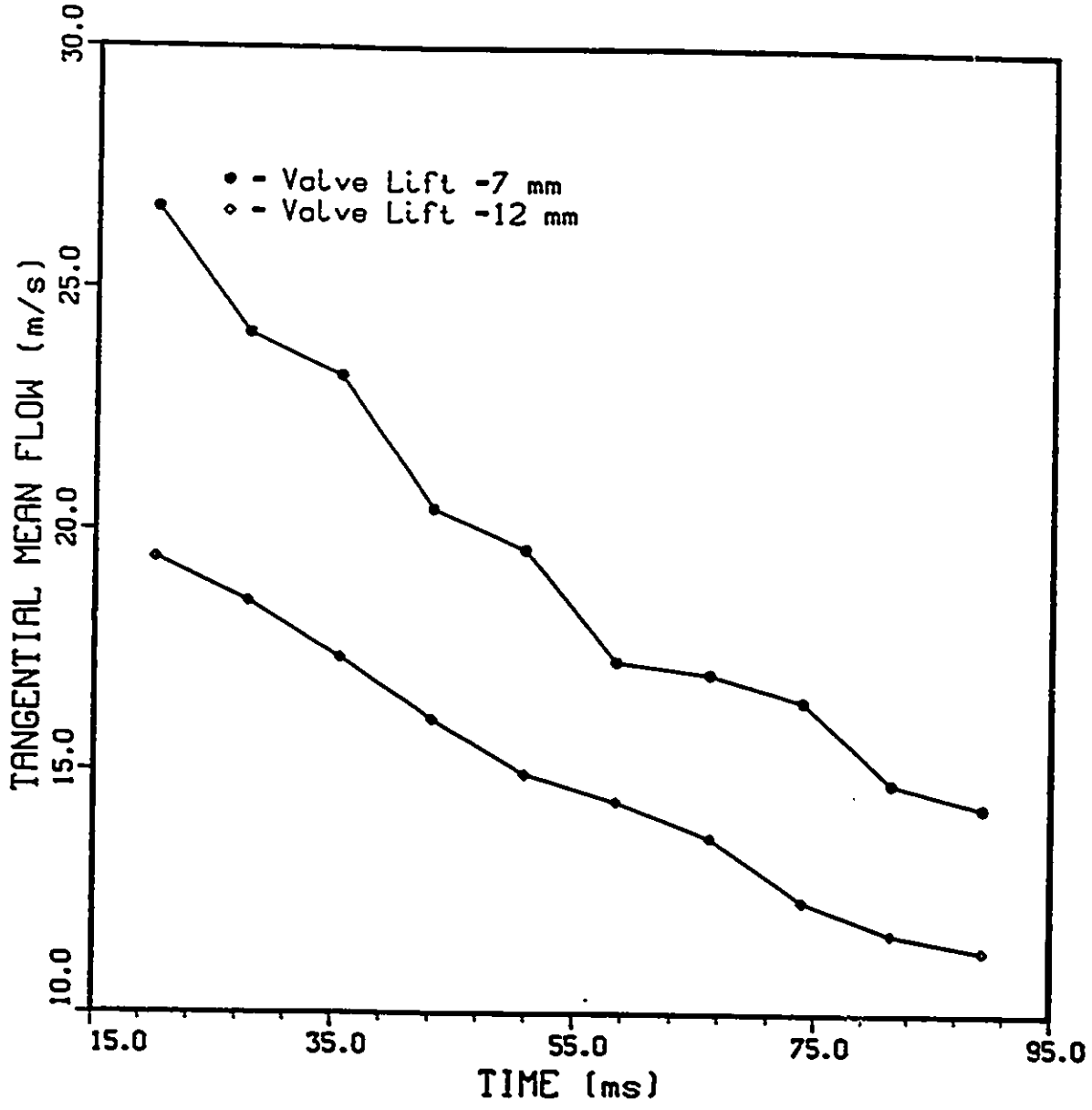

Figure 5.5: Effect of valve lift on tangential mean flow as a function of time (location: mid-radius)

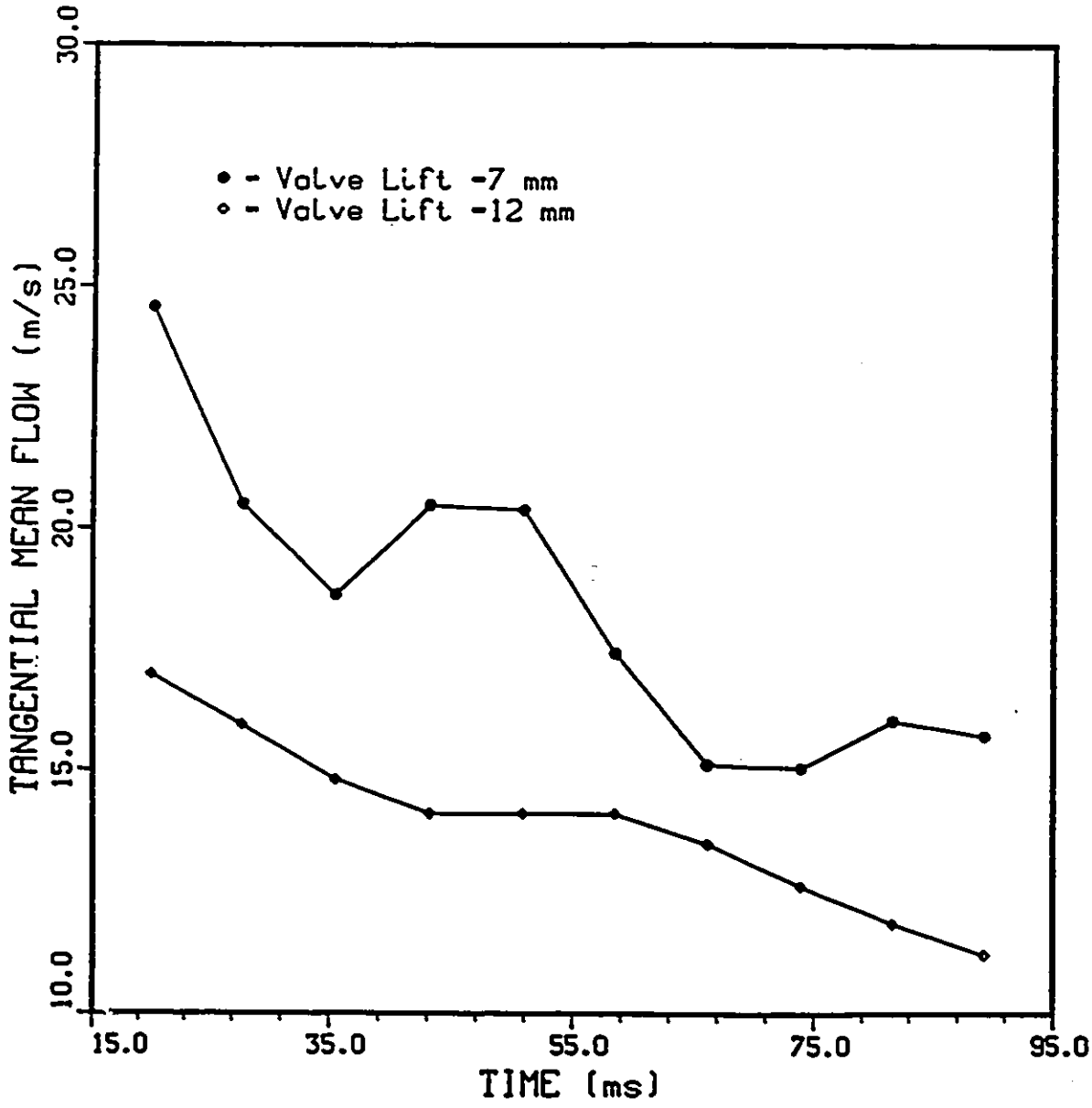

Figure 5.6: Effect of valve lift on tangential mean flow as a function of time (location: quarter radius to wall)

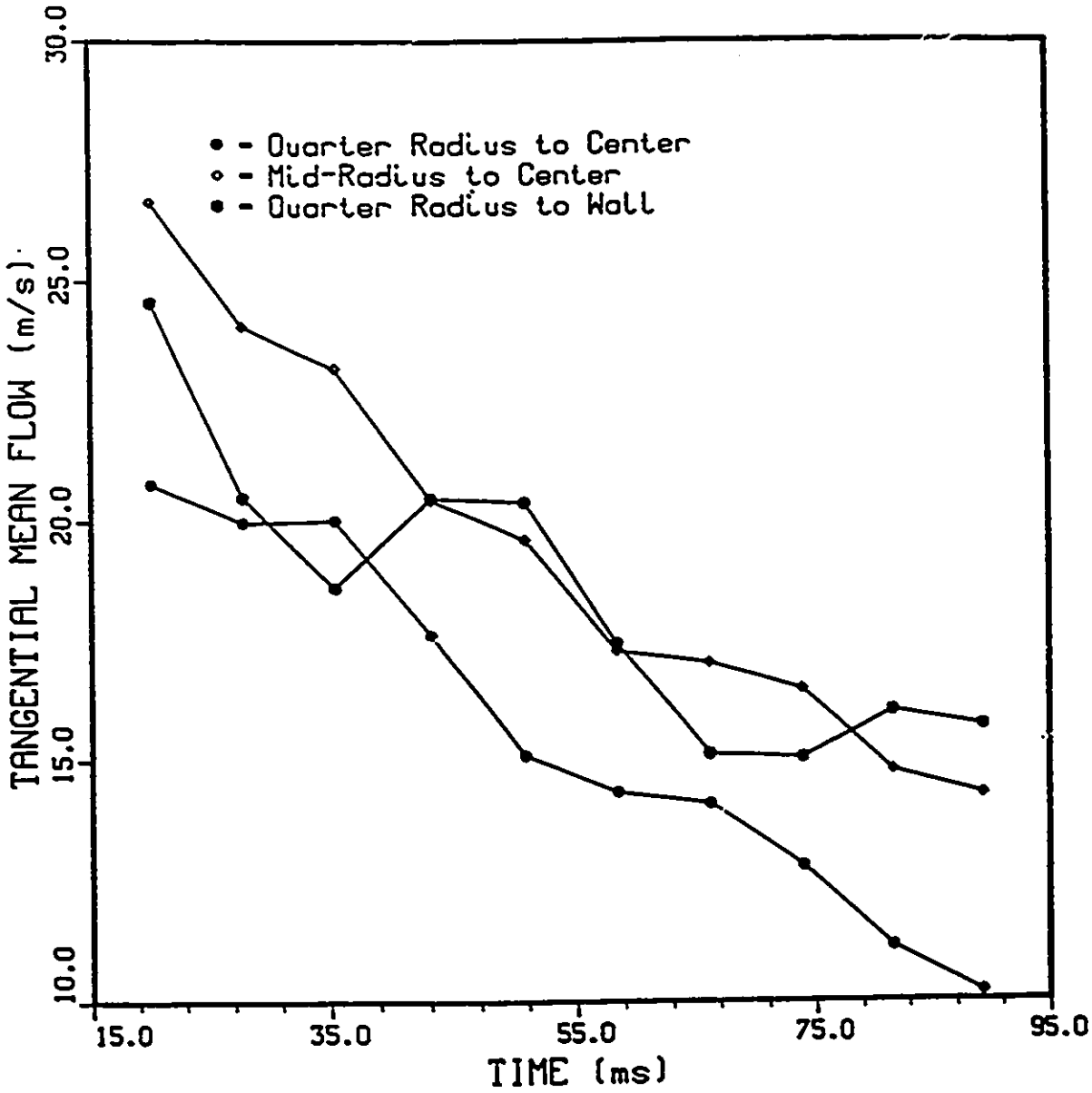

Figure 5.7: Effect of location on tangential mean flow as a function of time (CF=0.2 kHz and valve lift=7mm)

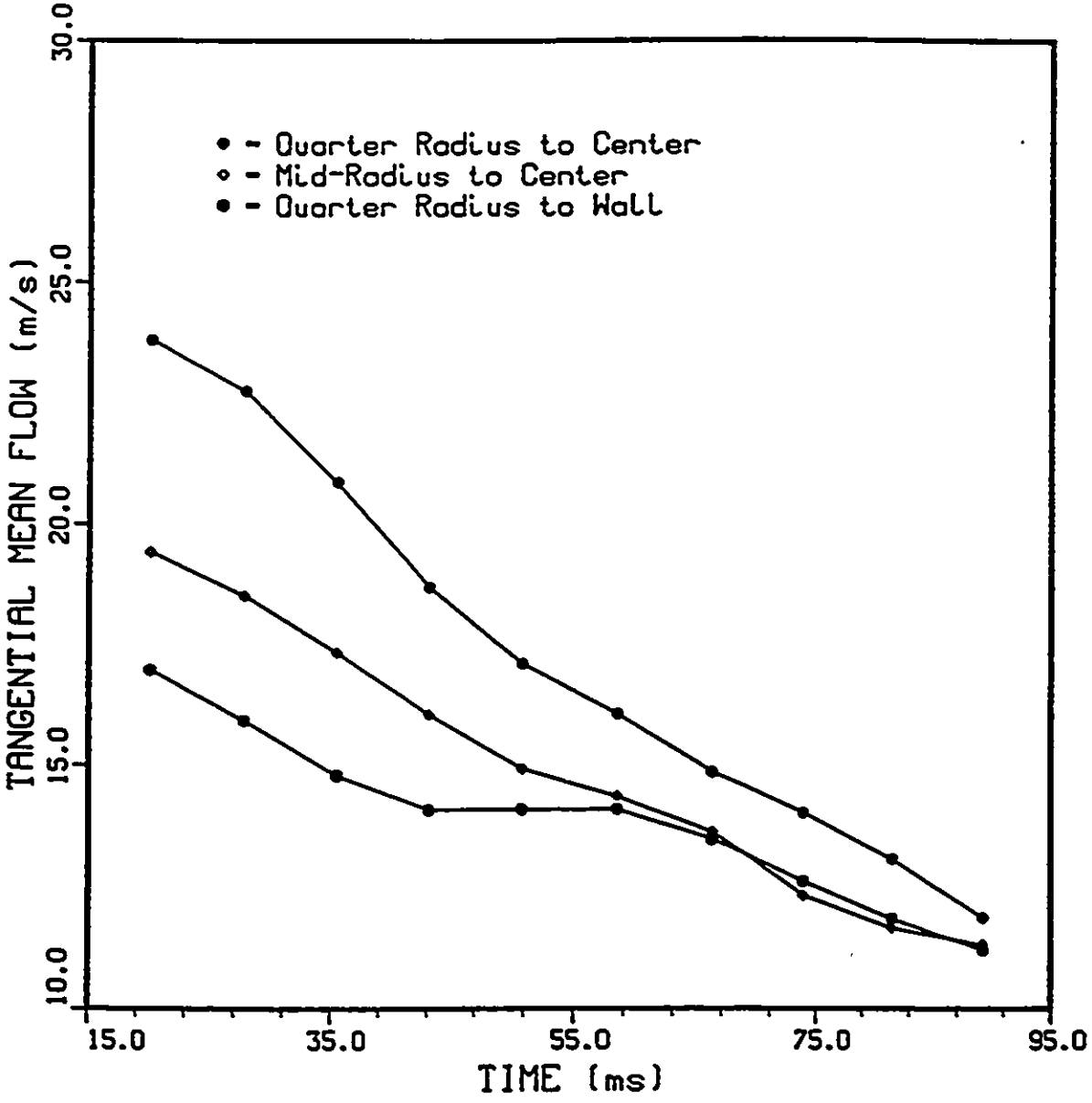

Figure 5.8: Effect of location on tangential mean flow as a function of time (CF=0.2 KHz and valve lift=12mm)

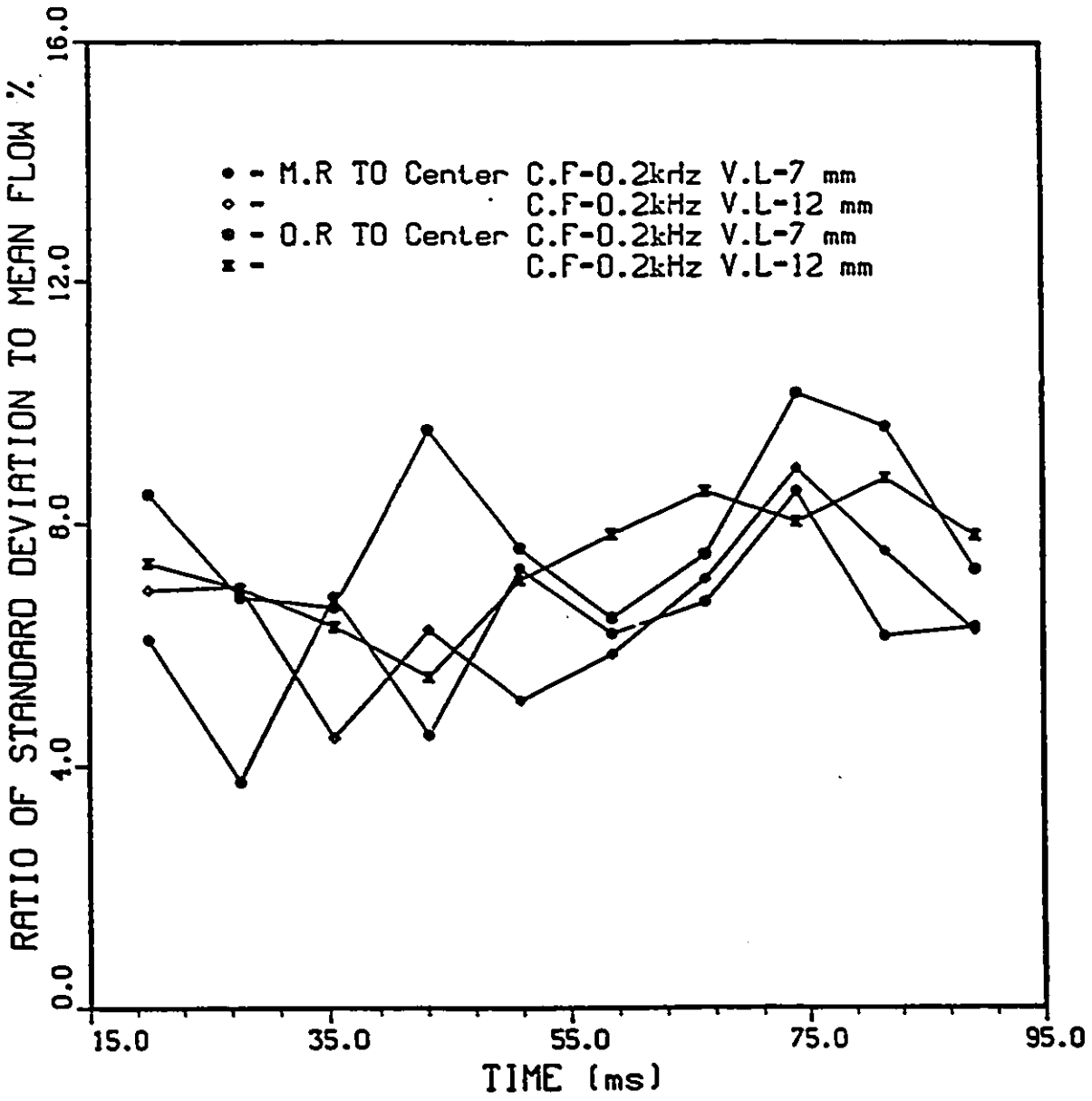

Figure 5.9: Ratio of standard deviation of mean flow to mean flow as a function of time

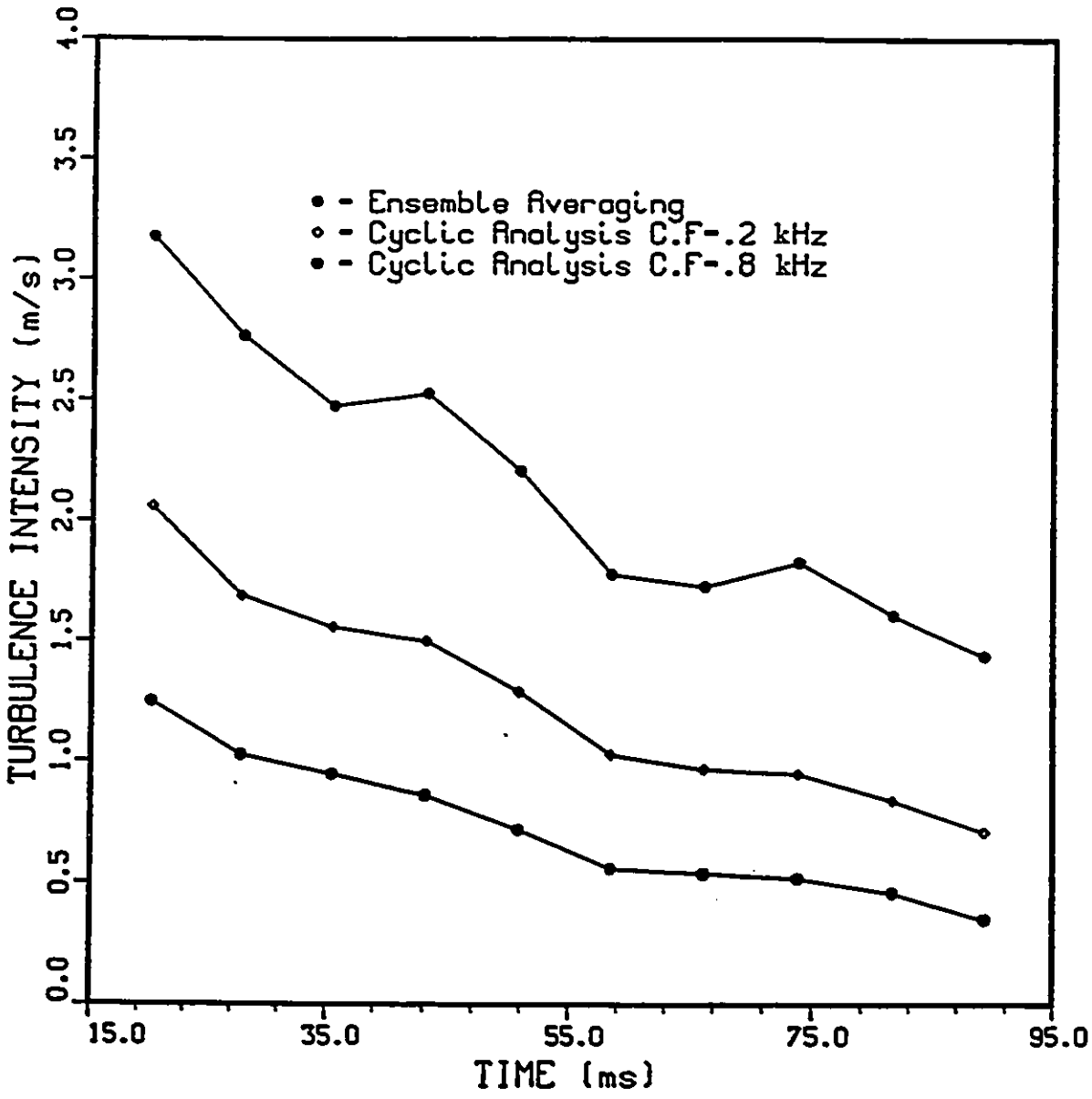

Figure 5.10: Turbulence intensity variation with time computed using ensemble averaging and cyclic analysis. (location quarter radius from center and valve lift=7mm)

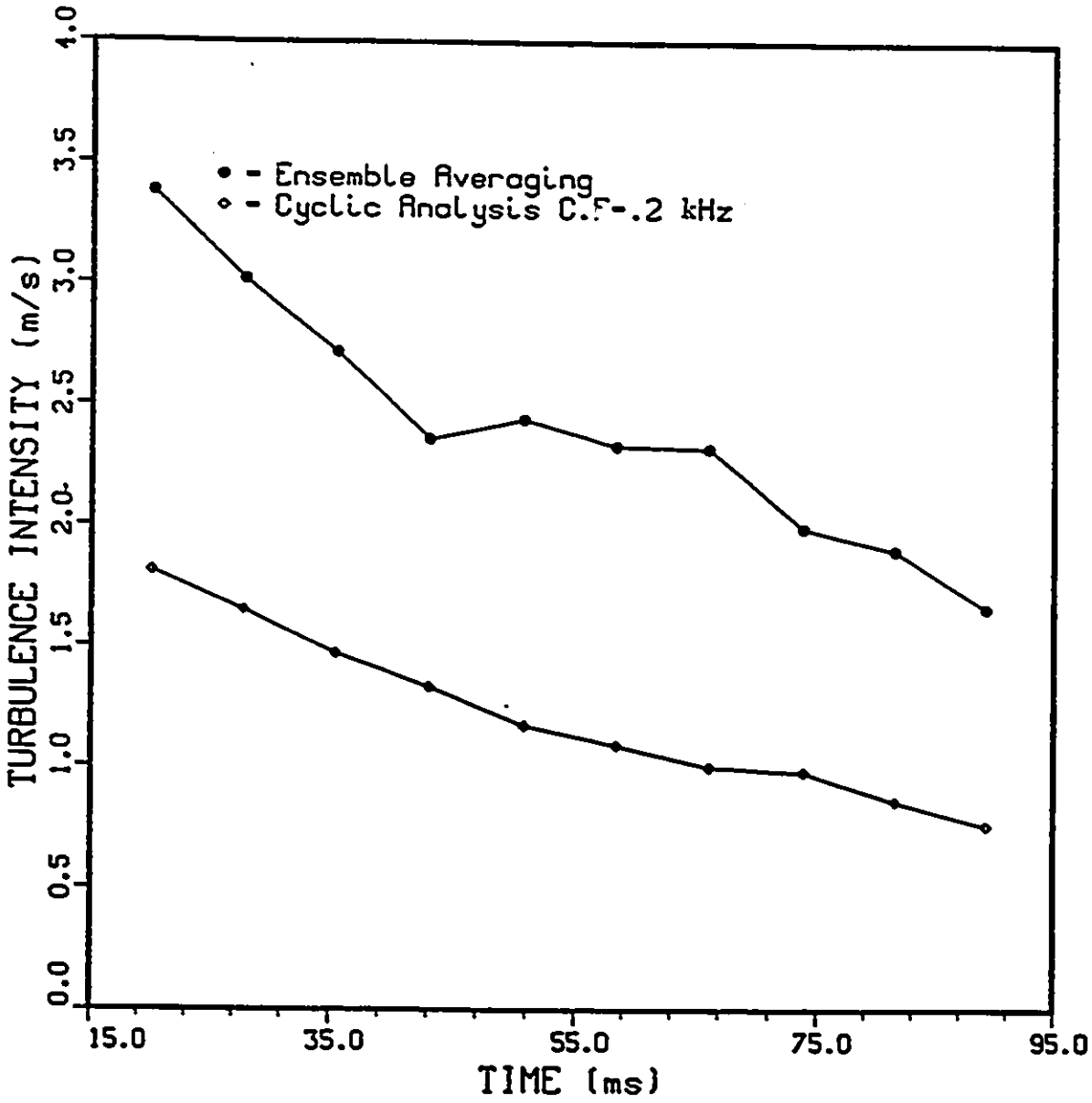

Figure 5.11: Turbulence intensity variation with time computed using ensemble averaging and cyclic analysis. (location quarter radius from center and valve lift=12mm)

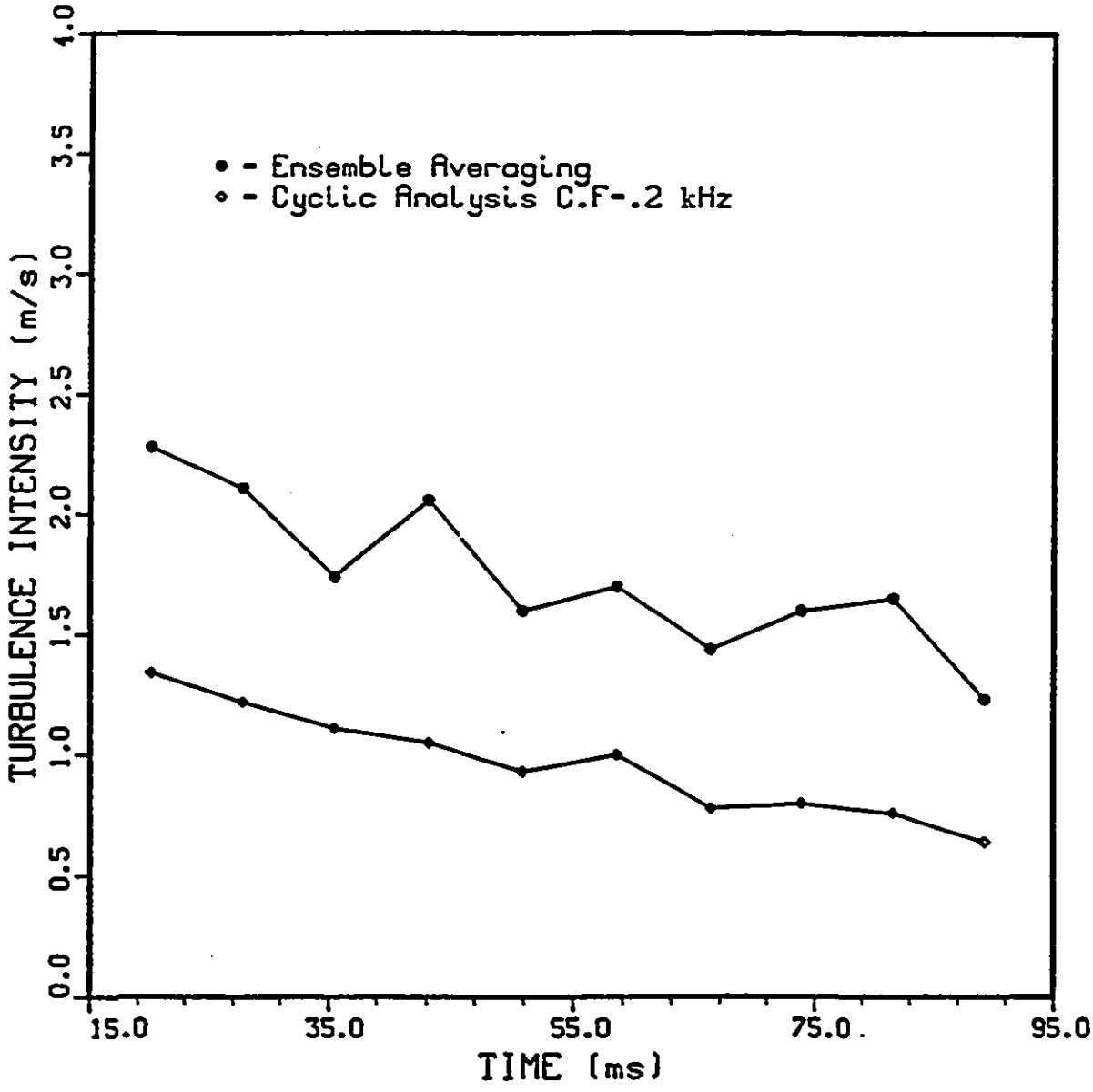

Figure 5.12: Turbulence intensity variation with time computed using ensemble averaging and cyclic analysis. (location mid-radius and valve lift=7mm)

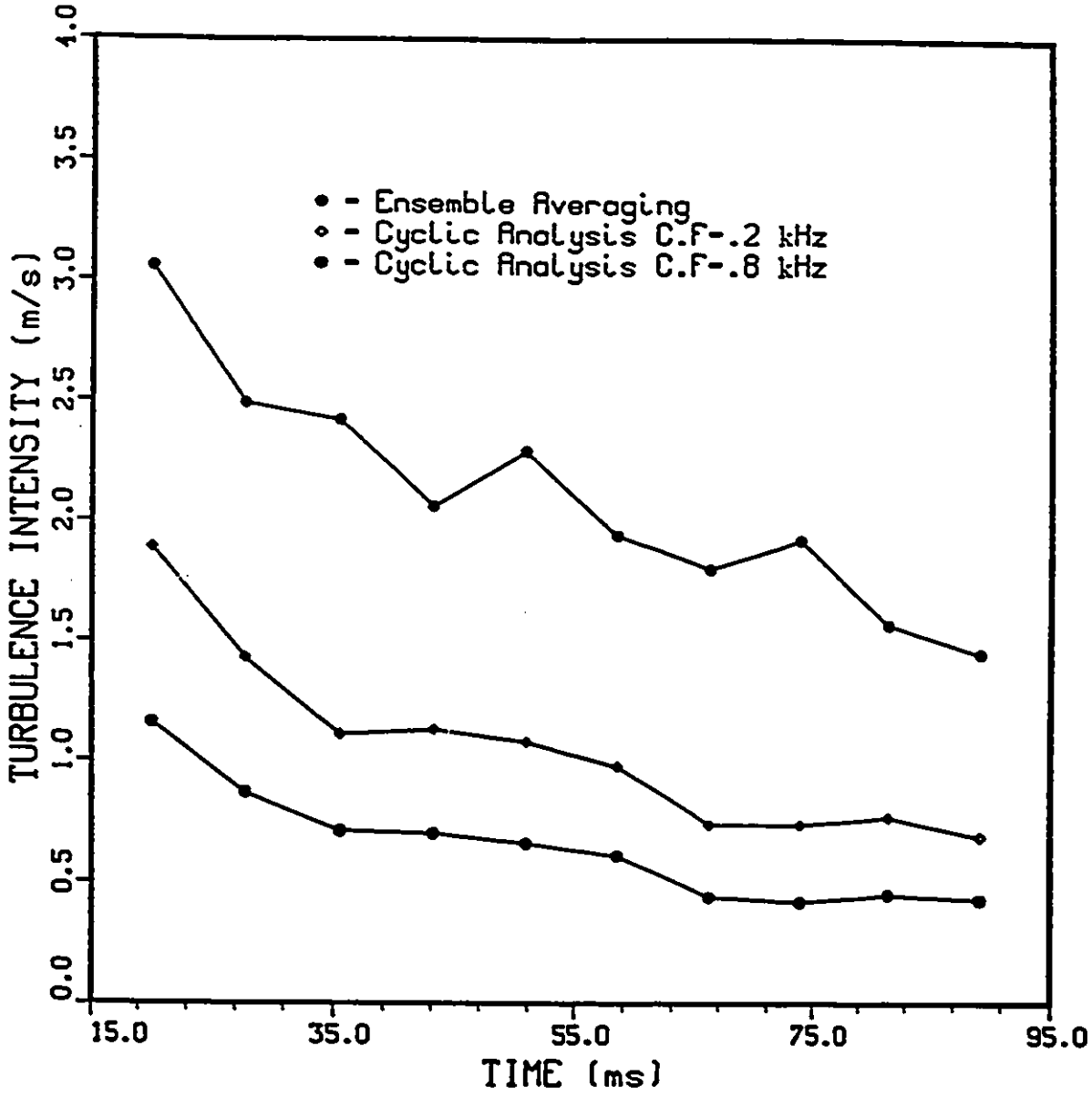

Figure 5.13: Turbulence intensity variation with time computed using ensemble averaging and cyclic analysis. (location mid-radius and valve lift=12mm)

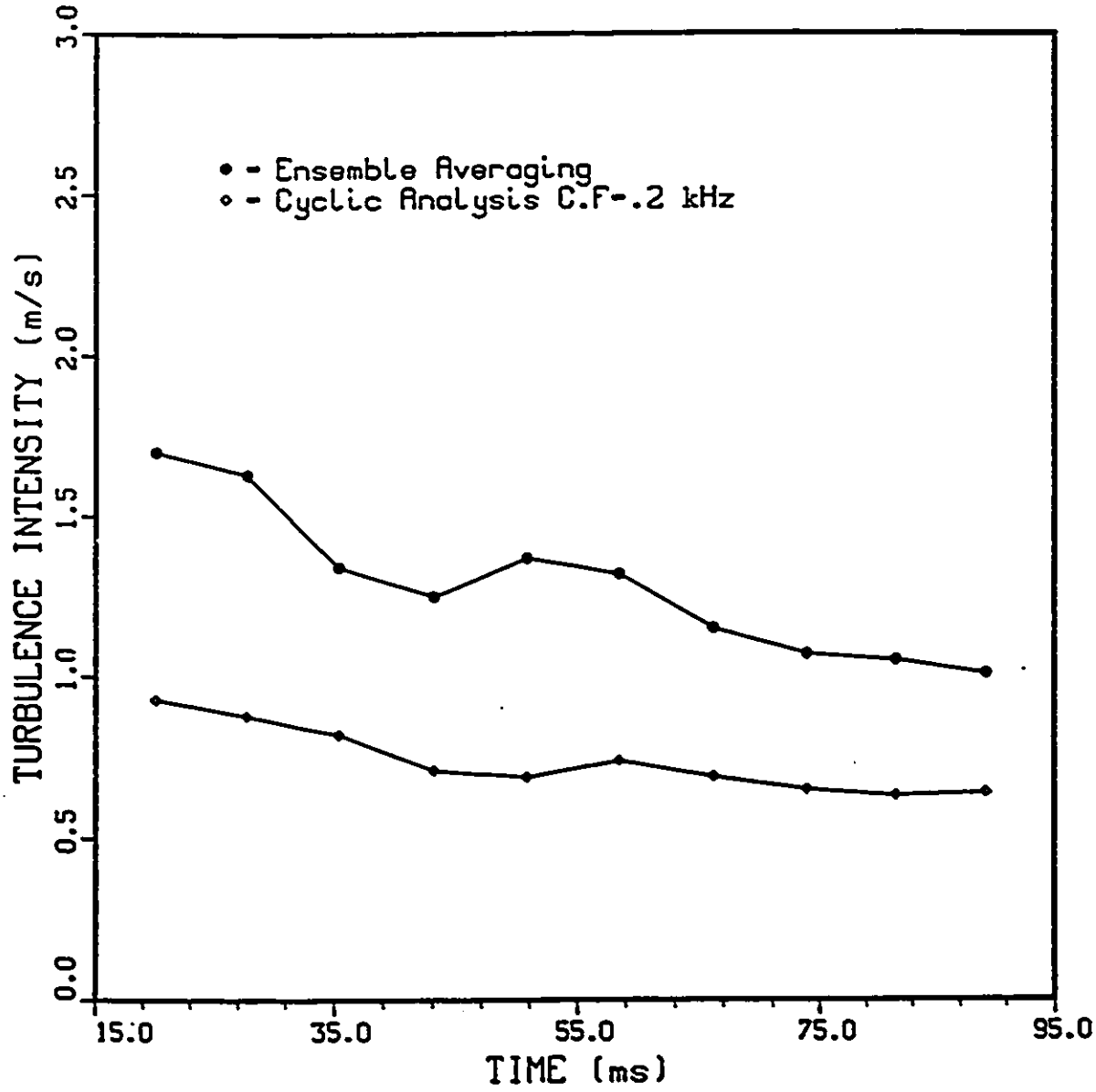

Figure 5.14: Turbulence intensity variation with time computed using ensemble averaging and cyclic analysis. (location quarter radius to wall and valve lift=7mm)

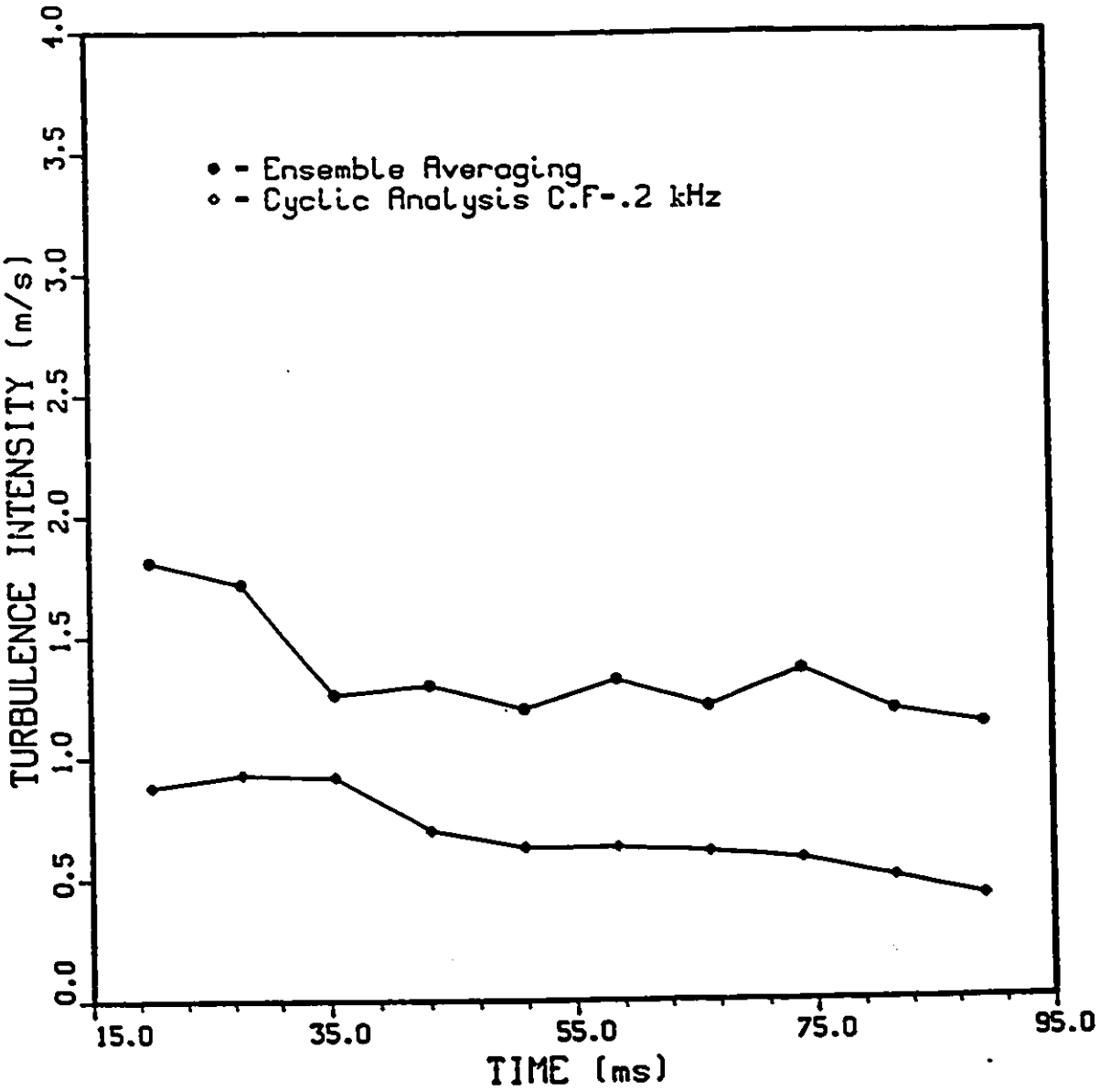

Figure 5.15: Turbulence intensity variation with time computed using ensemble averaging and cyclic analysis. (location quarter radius to wall and valve lift=12mm)

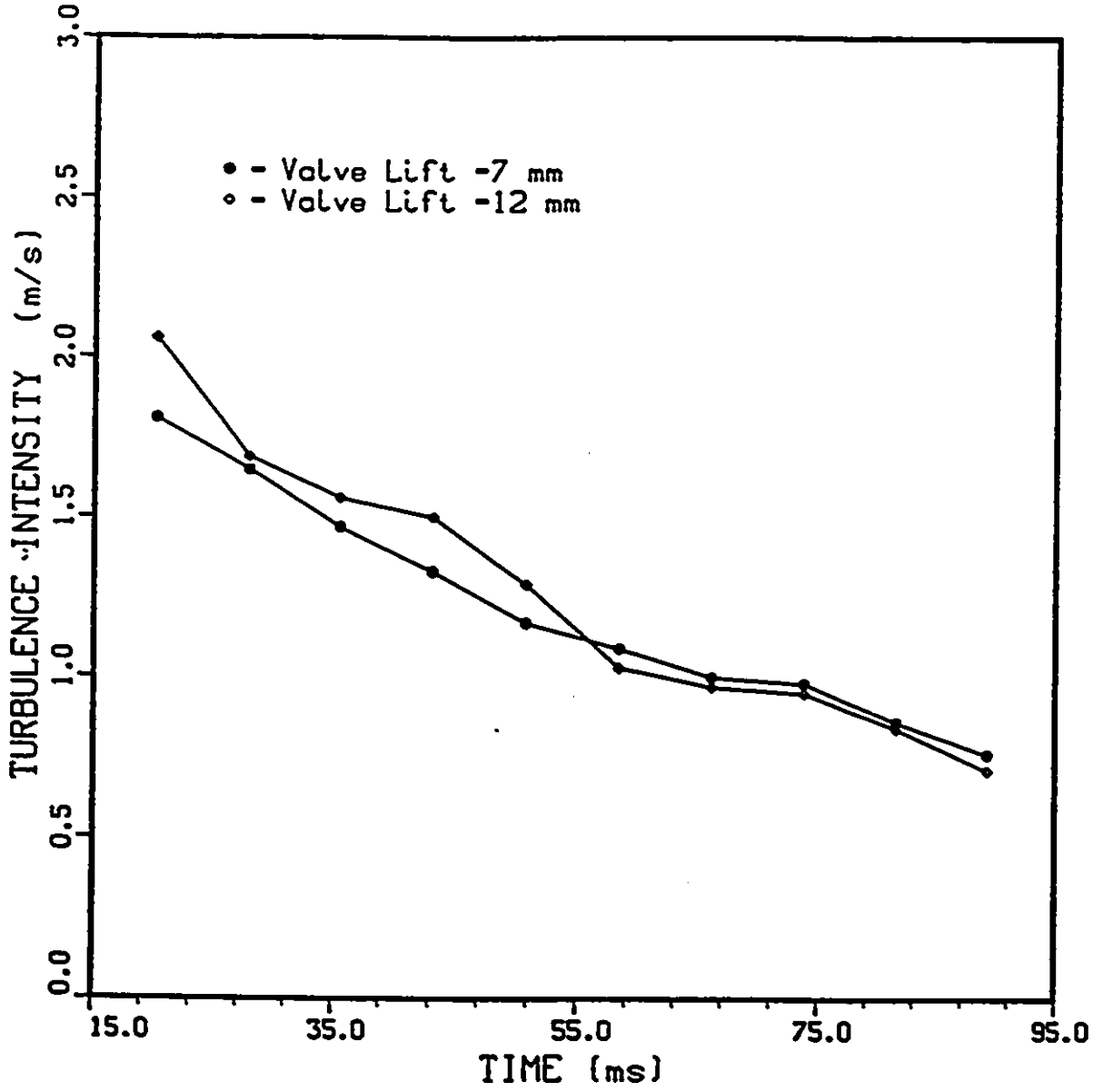

Figure 5.16: Effect of valve lift on turbulence intensity (location: quarter radius from center)

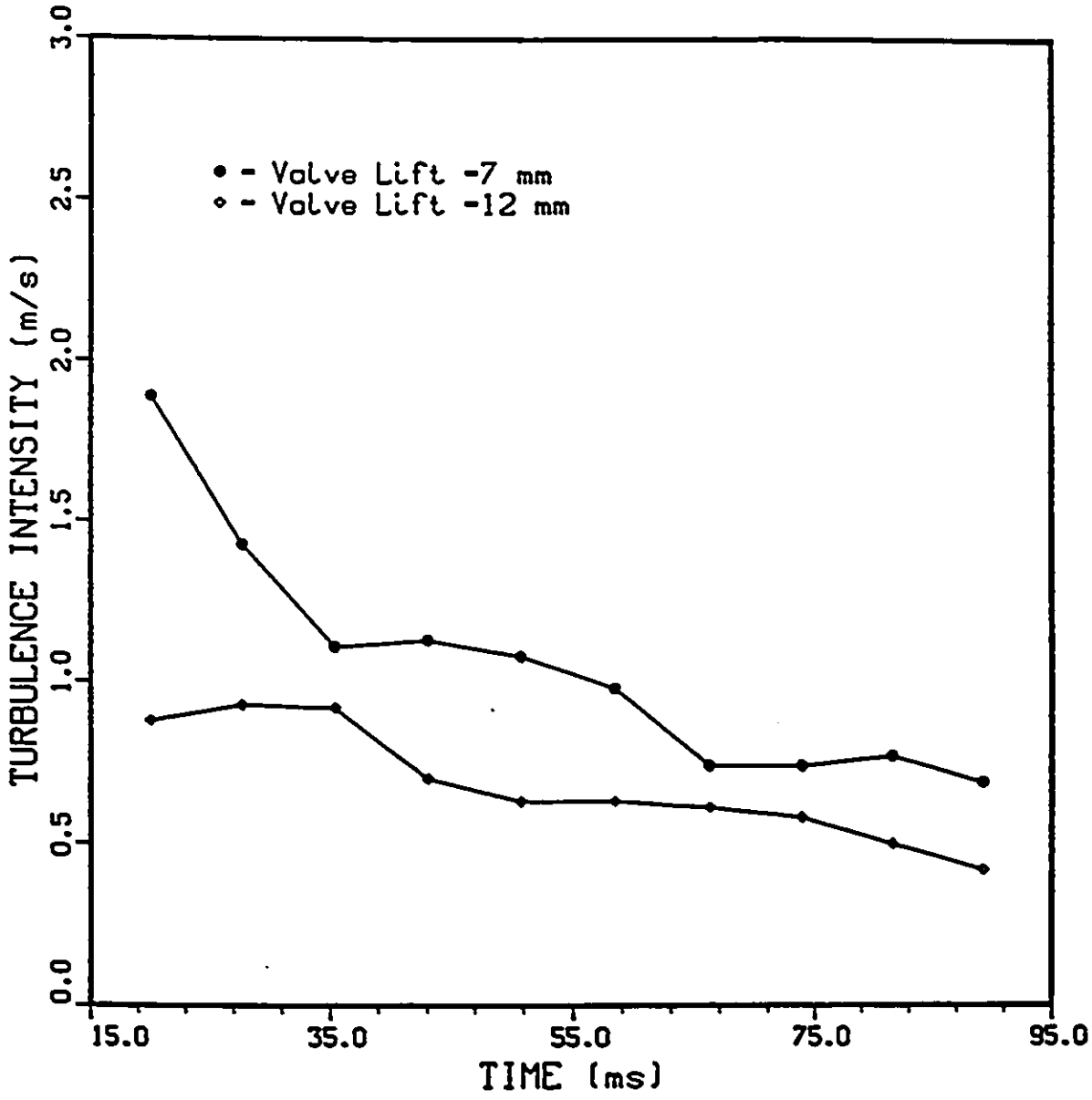

Figure 5.17: Effect of valve lift on turbulence intensity (location: mid-radius)

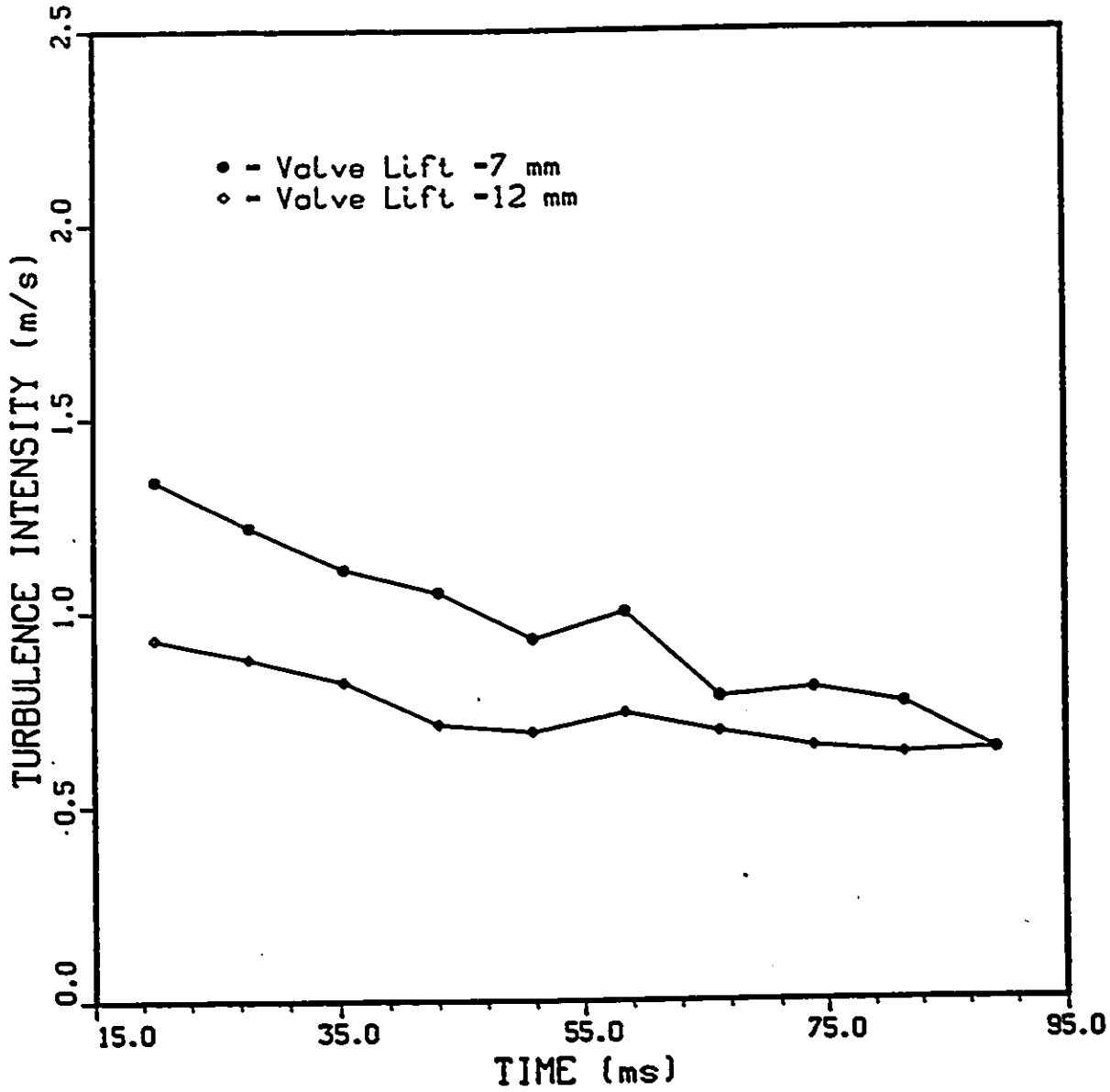

Figure 5.18: Effect of valve lift on turbulence intensity (location: quarter radius to wall)

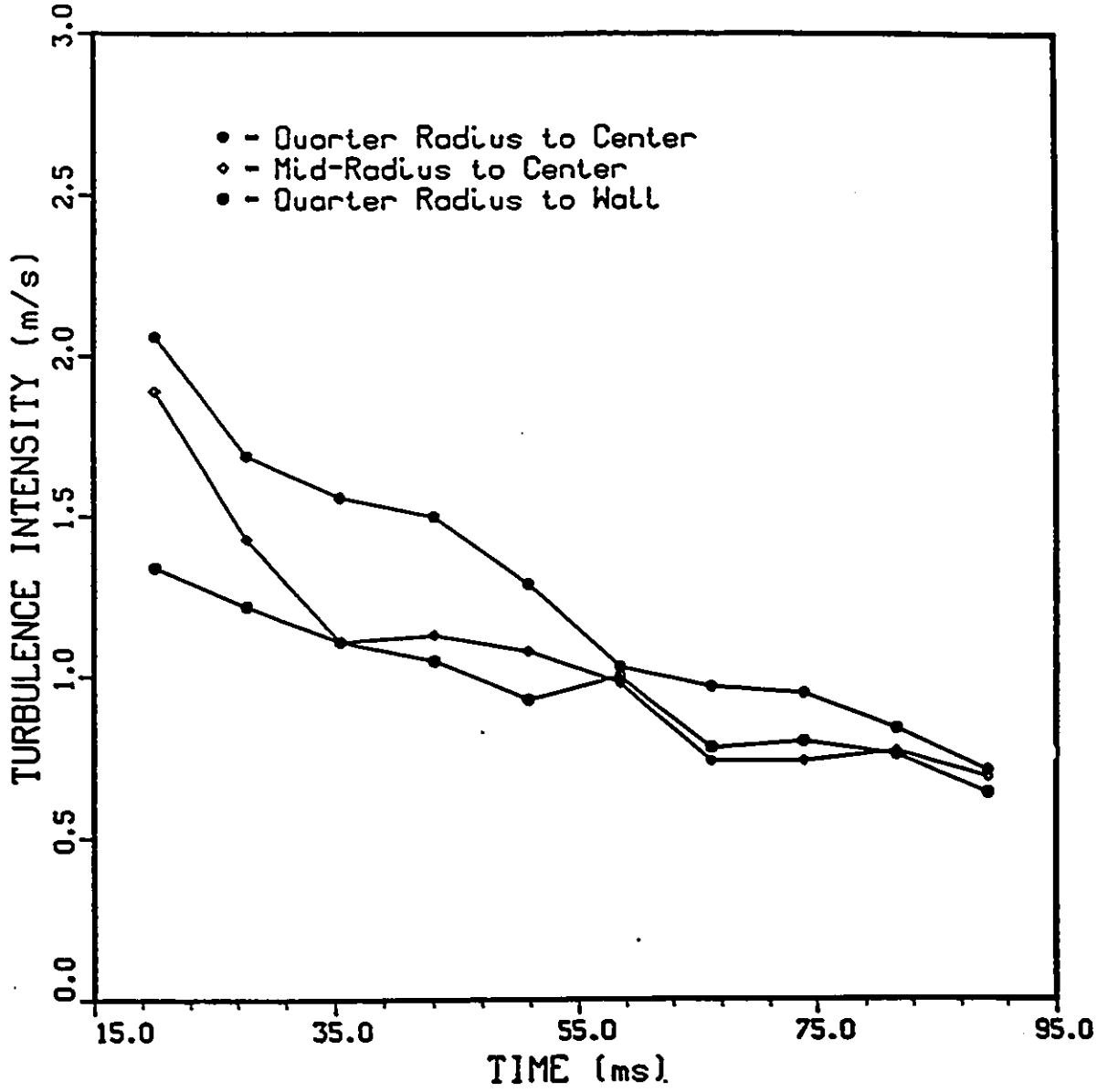

Figure 5.19: Effect of location on turbulence intensity (valve lift=7mm)

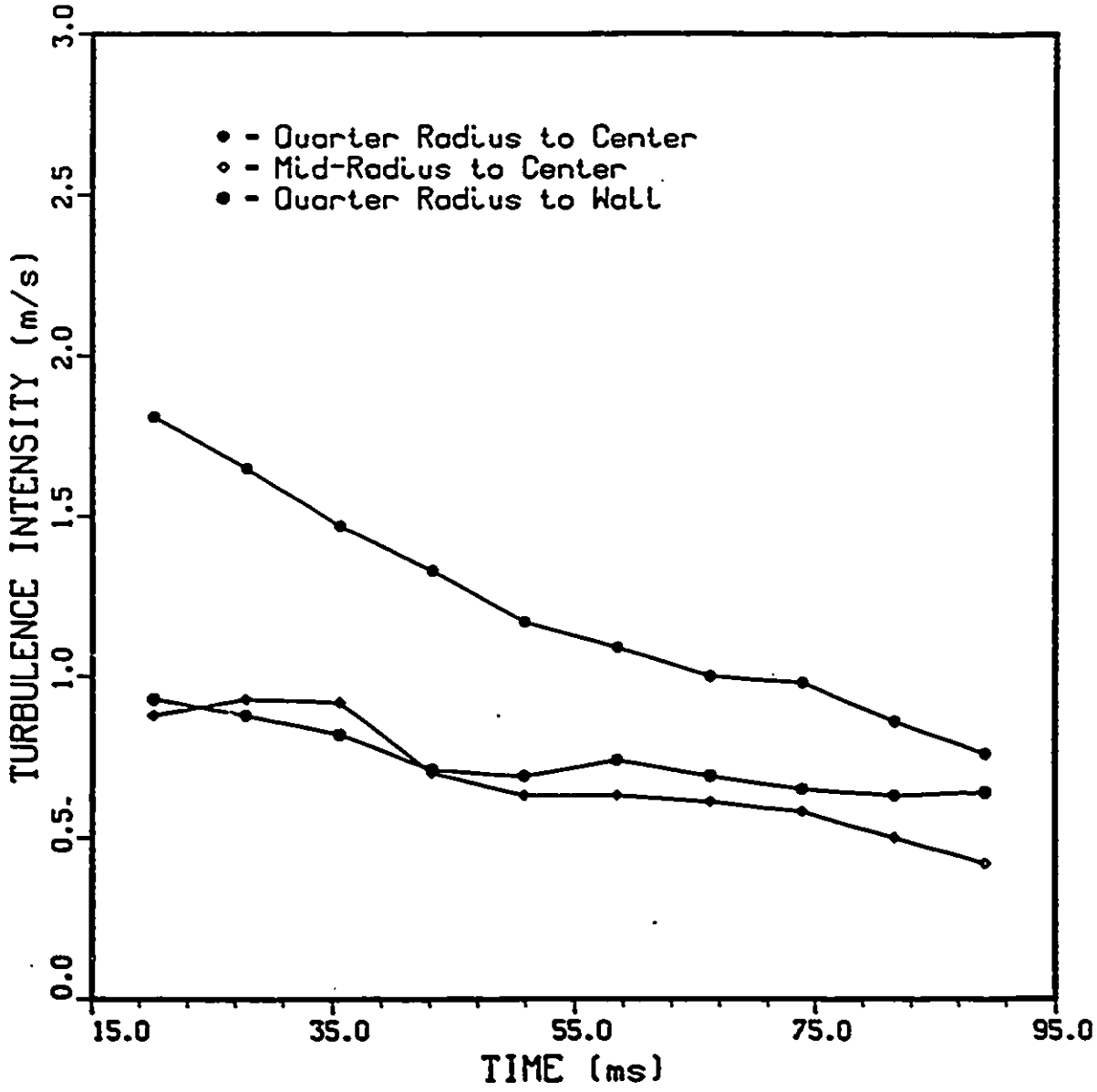

Figure 5.20: Effect of location on turbulence intensity (valve lift=12mm)

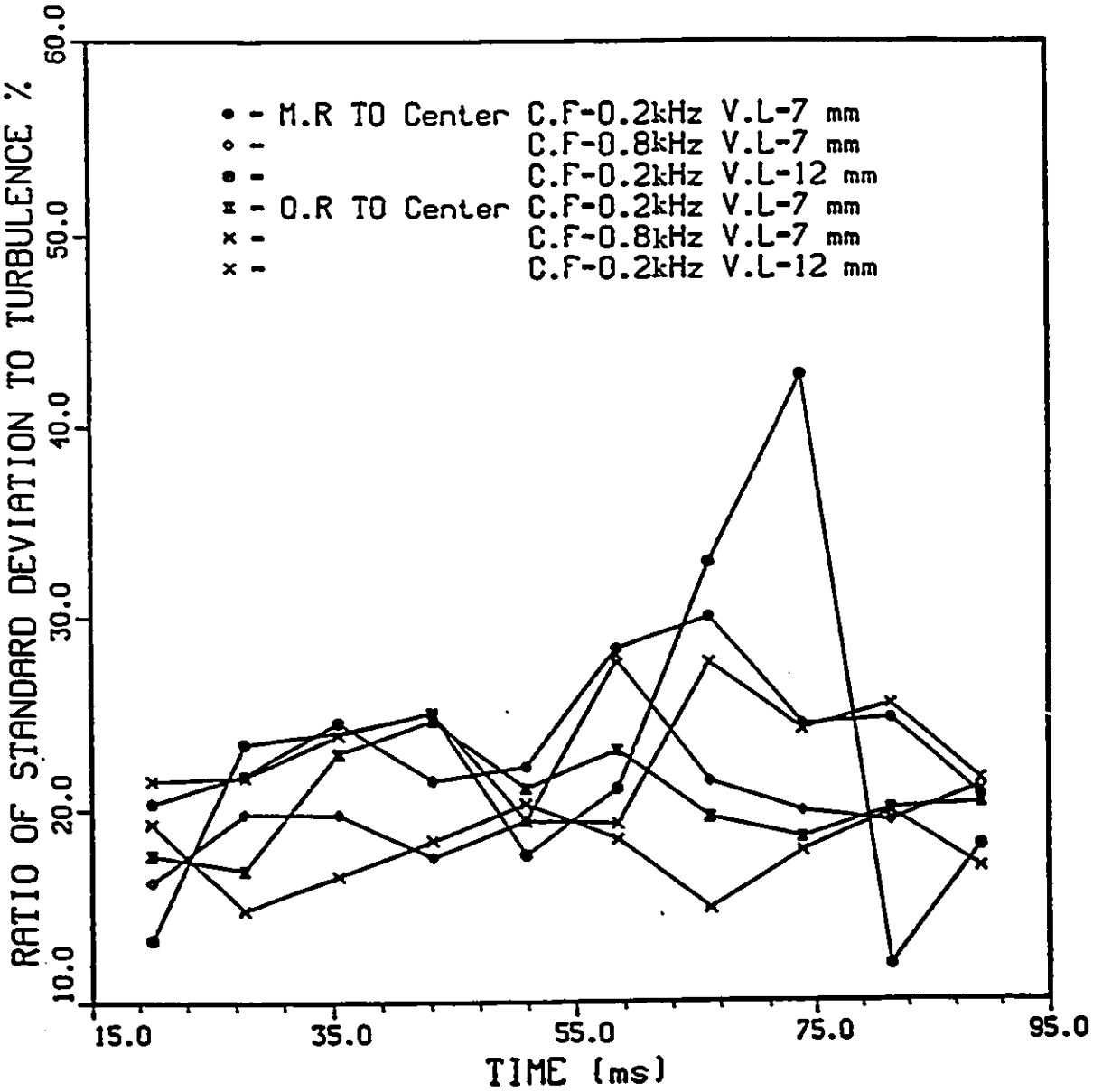

Figure 5.21: Ratio of standard deviation of turbulence intensity to turbulence intensity versus time

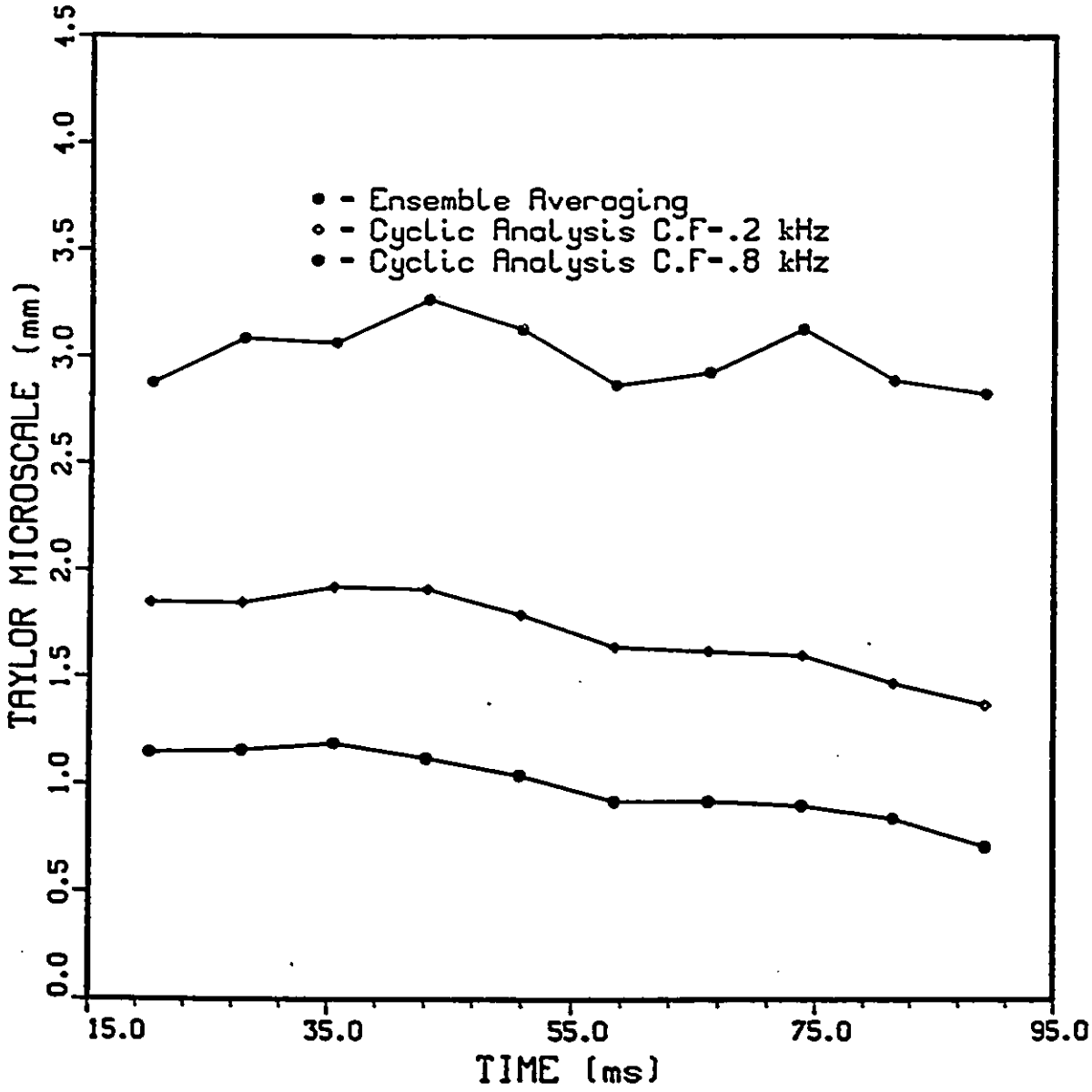

Figure 5.22: Taylor microscale variation with time computed using ensemble averaging and cyclic analysis, (location quarter radius from center and valve lift=7mm)

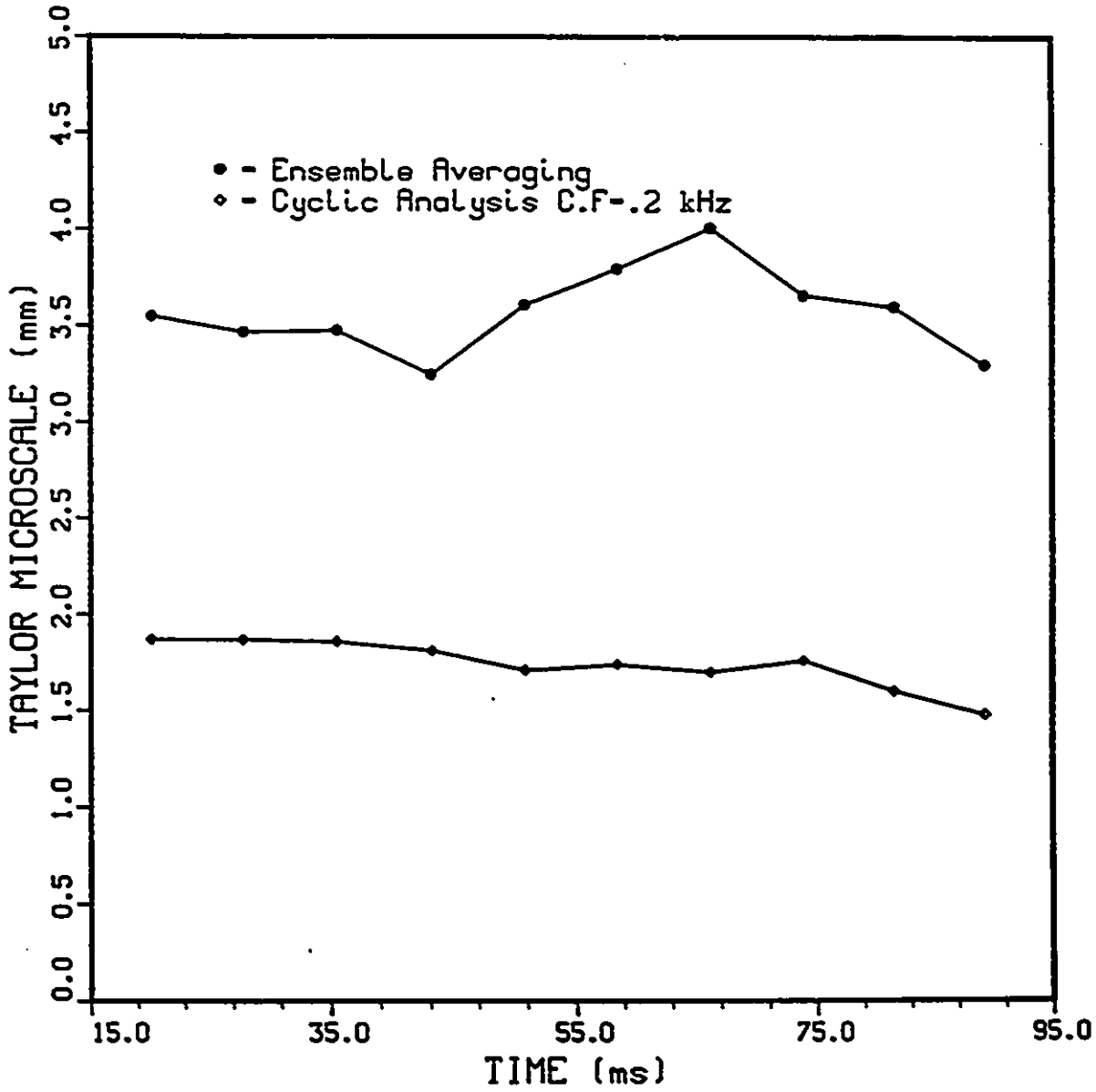

Figure 5.23: Taylor microscale variation with time computed using ensemble averaging and cyclic analysis, (location quarter radius from center and valve lift=12mm)

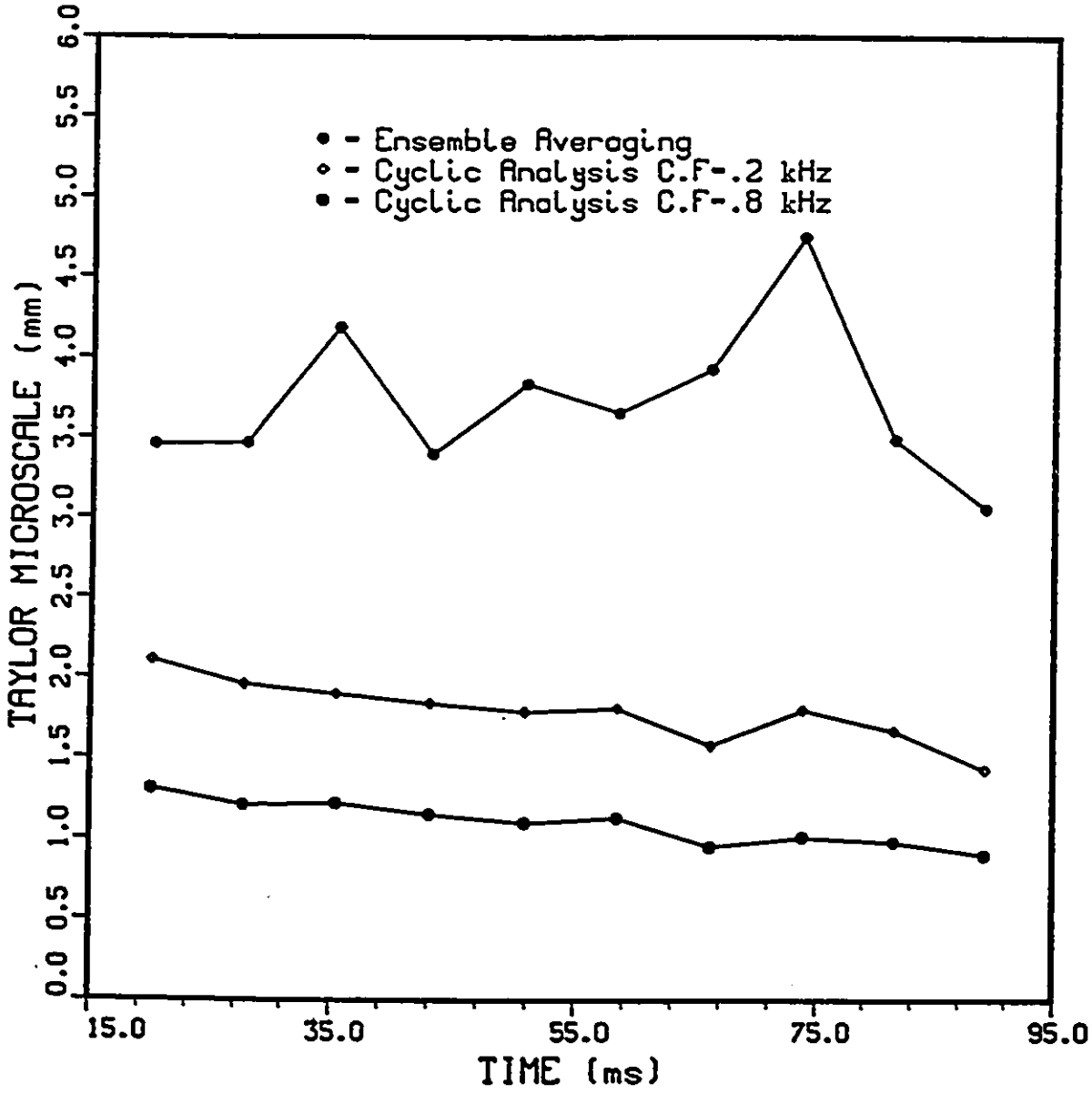

Figure 5.24: Taylor microscale variation with time computed using ensemble averaging and cyclic analysis, (location mid-radius and valve lift=7mm)

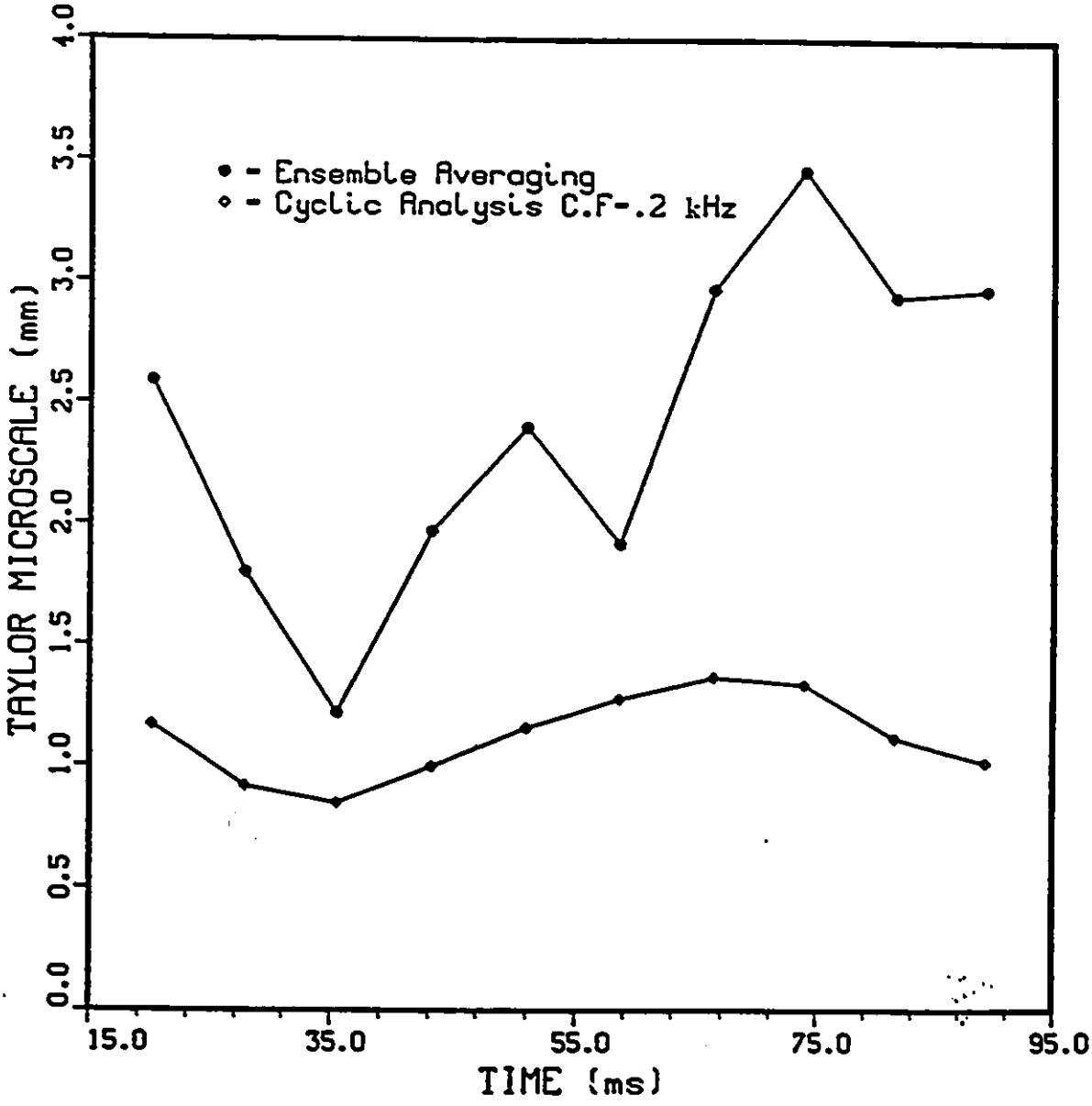

Figure 5.25: Taylor microscale variation with time computed using ensemble averaging and cyclic analysis, (location mid-radius and valve lift=12mm)

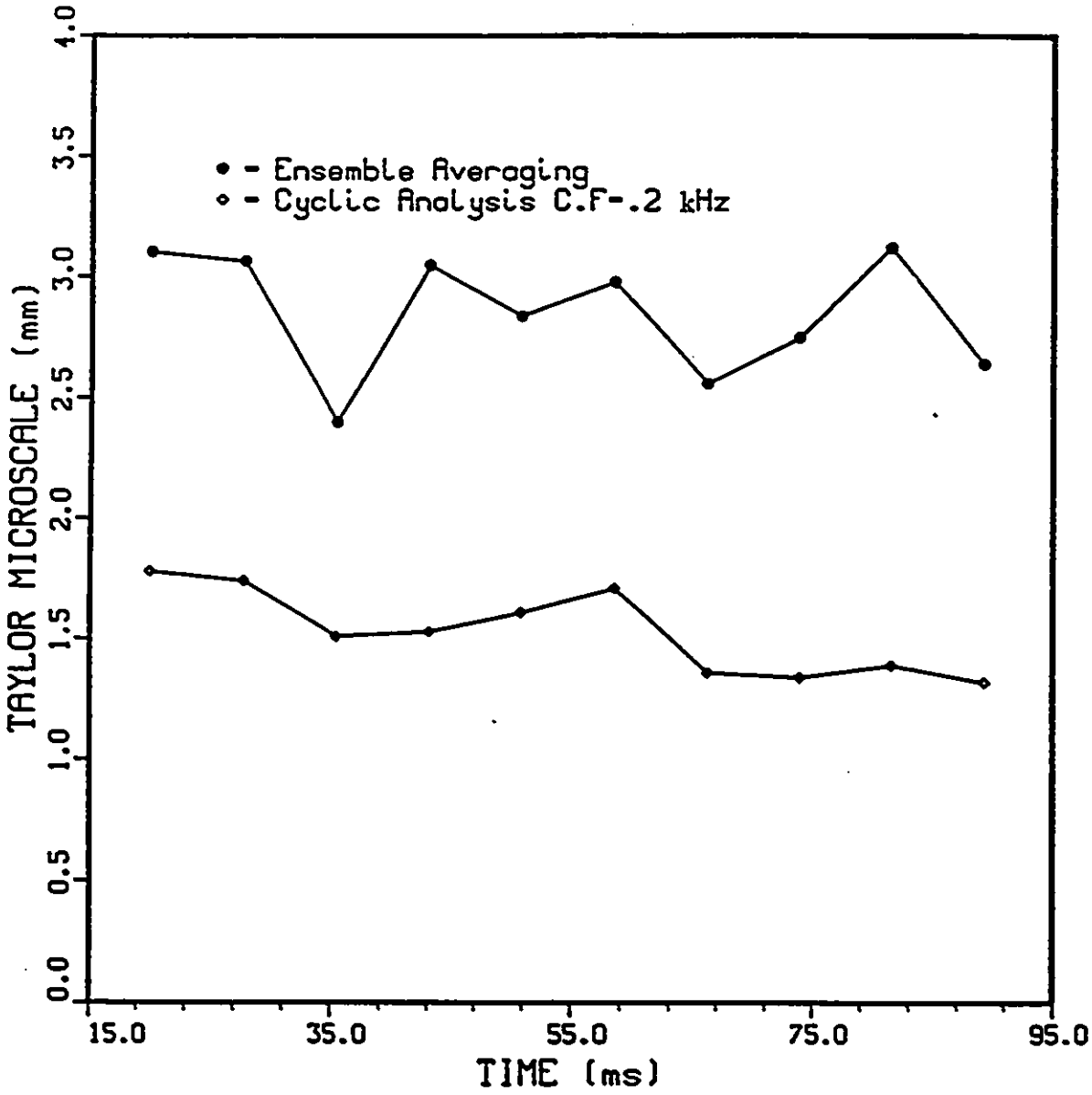

Figure 5.26: Taylor microscale variation with time computed using ensemble averaging and cyclic analysis, (location quarter radius to wall and valve lift=7mm)

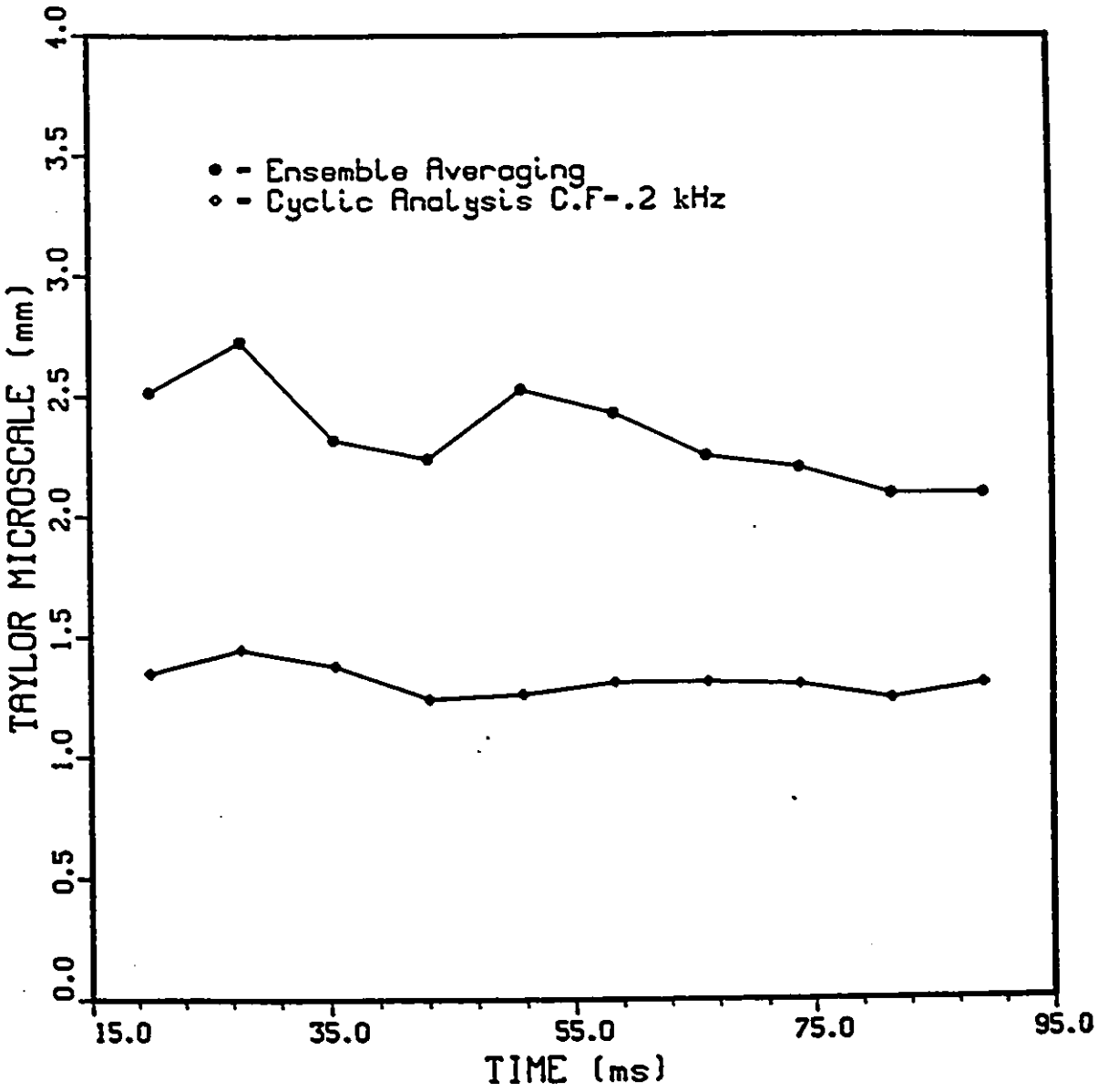

Figure 5.27: Taylor microscale variation with time computed using ensemble averaging and cyclic analysis, (location quarter radius to wall and valve lift=12mm)

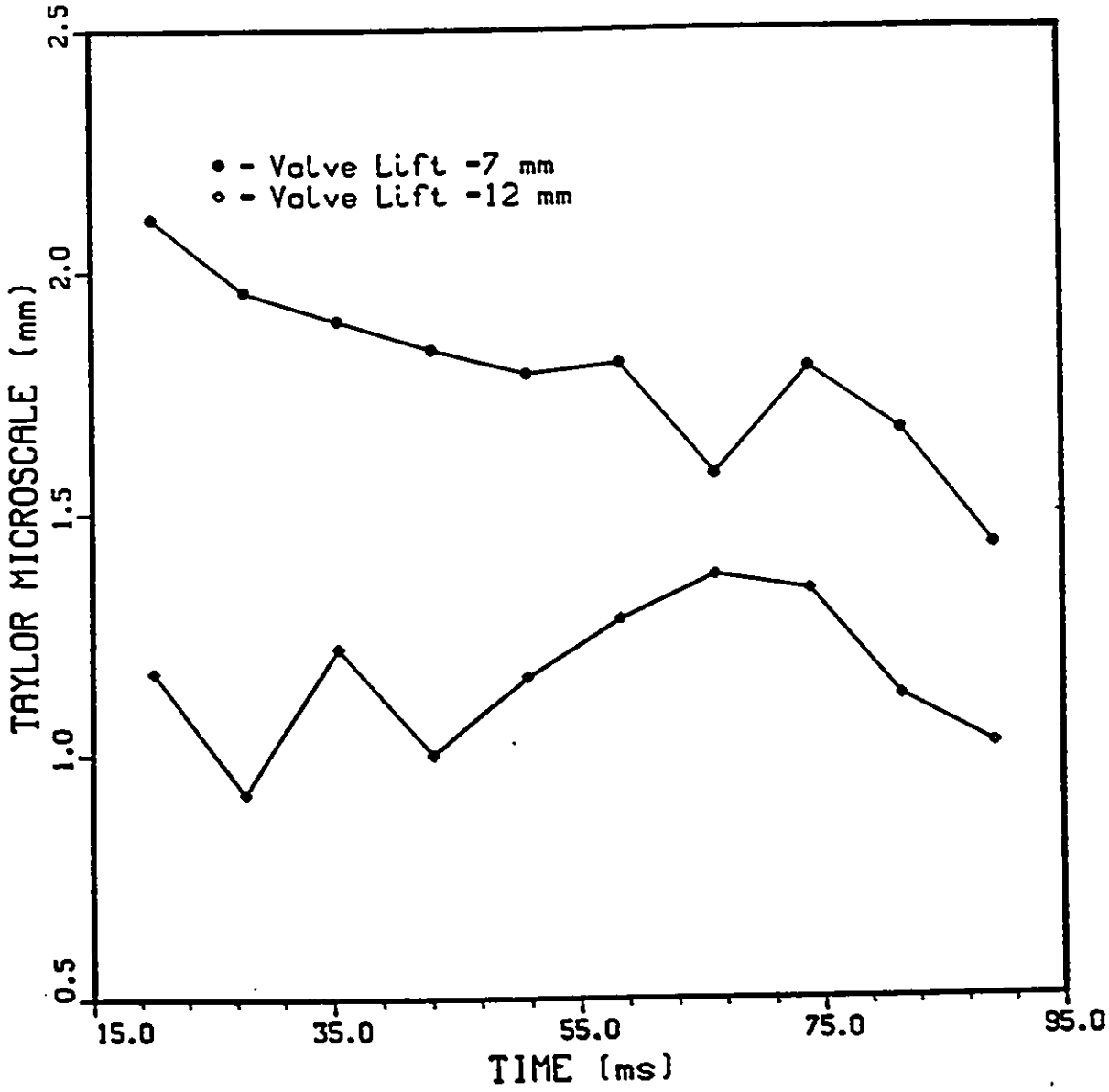

Figure 5.28: Effect of valve lift on Taylor microscale, (location: quarter radius from center)

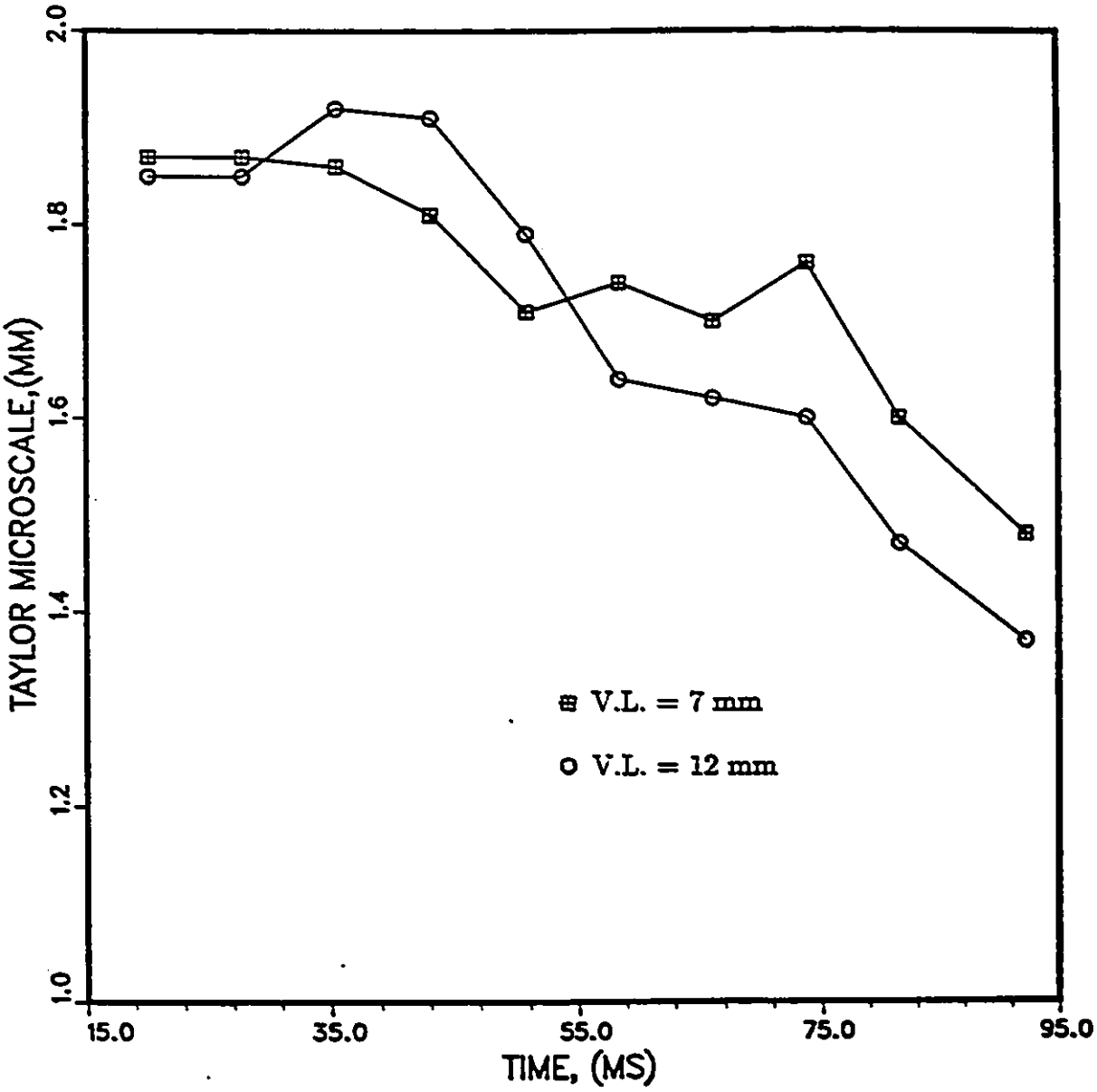

Figure 5.29: Effect of valve lift on Taylor microscale, (location: mid-radius)

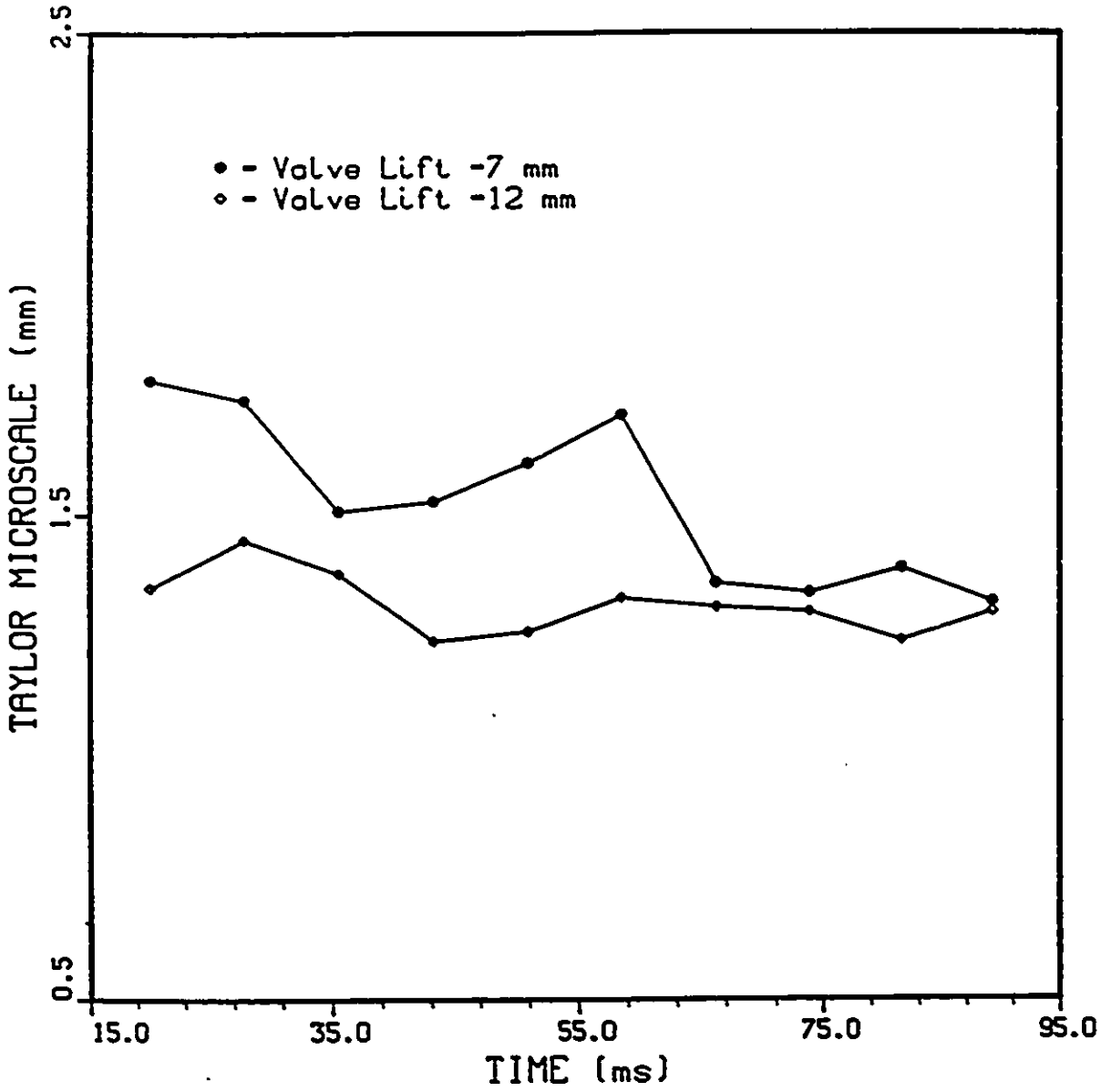

Figure 5.30: Effect of valve lift on Taylor microscale, (location: quarter radius to wall)

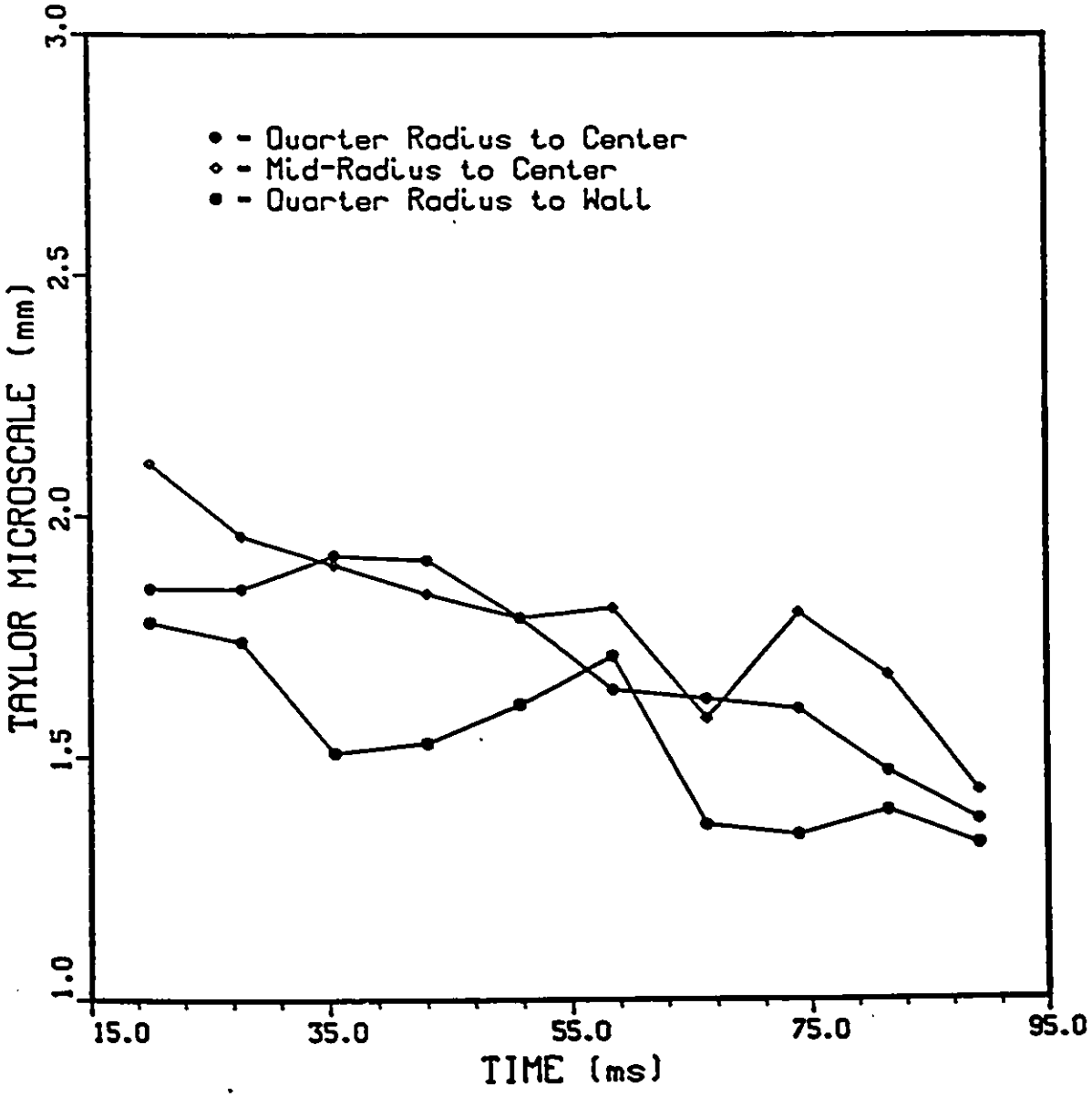

Figure 5.31: Effect of location on Taylor microscale, (valve lift=7mm)

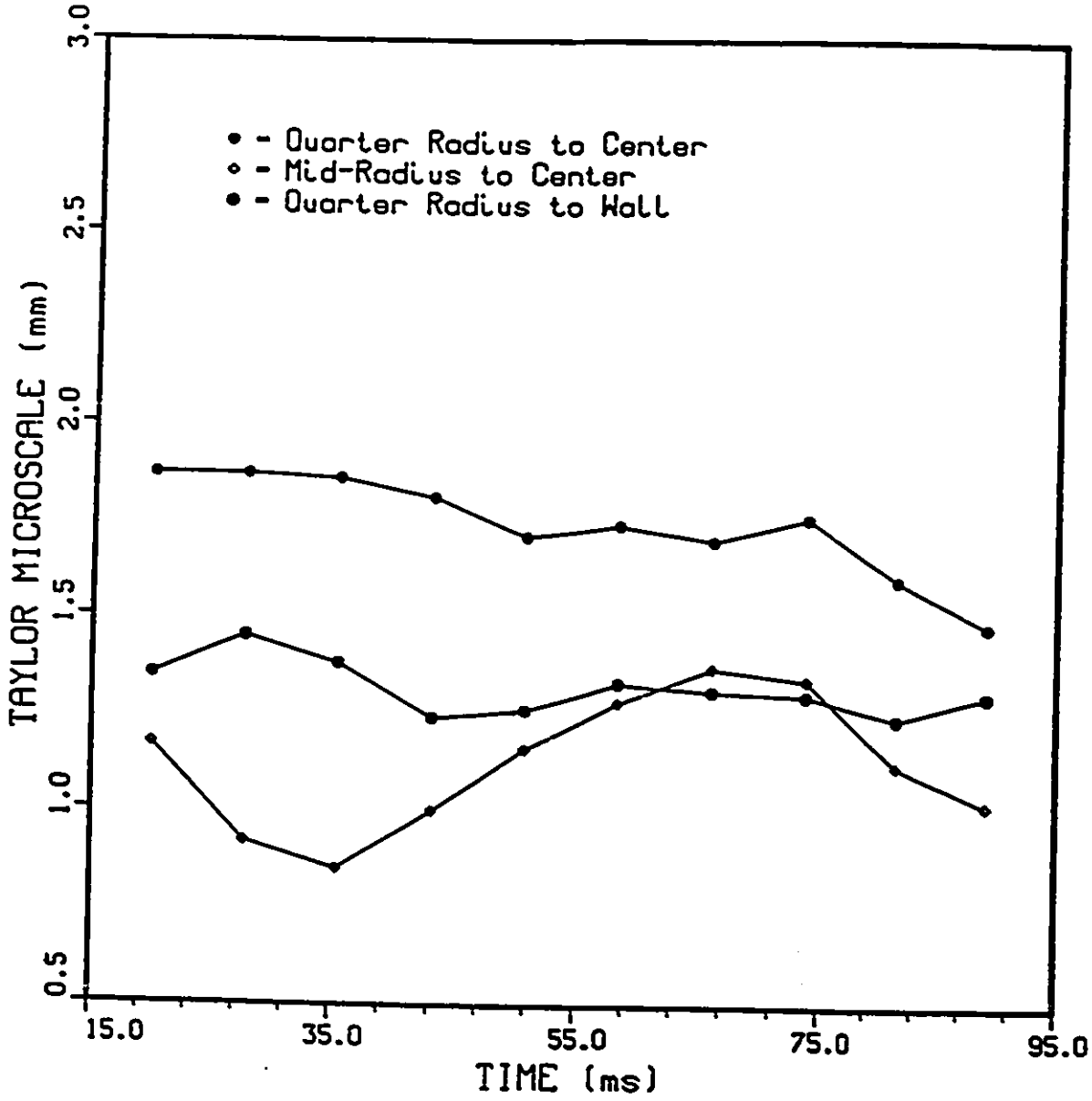

Figure 5.32: Effect of location on Taylor microscale, (valve lift=12mm)

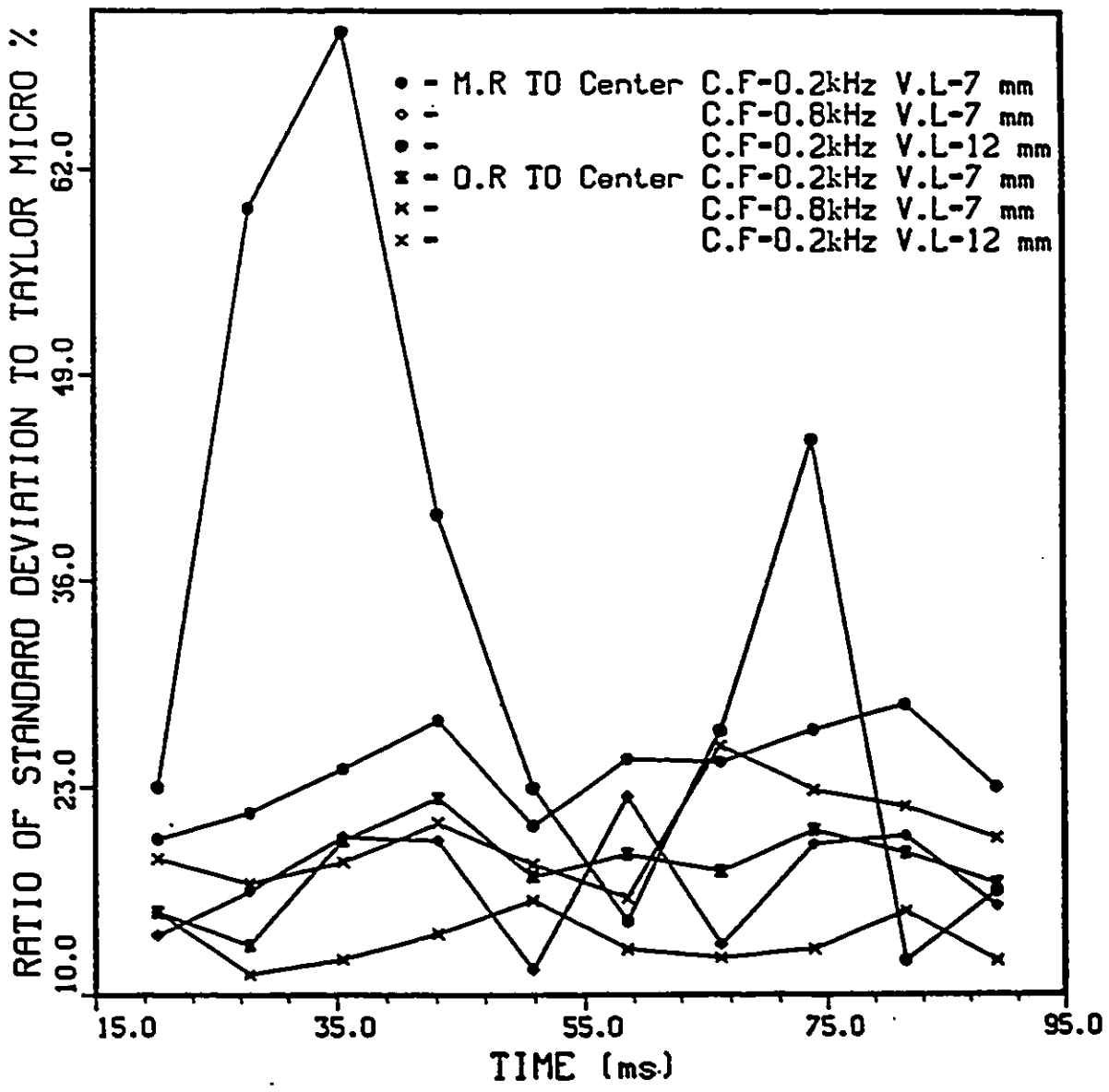

Figure 5.33: Ratio of standard deviation of Taylor microscale to Taylor microscale

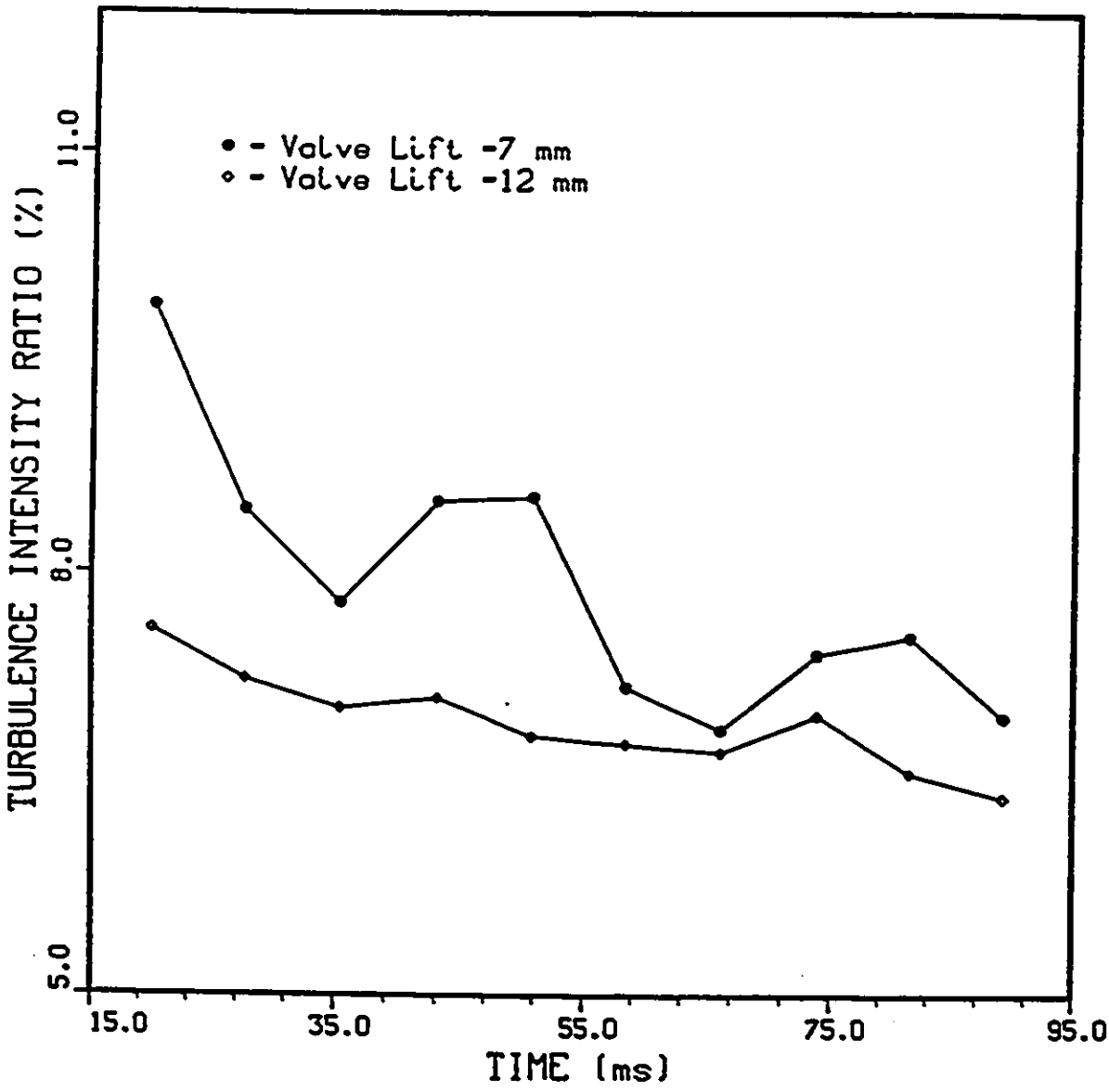

Figure 5.34: Turbulence intensity to mean flow ratio versus time (location: quarter radius from center)

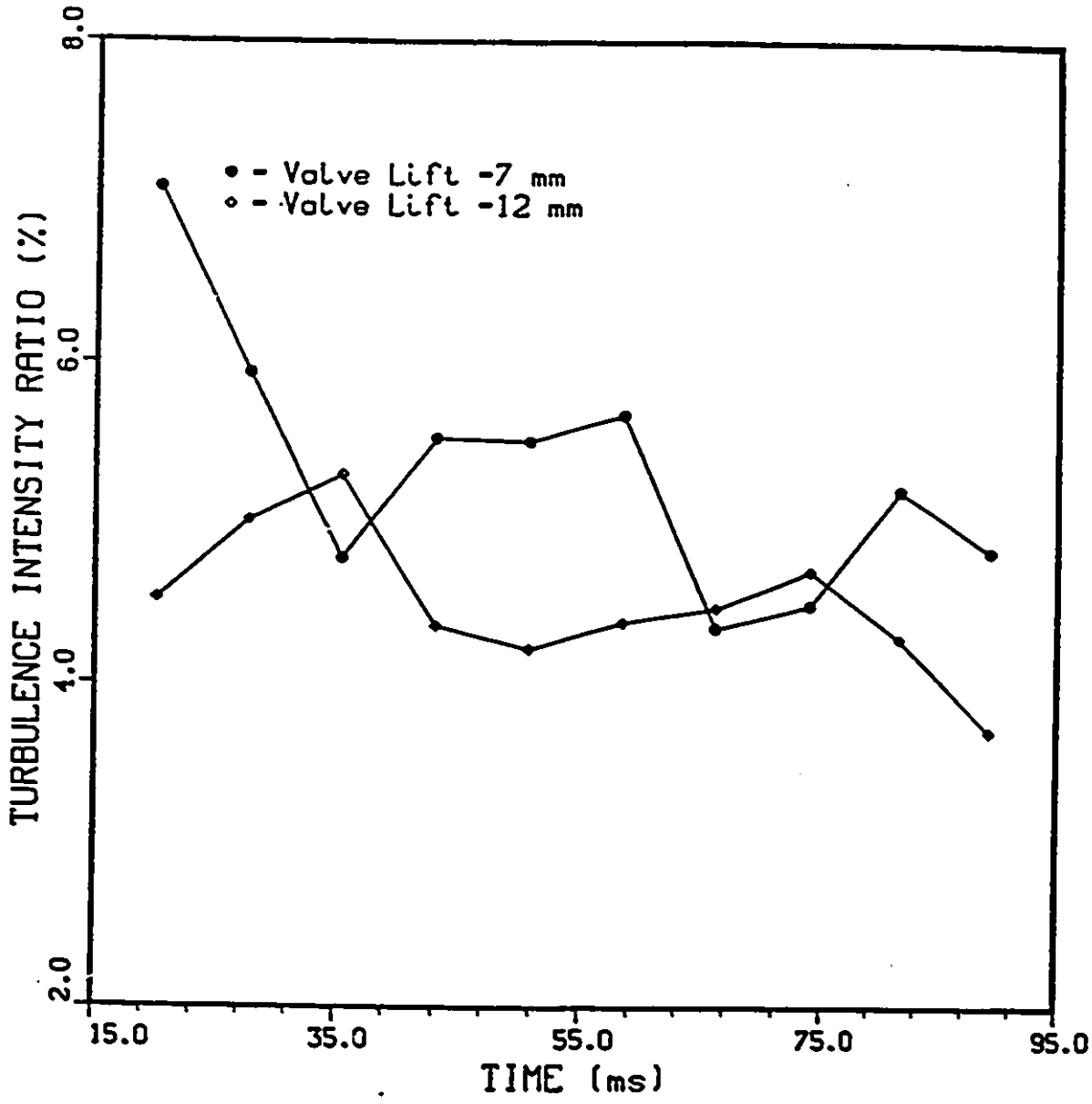

Figure 5.35: Turbulence intensity to mean flow ratio versus time (location: mid-radius)

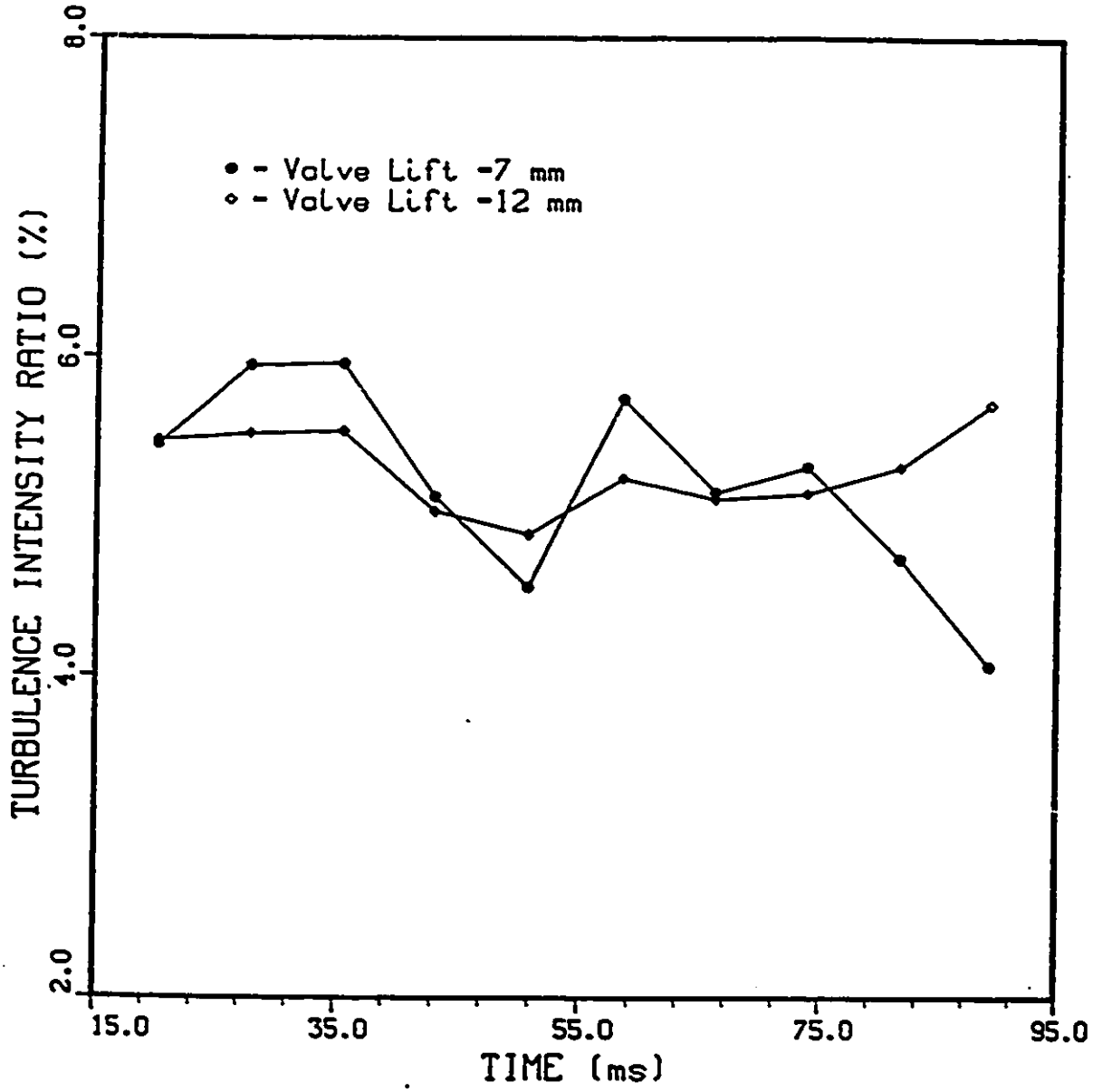

Figure 5.36: Turbulence intensity to mean flow ratio versus time (location: quarter radius to wall)

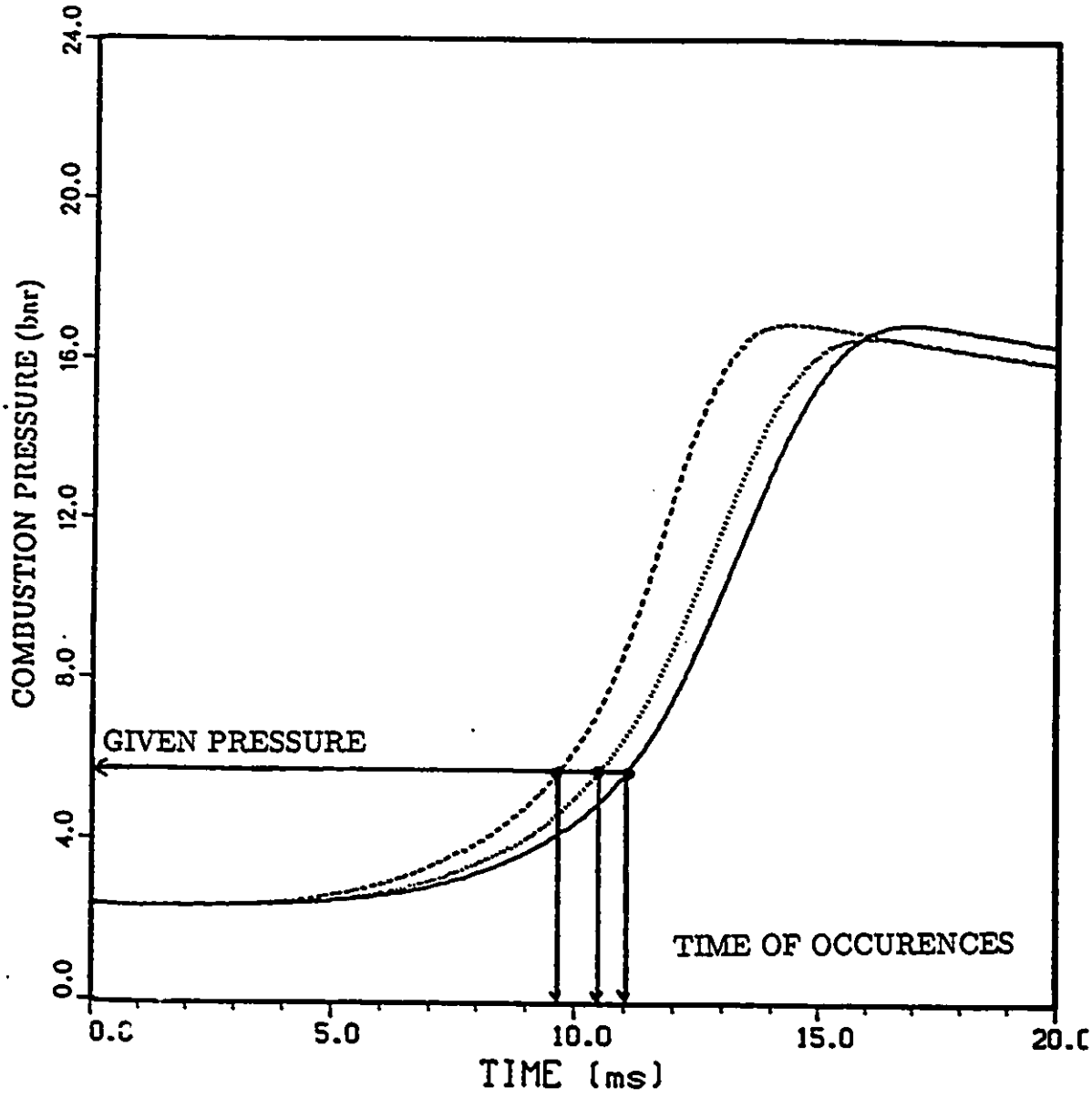

Figure 5.37: Determination of the time of occurrence of a given combustion pressure

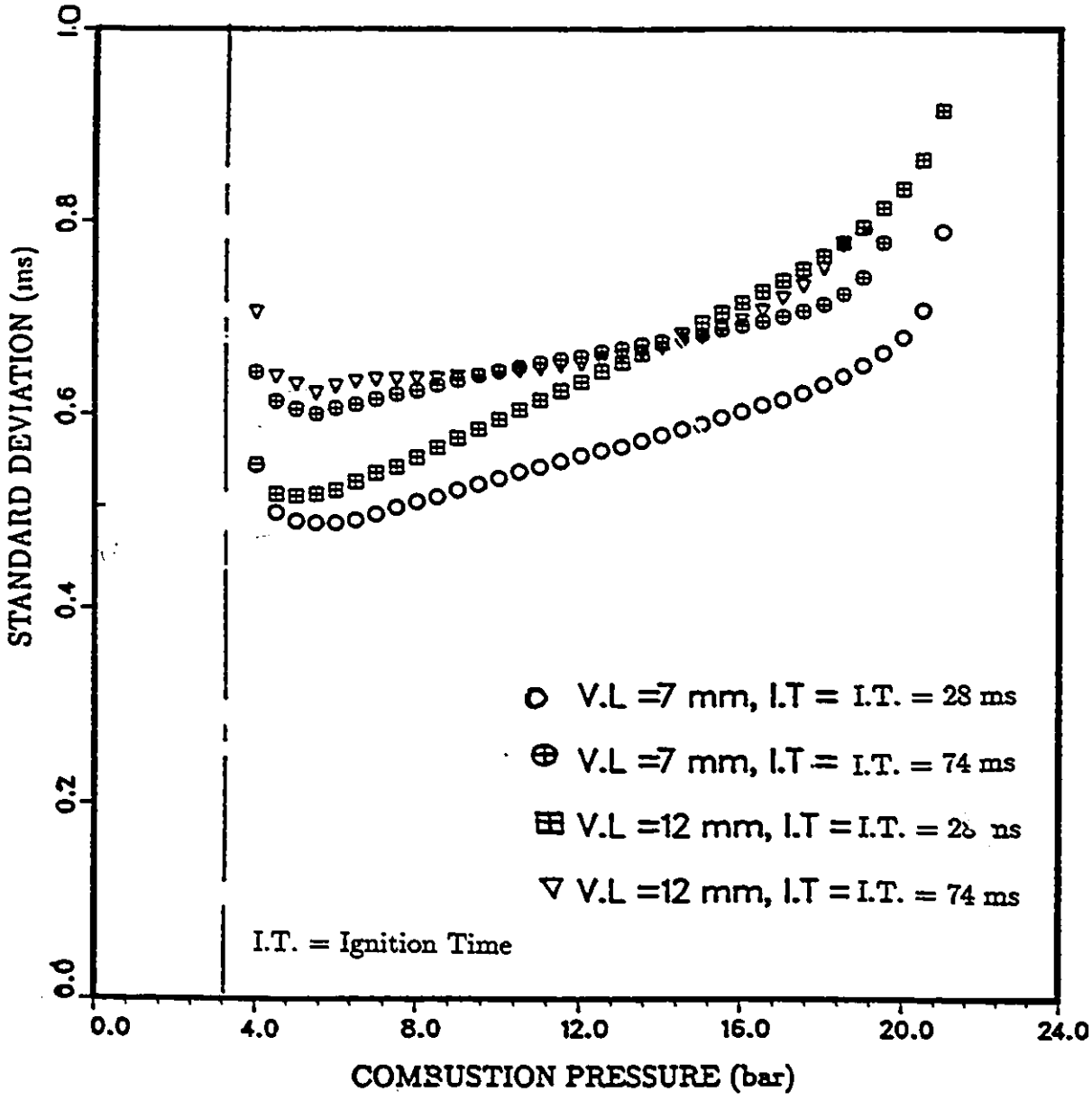

Figure 5.38: Standard deviation of delay time versus combustion pressure

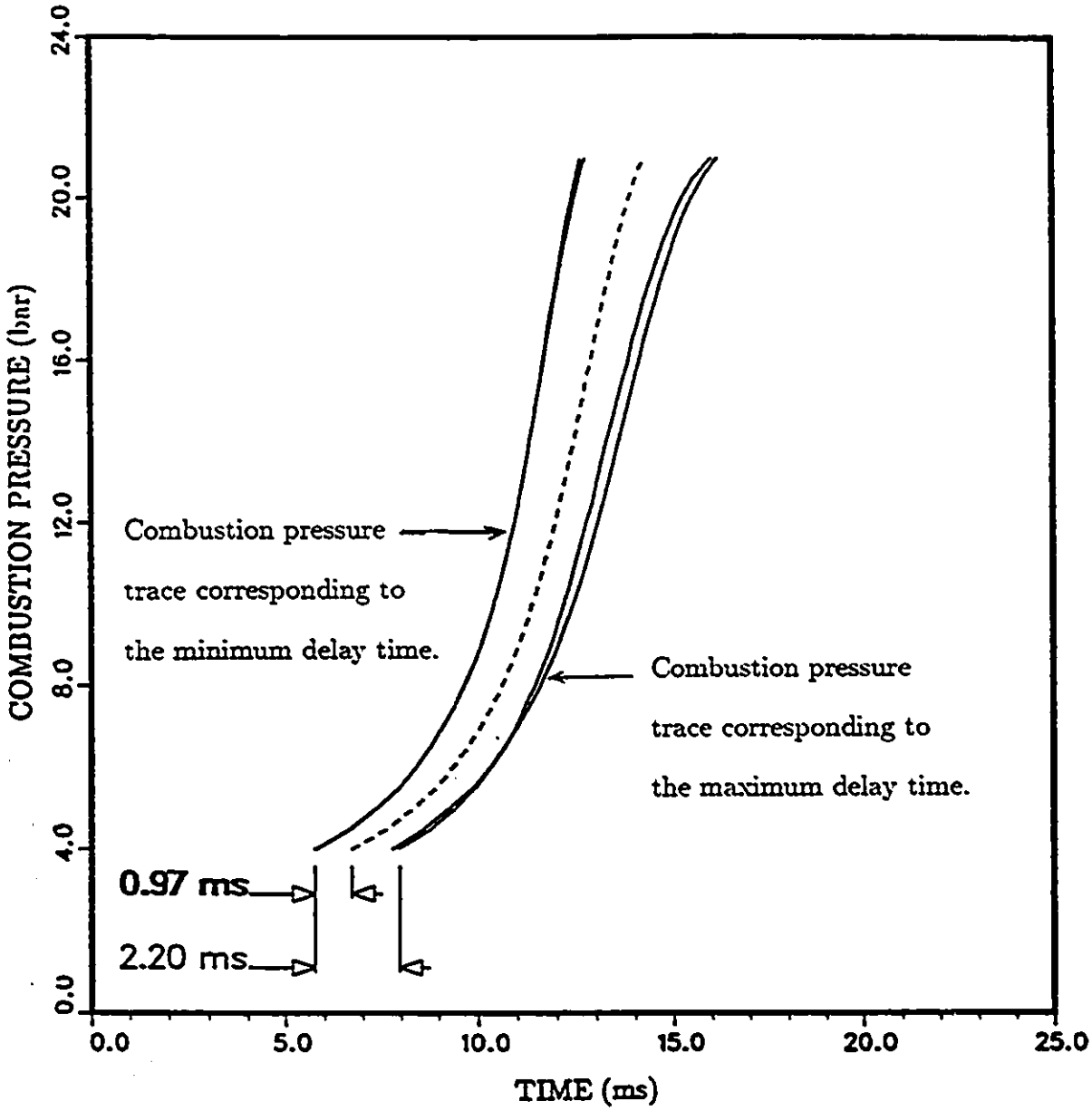

Figure 5.39: Determination of the minimum mean and maximum time delay (valve lift=7mm and ignition time=28 ms after closing valve)

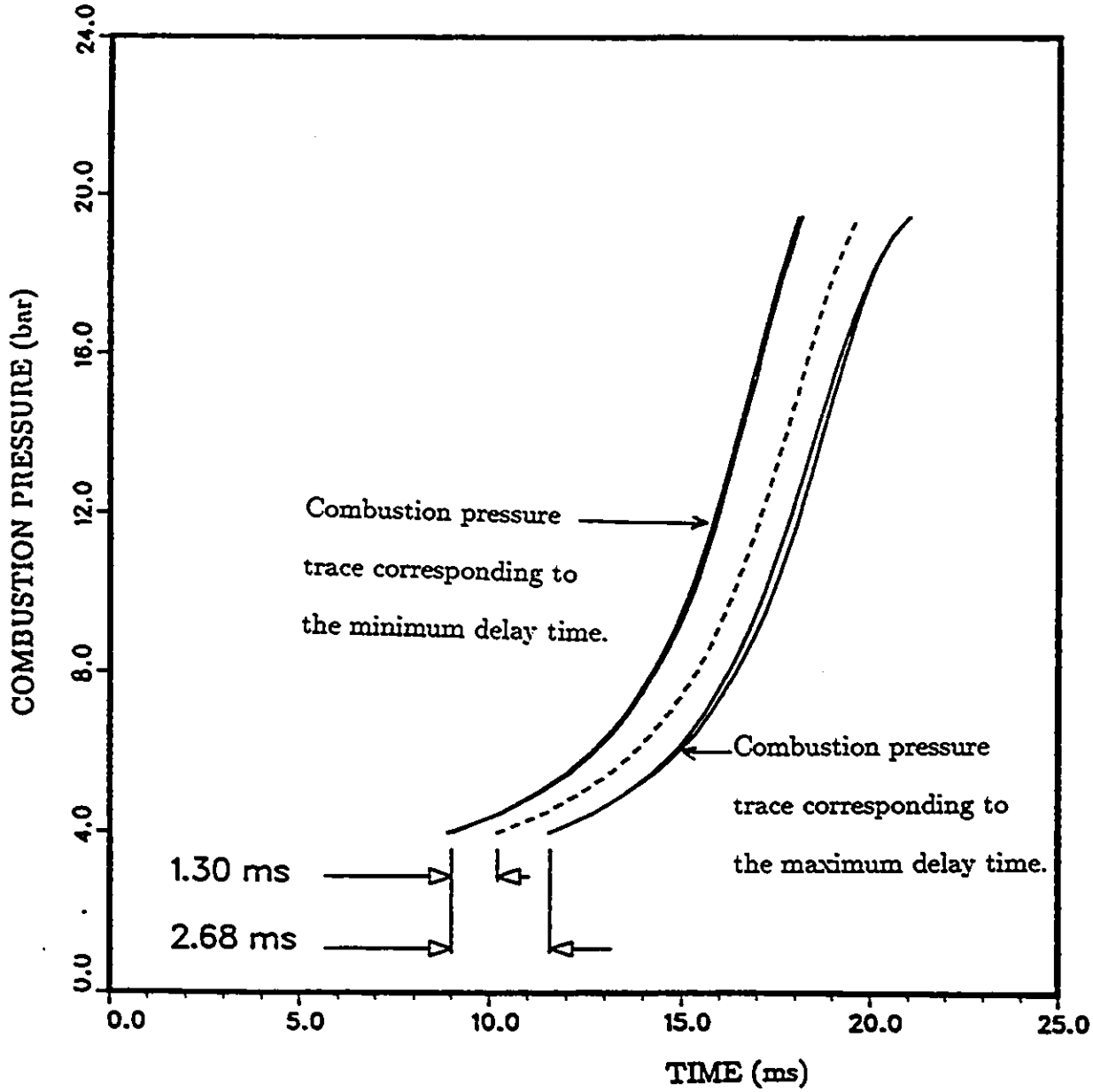

Figure 5.40: Determination of the minimum mean and maximum time delay (valve lift=12mm and ignition time=74 ms after closing valve)

Chapter 6

CONCLUSIONS AND RECOMMENDATIONS

6.1 General Conclusions

Based on the first phase of study, namely the investigation of turbulence structure, the following are the principal conclusions:

1. For the purpose of this study, a single hot wire anemometer was found to be a convenient and reliable technique for investigating the turbulence characteristics of a swirling flow.

2. The flow is fully tangential and the turbulence intensity is independent of hot wire orientation, implying an isotropic turbulence within the vessel.

3. The valve lift affects the spatial variation of turbulence at mid-radius. At quarter radius from center and to wall, the turbulence intensity and the Taylor microscale are independent of valve lift.

The following conclusions refer to the second phase of this study, namely combustion.

1. The initial cyclic variations in combustion contribute the most to cycle to cycle variations.

2. The standard deviation in delay time increases as the flame propagates.

3. The initial standard deviation in delay time is insensitive to variations in the mean flow and turbulence intensity.

4. The standard deviation is a strong function of Taylor microscale and laminar flame speed as implied by the Tennekes model.

5. The Taylor microscale deduced from the combustion traces and using the Tennekes model, are 20 % less than the value measured using the hot wire.

The above general conclusions are evidence that the Tennekes model explains the behavior of turbulent flame propagations in spark ignition engines for small scale structure.

6.2 Recommendations for Further Research

An obvious extension to this work would be the following:

- Turbulence s\ ıcture may change when the hot wire probe is replaced by the electrodes. Therefore, a simultaneous measurement of velocity and combustion pressure is necessary.
- The effect of laminar flame speed and Taylor microscale on initial cyclic variations in combustion should be investigated.
- The effect of the compression of unburnt gas on time delay in ignition should be studied.
- A large number of cycles should be taken in order to identify the occurrence of the ignition distribution function.

Chapter 7

REFERENCES

- Anderson, R. W. (1987), "The Effect of Ignition System Power in Fast Burn Engine Combustion." SAE Paper 870549.

- Arrigoni, V., Calvi, F., Cornett, G. M. and Pozzi, U. (1973), "Turbulent Flame Structure as Determined by Pressure Development and Ionization Intensity." SAE Paper No. 730088.

- Beshai, S. W., Deniz, O., Chomiack, J. and Gupta, A. K. (1988), "Cycle-by-Cycle Variation of Maximum Energy Release Rates in Spark Ignition Engine." ASME, Vol. 70, pp. 5-8.

- Boresi, A. P., Sidebottom, O. M., Seely, F. B. and Smith, J. O. (1978), "Advanced Mechanics of Materials, Third Edition." John Wiley and

Sons, New York.

- Broeze, J. J. (1950), "Combustion in Internal Combustion Engine." Engineering, Vol. 169, No. 4395.

- Chomiack, J. (1972), "Application of Chemiluminescence Measurement to the Study of Turbulent Flame Structure." *Combustion and Flame*, Vol. 18, pp. 429-433.

- Daneshyar, H. and Fuller, D. E. (1986), "Definition and Measurement of Turbulence Parameters in Reciprocating I.C. Engines." *Society of Automotive Engineers, Inc.*, Paper No. 861529.

- Gatowski, J. A., Heywood, J. B. and Deleplace, C. (1984), "Flame Photographs in a Spark Ignition Engine." *Combustion Science and Technology*, Vol. 56, pp. 71-81.

- Harrow, G. A. (1965), "A Study of Flame Propagation and Cyclic Dispersion in a Spark Ignition Engine." Advanced School of Automotive Engineering (Part IV), Combustion Process in the Spark Ignition Engine, Pergamon Press, July.

- Hill, P. G. (1988), "Cyclic Variations and Turbulence Structure in Spark Ignition Engine." *Combustion and Flame*, Vol. 72, pp. 73-89.

- Hill, P. G. and Kapil, A. (1989), "The Relationship between Cyclic Variations in Spark Ignition Engines and the Small Structure of Turbulence." *Combustion and Flame*, Vol. 78, pp. 237-247.

- Hires, S. D., Tabacyznski, R. J. and Novak, J. M. (1978), "The Prediction of Ignition Delay and Combustion Intervals for Homogeneous Charge, Spark Ignition Engine." *Society of Automotive Engineers, Inc.*, Vol. 87, Paper No. 780232.

- Kalghatgi, G. T. (1987), "Spark Ignition, Early Flame Development and Cyclic Variation in I.C. Engines." SAE Paper 870163.

- Karim, G. A. (1967), "An Examination of the Nature of Random Cyclic Variations in Spark Ignition Engine." *Journal of the Institute of Petroleum*, Vol. 53, No. 519, pp. 112-120.

- Keck, J. C. and Heywood, J. B. (1987), "Early Flame Developement and Burning Rates in Spark Ignition Engines and their Cyclic Variability." SAE Paper No. 870164.

- Lei, M. (1986), "Design of a Constant Combustion Vessel." 4^th year thesis, Ottawa University, Department of Mechanical Engineering.

- Liou, T. M. and Santavicca, D. A. (1985), "Cycle Resolved LDV Measurements in a Motored I.C. Engine." *Transaction of the ASME*, Vol. 107, pp. 232-240.

- Metghalchi, M., and Keck, J. C. (1982), "Burning Velocities of Mixtures of Air with Methanol, Isoctone, and Indolene at High Pressure and Temperatures." *Combustion and Flame*, Vol. 48, pp. 191-210.

- Milane, R. E., Tabaczynski, R. J. and Arpaci, V. S. (1983), "A Stochastic Model of Turbulent Mixing for the Prediction of Burn Rate in a Spark Ignition Engine." *Combustion Science and Technology*, Vol. 32, pp. 211-235.

- Milane, R. E., Evans, R. L. and Hill, P. G. (1986), "Combustion and Turbulent Structure in a Closed Chamber with Swirl." *Combustion Science and Technology*, Vol. 51, pp. 1-20.

- Milane, R. E. and Hill, P. G. (1988), "Turbulent Characteristics of Flame Propagation in a Swirling Flow of Premixed Fuel and Air". *Combustion Science and Technology*, Vol. 59, 4-6, pp. 275-295.

- Milane, R. E. (1990), "Cyclic Analysis of Turbulence and the Isotropic Relation for Length Scales in a Decaying Swirling Flow." International

Journal of Engineering Fluid Mechanics, Vol. 3, No. 3, pp. 207-223.

- Patterson, D. J. (1966), "Cylinder Pressure Variations, A Fundamental Combustion Problem." *Society of Automotive Engineers, Inc.*, Paper No. 66129.

- Pishinger, S. and Heywood, J. B. (1990), "How Heat Losses to the Spark Plug Electrodes Affect Flame Kernel Development in an SI-Engine." SAE Paper No. 900021.

- Soltau, J. P. (1961), "Cylinder Pressure Variations in Petrol Engines." *Proceedings of the Institution of Mechanical Engineers.* No. 2.

- Sreenivassen, K. R., Prabhu, A. and Narasimha R. (1983), "Zero Crossings in Turbulent Signals". *J. Fluid Mech.*, Vol. 137, pp. 251-272.

- Starkman, E. S., Strange, F. M. and Dahm, T. J. (1959), "Flame Speeds and Pressure Rise Rates in Spark Ignition Engines." *Society of Automotive Engineers, Inc.*, Paper No. 83.

- Swokowski, E. W. (1979), "Calculus with Analytic Geometry, Second Edition." Prinde, Weber and Schmidt, Boston.

- Tennekes, H. (1968), "Simple Model for the Small-Scale Structure of Turbulence." *The Physics of Fluids*, Vol. 11, No. 3.

- Vichnievsky, R. and Sale, B. (1958), "Etude de la Combustion sur le Monocylindre I.F.P. Renault C.N.R.S." J. Soc. Ing. Auto., Vol. 31.

- Wakisaka, T., Hamamoto, Y., Ohigashi, S. and Hashimoto, M. (1979), "Measurments of Air Swirl and Its Turbulence Characteristics in the Cylinder of an Internal Combustion Engine." Paper No. C91/79.

- Warren, J. A. and Hinkamp, J. B. (1956), "New Instrumentation for Engine Combustion Studies." *SAE Transactions*, Vol. 64, pp. 665-677.

- Witze, P. O. and Vilchis F. R. (1981), "Stroboscopic Laser Shadowgraph Study Effect of Swirl on Homogeneous Combustion in a Spark Ignition Engine." SAE Paper 810226.

- Witze, P. O., Hall, M. J. and Bennett, M. J. (1990), "Cycle-Resolved Measurements of Flame Kernel Growth and Motion Correlated with Combustion Duration." The Engineering Society for Advancing Mobility Land Sea and Space, Paper No. 900023.

- Young, M. B. (1981), "Cyclic Dispersion in the Homogeneous Charge Spark Ignition Engine - A Literature Survey." *Society of Automotive Engineers, Inc.*, Paper No. 810020.

Appendix A

DRAWINGS

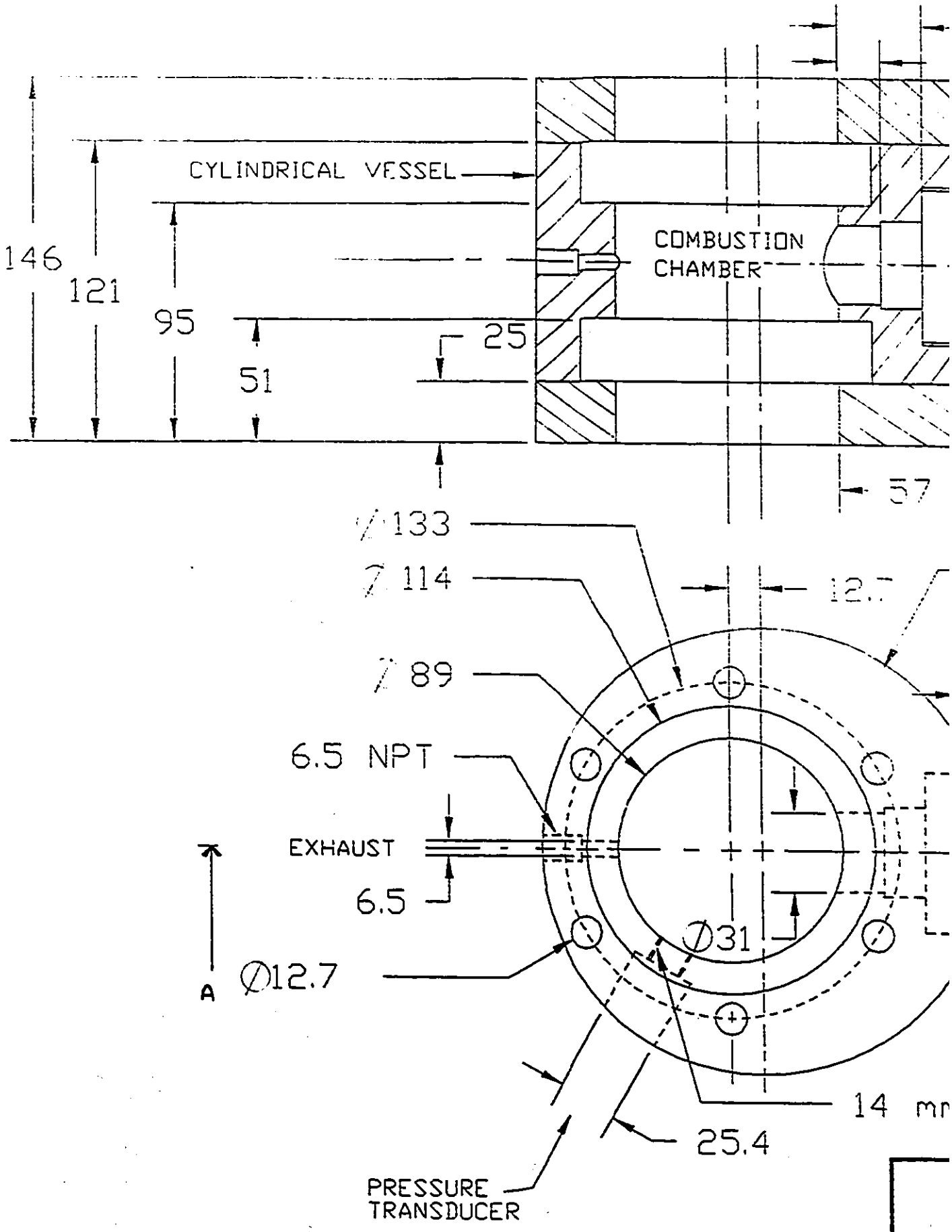
CYLINDRICAL VESSEL
COMBUSTION CHAMBER
146
121
95
51
25
57
∅133
∅114
∅89
12.7
6.5 NPT
EXHAUST
6.5
∅31
∅12.7
A
14 mm
25.4
PRESSURE TRANSDUCER

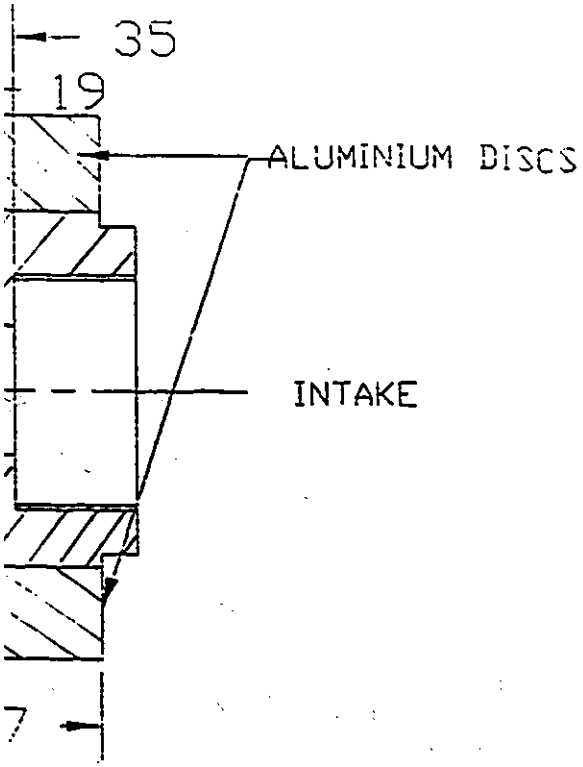

TOP VIEW

SECTION A-A

Ø178

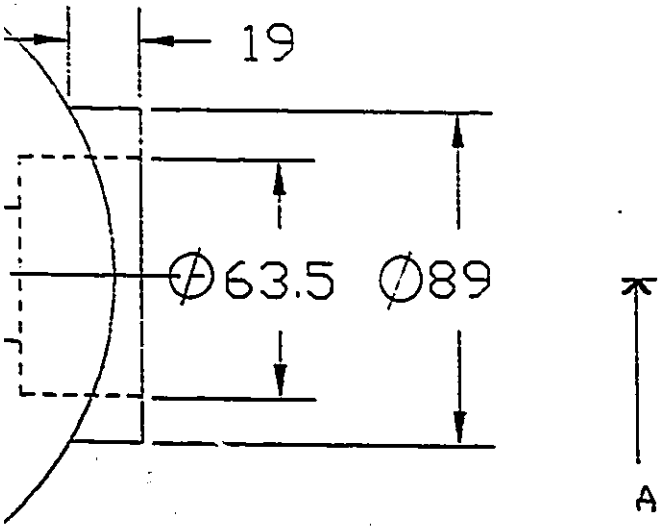

FRONT VIEW

mm x 1.25 mm THD (0.42 DEPTH)

UNIVERSITY OF OTTAWA DEPARTMENT OF MECHANICAL ENGINEERING	TITLE: COMBUSTION CHAMBER	DRAWING NO: 1 SCALE 1:2 (mm) DATE: JUNE 1992

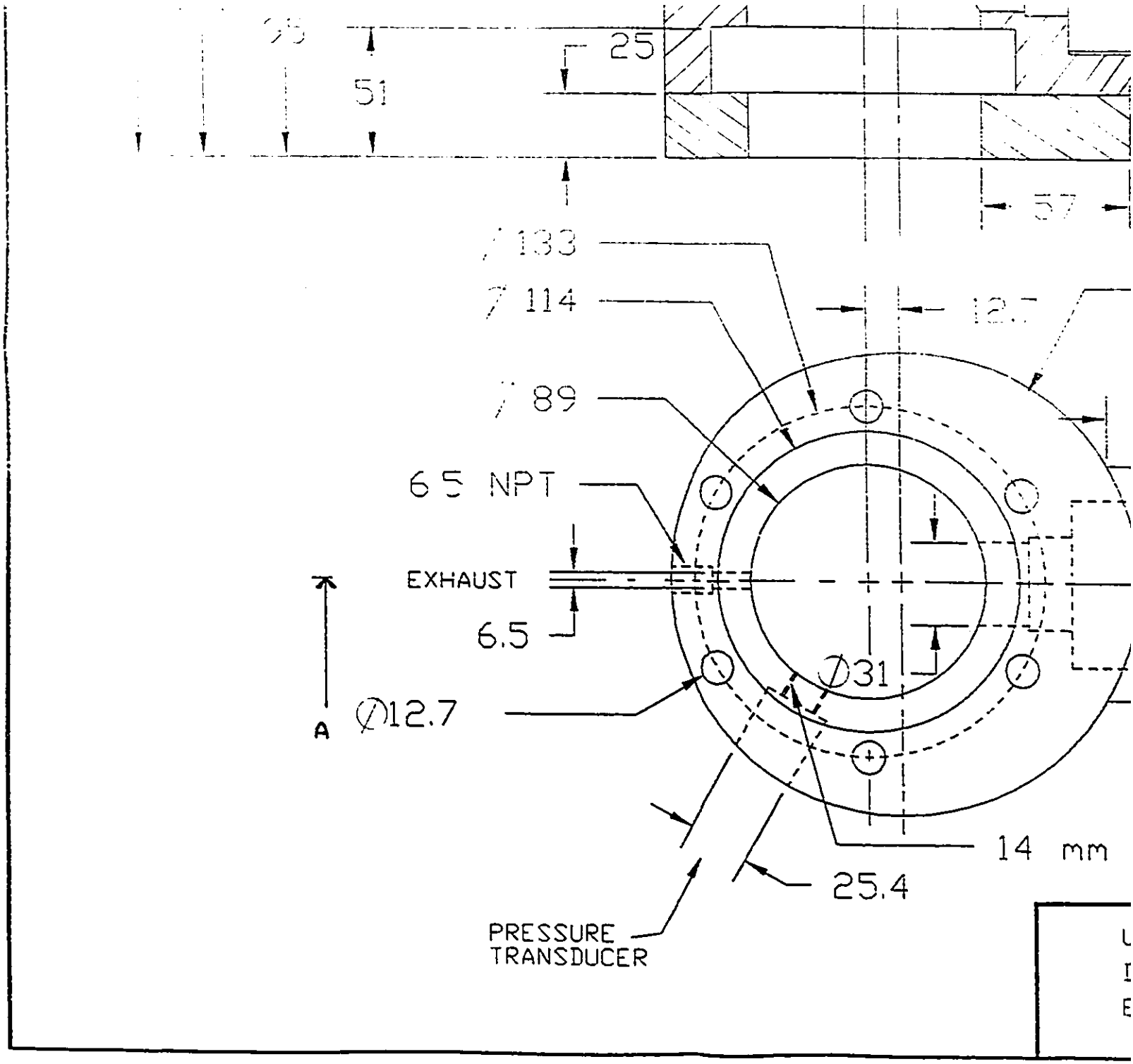

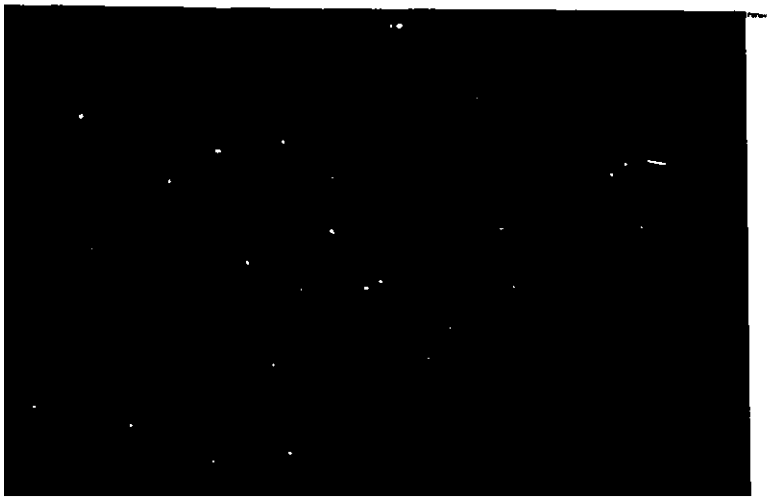

Drawing 1: Top and front view of the ves

SECTION A-A

Ø178

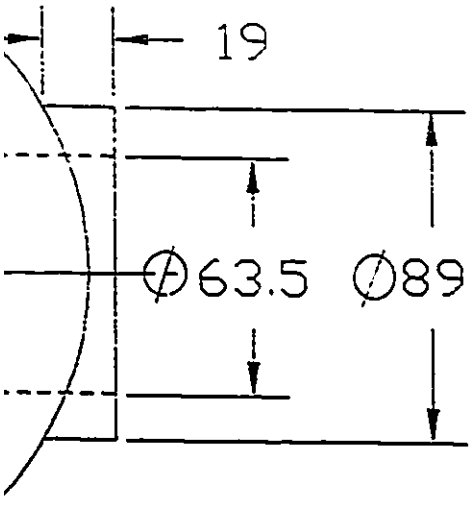

FRONT VIEW

ım x 1.25 mm THD (0.42 DEPTH)

UNIVERSITY OF OTTAWA DEPARTMENT OF MECHANICAL ENGINEERING	TITLE: COMBUSTION CHAMBER	DRAWING NO: 1 SCALE 1:2 (mm) DATE: JUNE 1992

ıe vessel.

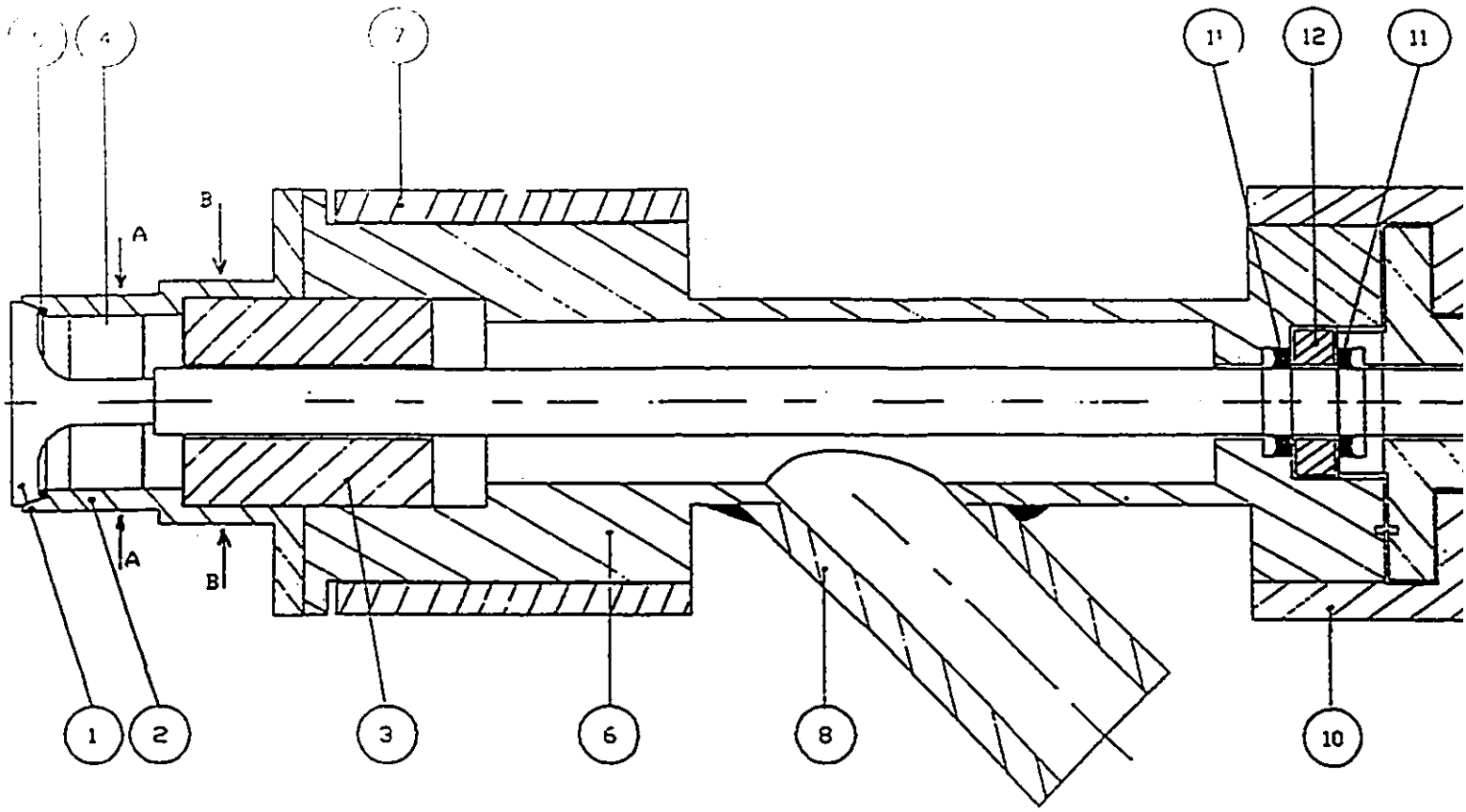

NO.	NAME OF PART	QTY. REQ.
1	VALVE	1
2	INTAKE PORT	1
3	VALVE GUIDE	1
4	SHROUD VALVE	1
5	O-RING	1
6	UPPER PORT	1
7	TREADED RING	1
8	INLET TUBE	1
9	VALVE ANGLE SELECTOR	1
10	SELECTOR CUP	1
11	U-CUP	2
12	PLACEMENT DISK	1
13	FLANGE LOCK NUT	1
14	FLANGE	1
15	LOCK NUT	1
16	AIR CYLINDER SHAFT	1
17	AIR CYLINDER	1

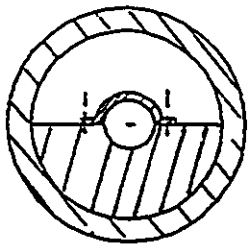

SECTION A-A

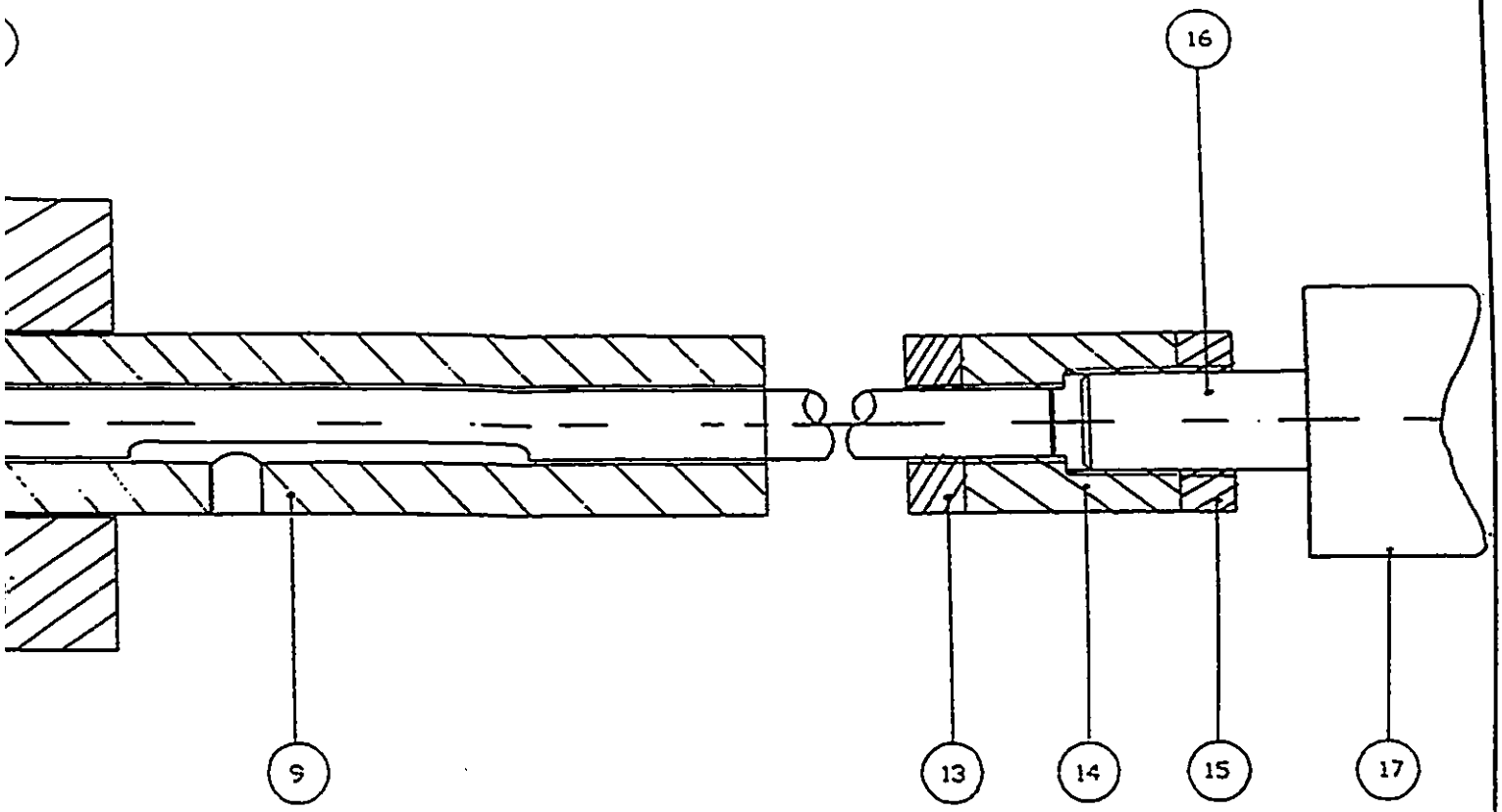

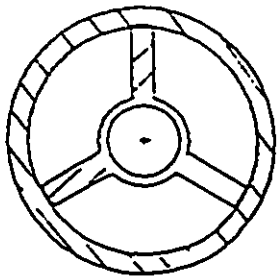

SECTION B-B

UNIVERSITY OF OTTAWA DEPARTMENT OF MECHANICAL ENGINEERING	TITLE: INTAKE SYSTEM	DRAWING NO: 2 SCALE 1: 1 DATE: JUNE 1992

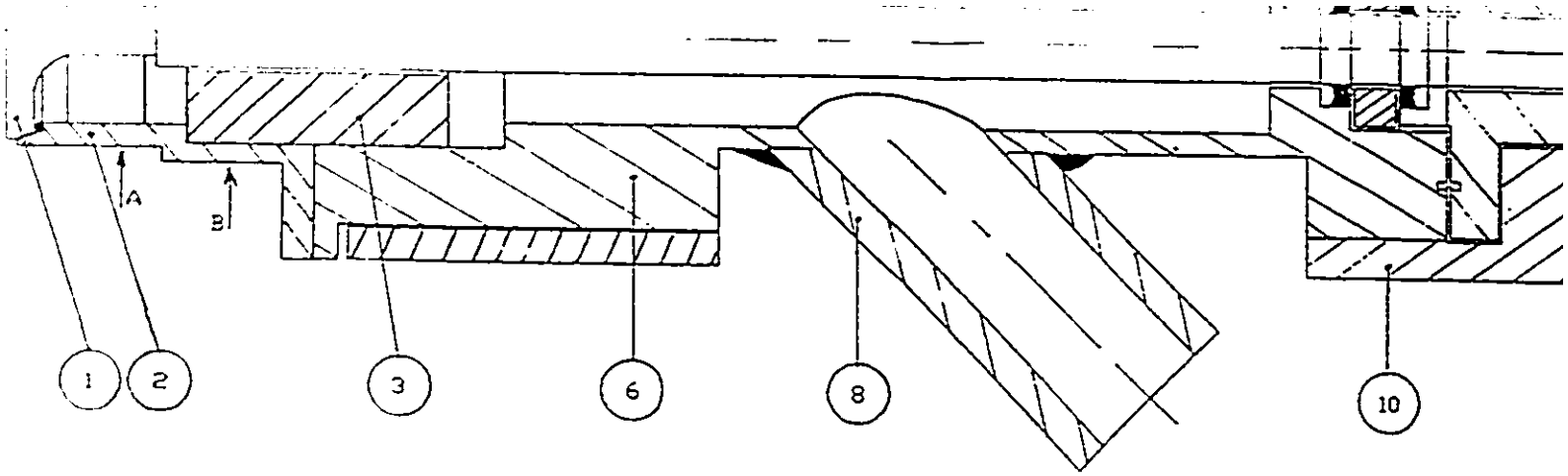

NO.	NAME OF PART	QTY. REQ.
1	VALVE	1
2	INTAKE PORT	1
3	VALVE GUIDE	1
4	SHROUD VALVE	1
5	O-RING	1
6	UPPER PORT	1
7	TREADED RING	1
8	INLET TUBE	1
9	VALVE ANGLE SELECTOR	1
10	SELECTOR CUP	1
11	U-CUP	2
12	PLACEMENT DISK	1
13	FLANGE LOCK NUT	1
14	FLANGE	1
15	LOCK NUT	1
16	AIR CYLINDER SHAFT	1
17	AIR CYLINDER	1

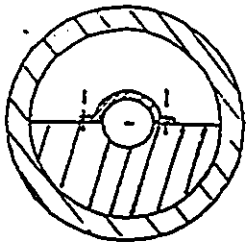

SECTION A-A

UNI
DEF
ENG

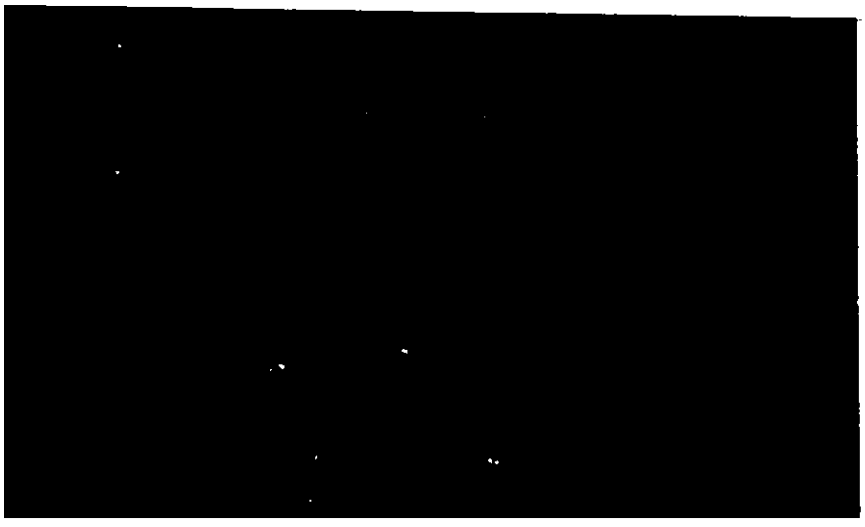

Drawing 2: Assembly drawin

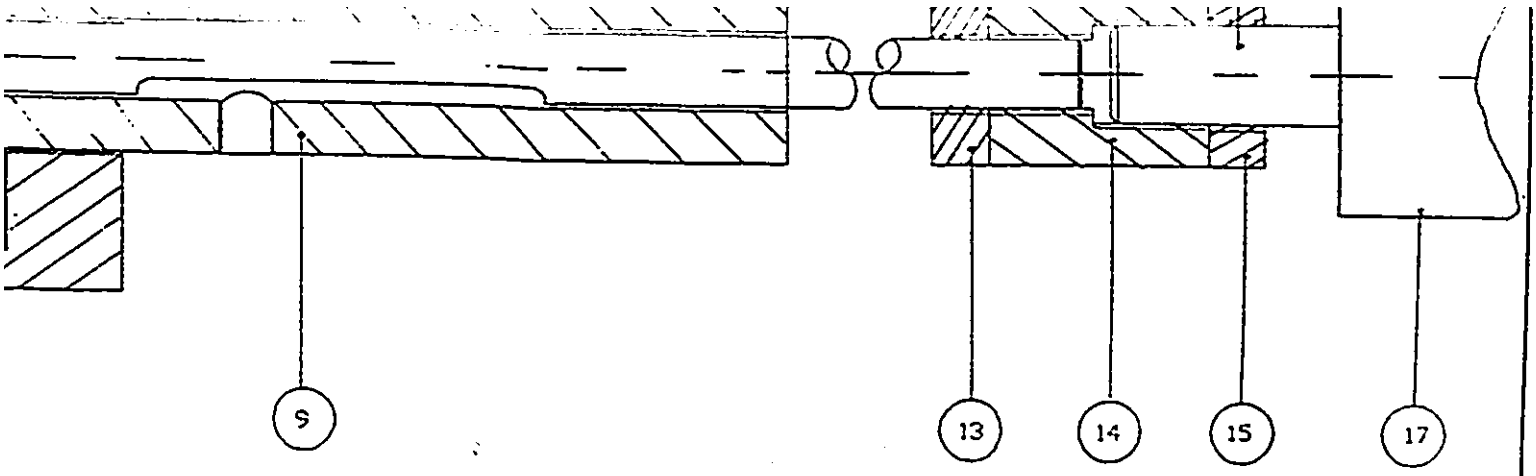

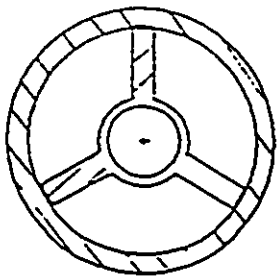

SECTION B-B

UNIVERSITY OF OTTAWA DEPARTMENT OF MECHANICAL ENGINEERING	TITLE: INTAKE SYSTEM	DRAWING NO: 2 SCALE 1: 1 DATE: JUNE 1992

awing of the intake system.

Appendix B

DESIGN OF THE INTAKE SYSTEM

The desired short injection time requires high acceleration of the intake valve which results in high impact load occurring at the valve-valve seat surface at valve closing time. A structural analysis of the situation was performed as follows:

On the return stroke, the air cylinder supplies a pulling force to close the valve.

Using an energy method, and assuming that all the kinetic energy of the valve is converted into elastic strain energy, since the intake part is much thicker compared to the valve rod diameter, the valve is expected to fail due to impact

loading before the intake port. It is assumed that the valve alone absorbs all the kinetic energy (in reality, this kinetic energy would be absorbed by the intake part, The "O" ring between the intake part and the valve depending on the elasticity of the "O" ring and the mass ratio of the valve and the intake part).

Using the conservation of energy one can write:

$$\frac{1}{2}mV_f^2 = \int_0^{x_f} f_x dx \qquad (B.1)$$

where m is the mass of the valve, V_f is the valve velocity at impact, f_x is a tensile force pulling the valve, dx is the differential change in extension of the valve and x_f is the total change in the valve length.

The normal strain in the x direction is defined by $\epsilon_x = \frac{x}{l}$ where l is the valve length and x is the change in length of the valve.

Since $\epsilon_x = \frac{x}{l}$, $d\epsilon_x = \frac{dx}{l}$. This implies that $dx = ld\epsilon_x$

Also, $f_x = A.\sigma_x$ where A is the cross-sectional area of the valve rod and σ_x is the normal stress in x direction. When $x = 0$ $\epsilon = 0$ and $\epsilon = \epsilon_f$ at $x = x_f$, where ϵ_f is the final normal strain.

Therefore

$$\frac{1}{2}mV_f^2 = Al\int_0^{\epsilon} \sigma_x d\sigma_x \qquad (B.2)$$

Assuming that the load does not exceed the proportional limit the tensile stress can be written as $\sigma_x = E\epsilon_x$, where E = Young's modulus. Substituting this relationship, known as Hooke's law, into equation (B.2) and rearranging yields:

$$\frac{1}{2}mV_f^2 = \frac{Al\sigma_x^2}{2E} \tag{B.3}$$

= On the other hand, based on conservation of energy one can write:

$$\frac{1}{2}mV_f^2 = P_c A_c h \tag{B.4}$$

= where P_c = pressure in the air cylinder, A_c = air cylinder cross-sectional area, and h = valve lift. Combining equations (B.3) and (B.4) results in:

$$\sigma_x = \sqrt{\frac{2P_c * A_c * h * E}{A * l}} \tag{B.5}$$

This relationship shows that the tensile stress is inversely proportional to the square root of the rod length. Therefore, a very long rod was used to minimize the normal tensile stress.